A modeling study to investigate performance of SOFC-ICE hybrid systems for marine applications

J.W. Reurings

Technische Universiteit Delft

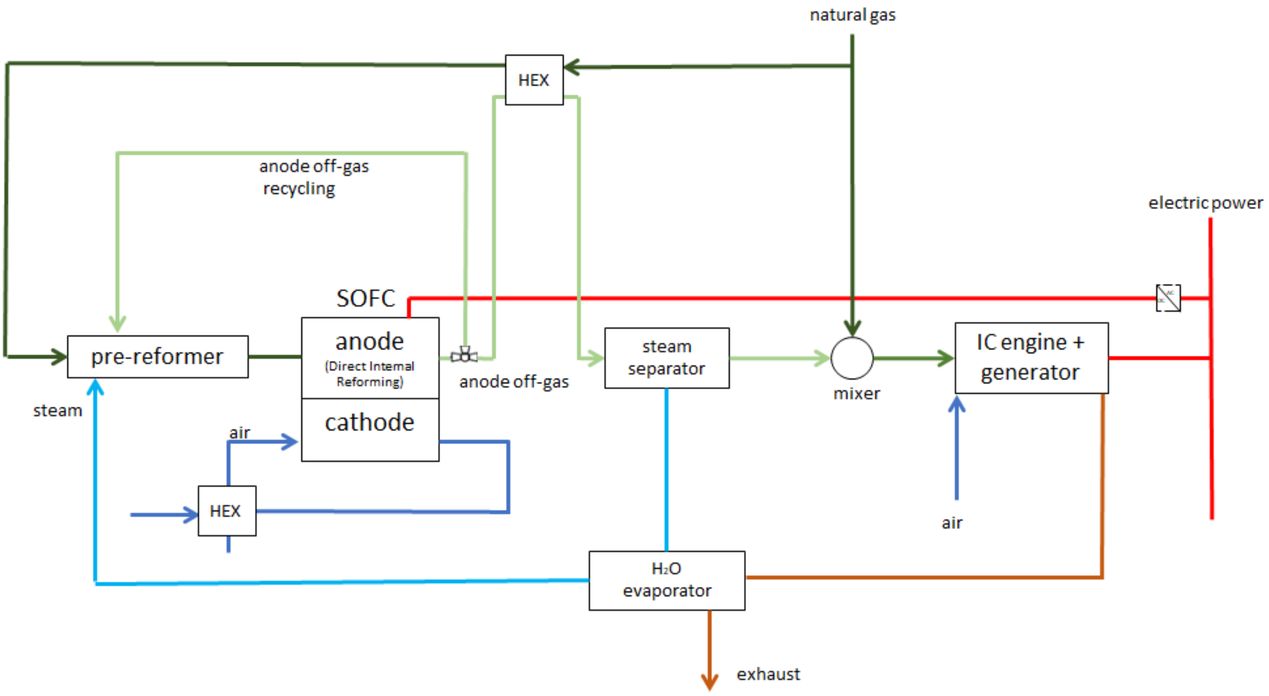

TU Delft

A modeling study to investigate performance of SOFC-ICE hybrid systems for marine applications

by

J.W. Reurings

to obtain the degree of Master of Science in Mechanical Engineering
at the Delft University of Technology,

Student number:	1323385	
Project duration:	November 2018 – July 2019	
Thesis committee:	dr. P.V. Aravind,	TU Delft, supervisor
	Ir. J.N. Stam,	TU Delft, mentor
	Ir. T. Woudstra,	TU Delft
	Ir. K. Visser,	TU Delft
	Ir. H.D. Sapra,	TU Delft

Abstract

Emissions restrictions imposed by the International Maritime Organization (IMO) is forcing ship owners and builders to look into alternative fuels and prime movers. The high efficiency of fuel cells could help to decrease emissions in marine power generation. Solid oxide fuel cells (SOFCs) are the most fuel flexible among fuel cells, the high operating temperature and the possibilities for direct internal reforming (DIR) makes this technology of great interest for natural gas fueled systems. SOFCs operating in hybrid system configuration could even achieve higher efficiencies, due to effective utilization of left-over fuel in anode off-gas and adequate system heat integration.

In literature extensive research is found about hybridization of SOFCs and gas turbines. For such hybrid configurations high efficiencies are projected, however poor part load performance and high system complexity are tempering the interest for marine applications. SOFC integration with an internal combustion engine (ICE) also has high projected efficiencies and is expected to enable system integration in marine applications with limited complexity, higher robustness, and lower costs compared to SOFC-gas turbine integration. However, due to the novelty of SOFC-ICE hybrid systems, not much research has been published as of yet and the research that is found shows a variety in system configurations and performance results. This observation justifies additional SOFC-ICE hybrid system research, particularly if the system has to operate on marine applications.

In this work an integration of an SOFC and ICE is proposed. Both SOFC and ICE share the load on the system: the SOFC can operate on a base load, while the ICE can handle majority of the transient load. A pre-reformer is proposed, which supplies partially reformed methane to the SOFC. The ICE is supplied with natural gas mixed with excess fuel from the SOFC-anode. This additional natural gas supply to the engine makes it a combined cycle, instead of a bottoming cycle, and allows better dynamic load control and increases reliability. Also system heat integration is an essential requirement, as the steam required for methane pre-reforming is produced with heat from engine exhaust system.

System component models are developed and individually analysed. Thereafter both component models are combined to an SOFC-ICE hybrid system model and a study is conducted to investigate the sensitivity of the following operating parameters and system configurations on system performance and efficiency: SOFC current density, SOFC fuel utilization, anode off-gas recycling, methane pre-reforming ratio, pre-reformer integration, and power split ratio.

The SOFC component model provides insights of performance behaviour when varying operating parameters. The ICE model clearly indicates the advantages when hydrogen is added to natural gas, both improved engine efficiency and improved combustion stability are demonstrated. Finally, it is found that operating the hybrid system model consisting of a 375 kWe (AC) SOFC and a 375 kWe ICE leads to an electric efficiency of 45.7 % (LHV). This is a 5 to 10 percent point improvement compared to conventional diesel engines operating in this power range [1]. In this hybrid system the SOFC current density is set to 5000 $\mathrm{A\,m^{-2}}$, anode off-gas recycling is not applied, and 30 % of the SOFC fuel is pre-reformed. The SOFC fuel utilization is set to 86 % in order to avoid too large hydrogen-natural gas blending ratios at the ICE intake, which are currently not substantiated with engine experiments. Future modeling of the ICE should make it possible to extend the hydrogen-natural gas blending ratio, such that even higher hybrid system efficiencies can be demonstrated.

This work demonstrates that the SOFC-ICE hybrid system operating at a 50 % SOFC and 50 % ICE power split provides a firm efficiency improvement compared to conventional diesel driven power plants in the range upto 1 MW. An higher efficiency means a lower fuel consumption and thus a CO_2-emissions reduction. Also NO_x-formation is reduced, due to the absence of expansive high temperature combustion in the fuel cell part of the system. Considering volumetric power density, the SOFC-ICE hybrid system installation volume is more than twice as large as conventional marine power plants. Taking the energy conversion efficiency into account, the LNG storage space for proposed hybrid system is two times larger than that of a diesel fueled generator set. A 50 % SOFC and 50 % ICE power split leads to these numbers, depending on the operating profile a different power split can lead to other efficiencies and volume and weight constraints. The impact of power density and energy density depend on the practical application (e.g. ship design, required power, endurance, operating profile, and costs) and must be considered case-by-case.

Preface

After 10 years of working as a marine engineering officer in the Netherlands Navy, I was offered the opportunity to pursue a two years master degree in mechanical engineering. An offer I couldn't refuse and I accepted it with pleasure. These were two challenging years of hard work, but it was well worth it. The practical experience obtained with sailing on hi-tech frigates motivated me in understanding the underlying physics taught in academic courses. With both under my belt, I'm looking forward to going back to work and contribute to the development of innovative and future-proof navy ships.

This thesis was written to fulfil the gradation requirements of the *Energy, Flow and Processes* track in the Mechanical Engineering MSc programme at the Delft University of Technology. The study was carried out in the period from November 2018 to July 2019. During the entire period I have had great support from numerous people around me. Furthermore, I would like to give special word of thanks to the following people: First of all I would like to thank associate Professor dr. P.V. Aravind for giving me the opportunity to work on this topic and for supervising this project. I would like to acknowledge my daily supervisor Jelle Stam MSc for sharing his fuel cell knowledge and teaching me the details of electrochemistry. Also, at least as important, was his support and guidance in doing academic research. Jelle was always ready to answer my questions or to have a valuable discussion. The weekly meetings we had gave me the perfect guidance throughout the project and helped me keep a steady pace. For the engine part of this research, I would like to thank Harsh Sapra MSc. Harsh's enthusiasm and knowledge of marine internal combustion engines renewed my interest and inspired me to do something with combustion engines in a thesis project. The guidance he gave me in engine modeling and the discussions we had were of great value to this project. Theo Woudstra MSc for the discussion we had about system integration, and Jeroen Hiemstra for his readiness in reading the report. Finally, I would like to thank my girlfriend Lia for her steadfast support during this study and for continually helping me focus on my end goal.

J.W. Reurings
Leiden, July 2019

Contents

Nomenclature

Acronyms

$AOGRR$	Anode off-gas recycling ratio
REF	Methane pre-reformer ratio
3ME	Mechanical, maritime and materials engineering
AC	Alternating current
AOG	Anode off-gas
BDC	Bottom dead centre
BMEP	Brake mean effective pressure
BoP	Balance of plant
CFD	Computational fluid dynamics
CI	Compression ignition
DC	Direct current
DIR	Direct internal reforming
EC	Exhaust valve closed
EGR	Exhaust gas recirculation
EO	Exhaust valve open
GT	Gas turbine
HC	Homogeneous charge
HCCI	Homogeneous charge compression ignition
HEX	Heat exchanger
HOR	Hydrogen oxidation reaction
IC	Inlet valve close
ICE	Internal combustion engine
IMO	International Maritime Organization
IO	Inlet valve open
LCSF	Lanthanum strontium ferite
LHV	Lower heating value (mass, molar, or volumetric)
LSM	Lanthanum strontium manganite
MEA	Membrane electrode assembly
MSR	Methane steam reforming

MVFP	Mean value first principle
O/C	Oxygen to carbon ratio
OCV	Open circuit voltage
PEMFC	Proton exchange membrane fuel cell
PEN	Positive electrode, Electrolyte, Negative electrode
RCCI	Reactivity controlled compression ignition
RPM	Revolutions per minute
S/C	Steam to carbon ratio
SI	Spark ignition
SOFC	Solid oxide fuel cell
TDC	Top dead centre
TPB	Thriple phase boundary
UHC	Unburned hydrocarbons
VOCs	Volatile organic compounds
WGS	Water-gas shift
YSZ	Yittrium-stabilized zirconia

Greek Symbols

α	Aspect ratio (length/width)	–
α	Convective heat transfer coefficient	$\mathrm{W\,m^{-2}\,K^{-1}}$
β	Charge transfer coefficient	–
Δh	Enthalpy of reaction	$\mathrm{J\,mol^{-1}}$
$\dot{\phi}$	Volume flow rate	$\mathrm{m^3\,h^{-1}}$
ϵ	Surface emissivity	–
η	Efficiency	–
λ	Air-to-fuel ratio / Air excess ratio	–
μ	Dynamic viscosity	$\mathrm{kg\,m^{-1}\,s^{-1}}$
ϕ	Fuel-to-air ratio	–
π	Pressure ratio	–
ρ	Density	$\mathrm{kg\,m^{-3}}$
σ	Electronic (ionic) conductivity	$\mathrm{\Omega^{-1}\,m^{-1}}$
σ	Engine stoichiometric air to fuel ratio	-
σ	Stefan-Boltzmann constant	$\mathrm{W/(m^2 \cdot K^4)}$
τ	Thickness	m

Roman Symbols

$\dot{m}$	Mass flow rate	$\mathrm{kg\,s^{-1}}$
$\dot{N}$	Molar flow rate	$\mathrm{mol\,s^{-1}}$
$\dot{Q}$	Heat transfer	W
A	Area	$\mathrm{m^2}$
a	Activity	-
C	Concentration	$\mathrm{mol\,m^{-3}}$
c_p	Specific heat capacity at constant pressure	$\mathrm{J\,kg^{-1}\,K^{-1}}$
C_{inf}	Bulk concentration	$\mathrm{mol\,m^{-3}}$
D_h	Hydraulic diameter	m
E	Electric potential	V
E_0	Electric potential at standard temperature and pressure and with pure reactants	V
E_a	Activation energy	$\mathrm{J\,mol^{-1}}$
F	Faraday's constant	$\mathrm{C\,mol^{-1}}$
f	Power fraction in hybrid system	-
G	Gibbs free energy	$\mathrm{J\,mol^{-1}}$
H	Height	m
h	Molar specific enthalpy	$\mathrm{J\,mol^{-1}}$
I	Current	A
i	Current density	$\mathrm{A\,m^{-2}}$
i	Engine number of cylinders	-
i_0	Exchange current density	$\mathrm{A\,m^{-2}}$
i_{limit}	Limiting current density	$\mathrm{A\,m^{-2}}$
k	Engine cycles (=2 for 4 stroke)	-
k	Reaction constant	$\mathrm{mol\,s^{-1}\,m^{-2}\,bar^{-1}}$
k	Thermal conductivity	$\mathrm{J\,m^{-1}\,s^{-1}\,K^{-1}}$
$K_{eq,MSR}$	Equilibrium constant MSR	–
$K_{eq,WGS}$	Equilibrium constant WGS	–
L	Length	m
M	Molar mass	$\mathrm{g\,mol^{-1}}$
m	Mass	kg
N	Mole number	mol
n	Number of moles of electrons	–
n	Polytropic exponent	–

P	Perimeter	m
P	Power	W
p	Pressure	bar
Pd	Power density	$\mathrm{W\,m^{-2}}$
q	Specific heat	$\mathrm{kJ\,kg^{-1}}$
R	Universal gas constant	$\mathrm{J\,mol^{-1}\,K^{-1}}$
r	Reaction rate (area specific)	$\mathrm{mol\,m^{-2}\,s^{-1}}$
r_{ohm}	Area specific resistance	$\Omega\,\mathrm{m^{-2}}$
Re	Reynolds number	–
T	Temperature	K
t	Time	s
u	Specific internal energy	$\mathrm{J\,kg^{-1}}$
u	Velocity	$\mathrm{m\,s^{-1}}$
U_f	Fuel utilization	–
U_{ox}	Oxygen utilization	–
V	Electric potential	V
v	Volume	$\mathrm{m^3}$
W	Width	m
w	Specific work	$\mathrm{J\,kg^{-1}}$
x	ICE modeling: mass fraction	–
x	SOFC modeling: mole fraction	–

Superscripts

0	Standard condition
$conv$	Convective
in	SOFC ingoing
net	Net
out	SOFC outgoing
rad	Radiative

Subscripts

1 – 6	Seiliger stages
a	Anode
a, b, c	Seiliger parameter
$a - d$	Engine stage point

act	Active
ae	Anode electrode
af	Anode flow
AOG	Anode off-gas
BT	Before throttle
c	Cathode
c	Compression (engine)
ce	Cathode electrode
$cell$	Single cell
cf	Cathode flow
ch	Channel
com	Engine turbocharger compressor
cv	Control volume
e	Electrochemical reactions
e	Electronic
e	Expansion (engine)
f	Fuel
g	Gas (exhaust gas)
hl	Heat loss
HOR	Hydrogen oxidation reaction
HS	Hybrid system
i	Species 'i'
ic	Indicated
ic	Interconnect
ICa	Interconnect at anode side
ICc	Interconnect at cathode side
ID	Ideal situation
is	Isentropic
MSR	Methane steam reforming
NG	Natural gas
PEN	PEN structure
pre	Pre-reformer
se	Solid electrolyte
sg	Stoichiometric
TC	Turbocharger
tur	Engine turbocharger turbine
WGS	Water-gas shift

1

Introduction

1.1. Background

The importance of maritime transport for trade and development cannot be overemphasized. 80 % of global trade by volume and more than 70 % of its value is being carried on board ships and handled by seaports worldwide. The maritime transport industry's annual carbon emission accounts for 2.2 % of global CO_2 emission released by humans and could grow by between 50 % and 250 % by 2050 [2]. Moreover the maritime transport industry is responsible for 15 % of annual global NO_x emissions and 13 % of annual global SO_x emissions [3]. Given these trends, a drastic improvement of marine power plants is mandatory. Therefore emissions restrictions imposed by the International Maritime Organization (IMO) is forcing ship owners and builders to look into alternative fuels and prime movers. A trend in marine transport applications is the increased interest in all-electric ships [4]. In an all-electric ship electric power is used for auxiliaries and propulsion. Currently the vast majority of all-electric ships use diesel generators to produce the required electric power, but this all-electric configuration also creates alternative, more efficient, and cleaner techniques of power generation.

Fuel cell technology is such an advanced power generation technique which can particularly play an important role in reducing emissions and increasing efficiency. In fuel cell systems, chemical energy is directly converted into electrical energy. The absence of expansive high temperature combustion gives high efficiencies and reduces NO_x-formation.

A solid oxide fuel cell (SOFC) is the most fuel flexible technology among fuel cells. Efficiencies of SOFCs exceed those of conventional thermal cycles [5], and the SOFC is favourable because direct internal reforming (DIR) makes this technology of great interest for natural gas fueled systems. Natural gas fueled systems have fuel processing and logistic advantages compared to pure hydrogen-demanding fuel cells as proton exchange membrane fuel cells (PEMFC) [1].

Fuel cell systems, and particularly SOFCs, operating in hybrid system configurations are projected to achieve even higher efficiencies compared to standalone systems, due to effective utilization of left-over fuel in the anode off-gas and integration of residual heat from fuel cell stack and engine exhaust gas.

A variety of SOFC hybrid system configurations have been studied in the past, mostly with either gas turbines or Rankine cycles. SOFC integration with gas turbines (SOFC-GT) is advantageous compared to standalone SOFC systems, in addition to the utilization of left-over fuel in the gas turbine burner, it provides good integration with the SOFC cathode air flow. Various computational SOFC-GT hybrid system simulations and analyses have been carried out where maximum electric efficiencies up to 70 % are projected [6–10].

In addition to these computational simulations, physical demonstration studies are performed by Siemens Westinghouse and Mitsubishi Heavy Industry (MHI). Siemens Westinghouse developed the first prototype SOFC-GT hybrid system combining their pressurized SOFC stack with a micro gas turbine. An electrical efficiency of 55 % at 220 kW has been reported [11]. MHI has developed a same type of pressurized SOFC-GT hybrid system producing 200 kW and demonstrated 52 % electrical efficiency [12]. Although these SOFC-GT turbine cycle were demonstrated 20 years ago, the technology has not left the laboratory phase. Both studies indicate that SOFC-GT hybrid system operation requires a complex control of operating parameters when

---

[1] Although natural gas itself is not a green energy source, before an effective sustainable industry can be achieved, a transitional phase is needed to deal with the stricter emission regulations. This is why natural gas is preferred above diesel fuel as a intermediate solution.

there is a coupling between the fuel cell and the turbo-machinery, particularly when the SOFC is operated pressurized or at part-load.

A fairly novel hybrid design is an SOFC integration with a reciprocating internal combustion engine. A SOFC-ICE hybrid system can have a number of benefits over the previously discussed SOFC-GT systems. First: the use of remaining fuel in the anode off-gas in an internal combustion engine can lead to high total system electric efficiencies. SOFG-ICE hybrid system simulations conducted by Park et al. indicated a maximum electrical efficiency of 59.5 %. [7]. An SOFC combined cycle comparison study conducted by van Biert et al. indicated a maximum electric efficiency of 64 % for the SOFC-ICE system [13] and an SOFC-ICE hybrid system computational system optimization study conducted by Chuahy and Kokjohn achieved a maximum electrical efficiency of 70 % [14]. Second: internal combustion engines have relative higher efficiencies across the full load range than gas turbines, which makes them more efficient and effective in following dynamic load curves and at part-load operation [14, 15]. Third: previous engine studies indicate that mixing natural gas with fuels that posses faster burning speeds and smaller ignition energy, for example hydrogen in anode off-gas, is an effective way to increase combustion rate and enhance combustion stability in a gas engine. [16–20]. In other words, addition of hydrogen-rich anode off-gas to natural gas expands the operating window of a gas fueled internal combustion engine and thereby enhances the usability of gas engines in marine transport applications. Finally: system power and efficiency of internal combustion engines are less sensitive to ambient condition variations [15] and system complexity and maintenance costs are generally lower for reciprocating internal combustion engine compared to gas turbines. These factors make the internal combustion engine a suitable and economical choice for marine hybrid SOFC operation.

Summarizing: SOFC-ICE hybrid systems are expected to facilitate marine system integration with better overall efficiency performance, lower system complexity, higher robustness, and lower costs compared to SOFC-GT systems.

1.2. Problem statement and objective

The SOFC-ICE hybrid system advantages are promising, but these systems are in the early phase of development. Operating an SOFC combined with a reciprocating engine is relatively unexplored. The above mentioned SOFC-ICE hybrid studies are the only three studies found and are demonstrating significant difference in output results, system designs, type of ICE, and modeling approach. Also no models are validated on the system level, because of a lack of system level-data. The novelty of SOFC-ICE hybrid systems and the variety of previous research results form the foundation for the problem statement and the objective of this work.

The overall problem statement is:
How can alternative marine power plants contribute to high performance and reduced emissions in shipping?

The objective is:
Identify relevant operating parameters and system configurations of SOFC-ICE hybrid systems for marine applications and find their influence on system efficiency and performance, by developing component models and conducting a hybrid system parameter sensitivity analysis.

1.3. Thesis outline

In chapter 2, a literature study provides SOFC and ICE background information and reviews previous studies. A description of the applied research methodology is explained in chapter 3. A zero dimensional SOFC model with pre-reformer is developed in chapter 4. In chapter 4 it is demonstrated the SOFC model can operate as a standalone component model and can provide insights of both steady state and dynamic SOFC operation, including the influence of SOFC operating parameters on performance. These SOFC operating parameters are expected to have influence on hybrid system performance also. The engine model is developed in chapter 5, here it is demonstrated that operating an engine with hydrogen-enriched fuel improves engines performance, which occurs in case of hybrid system operation also. In chapter 6 the individual component models are integrated to a hybrid system model and with that model an operating parameter and system configuration sensitivity study is carried out. Chapter 7 concludes and provides recommendations for future work.

2

Literature study

Before starting the development of any component model, a literature study is conducted to the working principles of SOFCs, a study is conducted on internal combustion engines, and a literature review study is done to determine what already has been found in the past on SOFC hybrid systems. Also, a brief description is given of marine power plant requirements.

2.1. Solid oxide fuel cells

An solid oxide fuel cell (SOFC) is known to be an efficient energy conversion system that produces electrical power by continuously converting chemical energy into electrical energy through an electrochemical reaction. Electrical efficiencies up to 60 % can be achieved with natural gas-fuelled systems [21]. Fuel cells typically utilize hydrogen as fuel and oxygen as the oxidant in the electrochemical reaction. A schematic representation of this electrochemical process is depicted in figure 2.1. To illustrate the external lay-out of an SOFC, a picture of a 50 kW SOFC stack for operation on board an ocean-going vessel is shown in figure 2.2.

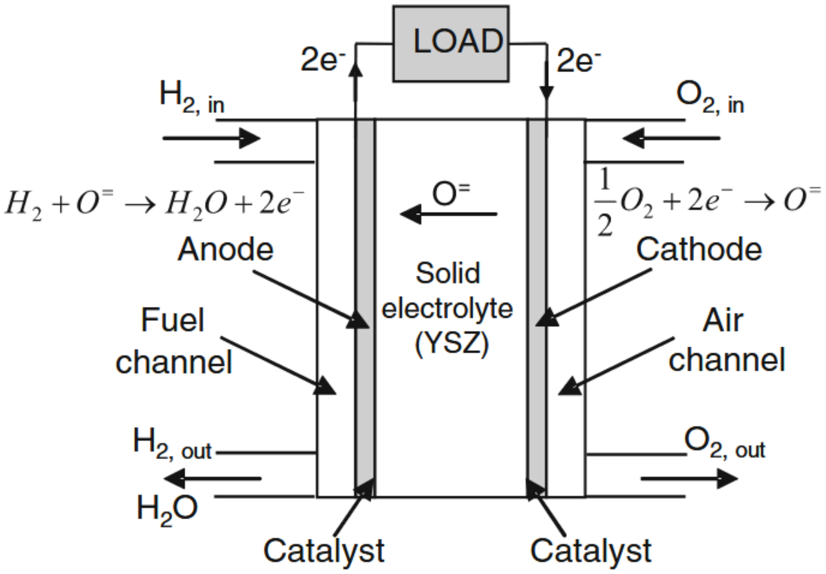

Figure 2.1: Anode and cathode reactions for the SOFC [22].

2.1.1. SOFC principles

A single SOFC-cell consists of five layers: anode, cathode, solid electrolyte, and two current collectors (or interconnecting plates). As illustrated in figure 2.1, hydrogen is supplied to the anode and oxygen is supplied

Figure 2.2: Sunfire - 50 kW SOFC for marine applications[23].

to the cathode. At the region of contact between cathode, electrolyte, and oxygen, also known as triple phase boundary (TPB), the oxygen reduction takes place (figure 2.3). In between, the solid electrolyte conducts the flux of oxygen ions to the anode. At the anode side TPB, the anode, electrolyte, and gaseous fuel are in contact. At this TPB the hydrogen oxidation reaction takes place. During this process electrons are released together with heat and water. In literature, the solid combination of positive electrode, electrolyte, and negative electrode is often called PEN structure or MEA (membrane electrode assembly). An example of a PEN structure composition is illustrated in figure 2.4. If natural gas is fueled to the system, also carbon monoxide can function as a fuel.

The SOFC is a complete solid-state device that uses an oxide ion-conducting ceramic material as electrolyte. In today's commercially available SOFCs the anode is a cermet made of metallic nickel and an yttrium-stabilized zirconia skeleton (NiO/8YSZ). The anode has a porous structure so that mass transport of reactant gas and product gas is not inhibited. Similar to the anode, the cathode has a porous structure that must allow rapid mass transport of reactant and product gasses. Commonly strontium-doped lanthanum manganite (LSM) or strontium-doped lanthanum ferite (LCSF) is used for the cathode material. The current collector materials can be conductive ceramic materials for high temperate operating fuel cells (900-1000 °C) or metallic alloys for intermediate temperature operation (600-900 °C) [5, 22, 24]. Intermediate temperature SOFC operation allows for a wider range of materials and more cost-effective fabrication, also in relation to the balance of plant (BoP).

As mentioned, SOFCs operate at relative high temperatures, because the conductivity of oxygen ions through the electrolyte material improves with increasing temperature. An additional advantage is that the chemical and transport kinetics are faster compared to low temperature fuel cells, this results in less irreversible losses. But it should be noted that these high operating temperatures also lead to a lower Nernst voltage. Nernst voltage and irreversible losses are explained in next section. Moreover, a relative high operating temperature ensures that SOFCs don't need an expensive catalyst as platinum which is used in other fuel cell types, and makes the SOFC also suitable for utilizing CO as fuel and supports suitable conditions for internally reforming hydrogen-rich fuels. More information about reforming reactions is provided in section 2.1.4. Disadvantage of high temperature fuel cell operation compared to low temperature fuel cells (PEM) are long start-up times, stringent material and structure requirements, and complex system integration.

Two main SOFC designs are commonly built: tubular and planar. Currently most developers are focusing on planar design, since this design has lower electrical resistance than tubular design. For planar SOFCs co-, counter- and cross-flow configurations are used. Co-flow is currently receiving most attention, because of the easy monitoring of temperature gradients and absence of dangerous hot spots [25].

Within planar SOFCs two type of structures are mostly applied: electrolyte-supported and electrode-supported. In electrolyte supported SOFCs the electrolyte is the thickest layer and works as the supporting structure. This type of structure is suitable for high temperature operation, where Ohmic losses are less dominant. Electrode-supported SOFCs have been designed in order to minimize Ohmic losses for intermediate temperature operation, where the electrolyte has a smaller thickness and hence better supports ionic conductivity. In electrode-supported SOFCs one of the two electrodes is the thickest component and supports the structure.

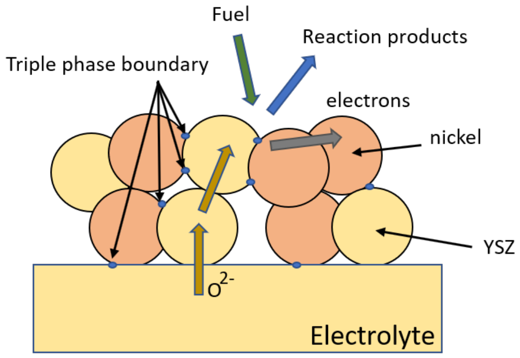

Figure 2.3: Triple phase boundary anode side.

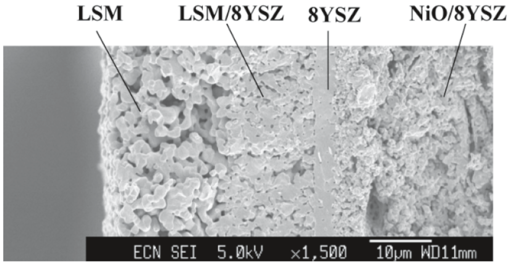

Figure 2.4: Cathode, electrolyte, anode layer of single cell [22].

2.1.2. SOFC pre-reforming and internal reforming

Usually, in case of SOFC operation, hydrocarbon fuel (e.g. methane) needs to be converted into a hydrogen-rich gas required for the electrochemical reaction. Indirectly converting hydrocarbons is done in an external fuel processing system, such as a catalytic steam reformer (pre-reformer) or partial oxidation reactor [5]. In case of a pre-reformer, heat is required to drive the steam reforming reaction. This heat can be obtained by burning anode off-gas left-over fuel or can be extracted from another source (heat integration). Depending on the operating conditions, the heat for the pre-reformer can vary from 40 % to 70 % of the total heat produced in the fuel cell [26]. Partially internal reforming inside the fuel cell reduces the requirement for an external reformer significantly and leads to a more efficient and compact overall system design.

There are two methods of internal reforming within an SOFC: indirect internal reforming (IIR) and direct internal reforming (DIR), they are illustrated schematically in figure 2.5. At IIR, the reformer is in thermal contact with the anode channel, but separated from the cell. At DIR, the fuel reforming is conducted directly into the fuel channel, where the material of the anode electrode acts as a catalyst [5]. An advantage of IIR is that the reformer and cell environment do not have a direct physical effect on each other, however the conversion of methane to hydrogen is not carried out to the same extent as in DIR. For a DIR configuration, part of the steam required for the reforming reaction is obtained from the fuel cell electrochemical reaction. Due to the continuing consumption of hydrogen, the equilibrium of the reforming reaction may be shifted to the right and increases methane conversion.

Two problems are related to DIR-SOFC operation. First: the risk of carbon formation in several areas of the system where hot fuel gas is present. For example, methane will decompose when heated in the absence of air or steam at temperatures above 650 °C via pyrolysis reactions of the type [5]:

$$\mathrm{CH_4} \longrightarrow \mathrm{C} + 2\,\mathrm{H_2} \tag{2.1}$$

A commonly applied procedure to reduce the risk of carbon formation is to carry out some pre-reforming of the fuel gas before it is fed to the SOFC. The advantage of pre-reforming is that higher hydrocarbons, which are more reactive than methane, are preferentially converted into hydrogen. Second: the large temperature gradient in the SOFC stack caused by strong cooling effects of the fast steam reforming reactions at the inlet of the fuel channel [27]. A certain amount of external (pre-)reforming ensures that no excess thermal stress is placed at the SOFC stack. In summary: a combination of pre-reformer and DIR is often applied to have the benefits of DIR, while reducing the risks of carbon depositing with pre-reforming.

2.1.3. SOFC electrochemistry

The output power of a fuel cell is equal to voltage multiplied by current. The current depends on the hydrogen oxidation reaction and is explained in next section. The final cell voltage is depending on ideal cell voltage and several voltage losses.

Ideal cell voltage is also known as the Nernst voltage or theoretic open cell voltage (OCV) and depends on temperature, pressure, and fuel composition. In practice the OCV is observed to be lower than the ideal

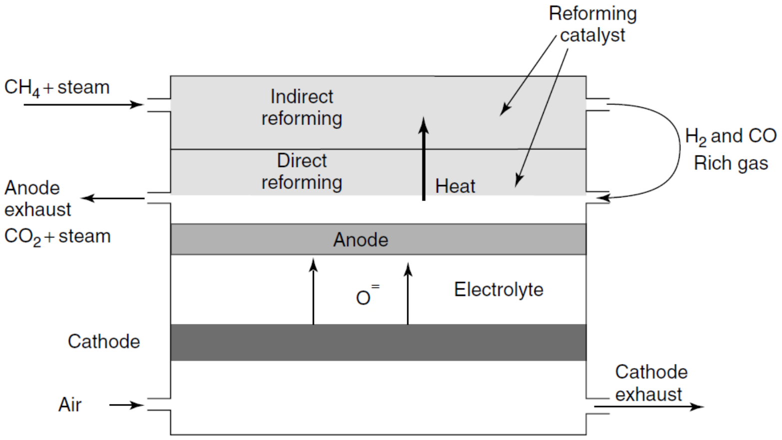

Figure 2.5: Schematic representation of direct and indirect internal reforming. Figure taken from [5].

cell voltage. Thereupon, when drawing a current the cell voltage further drops according to eq. 2.2. Figure 2.6 depicts the operational cell voltage against the drawn current density ($\mathrm{A\,m^{-2}}$). The characteristic shape of this figure results from three irreversibilities: activation losses, concentration losses and Ohmic losses. The starting point of this curve depends on the crossover losses. Equations for Nernst voltage and polarization loss calculations are provided in appendix A.

$$V_{cell} = E - \Delta V_{act} - \Delta V_{conc} - \Delta V_{ohm} \tag{2.2}$$

In eq. 2.2 represents: E is the Nernst voltage, ΔV_{act} the activation voltage loss, ΔV_{conc} the concentration voltage loss, and ΔV_{ohm} the Ohmic voltage loss.

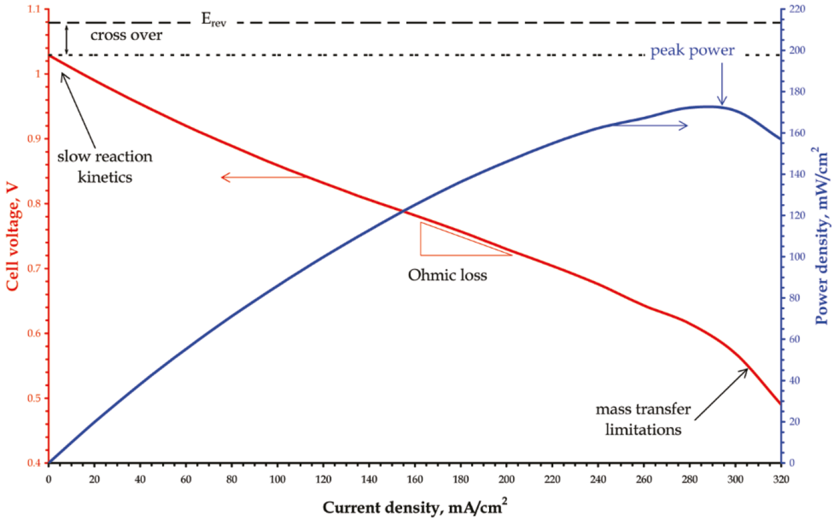

Figure 2.6: SOFC V-i curve with the origin of potential losses (red line) and power density (blue line) [22].

2.1.4. SOFC chemistry and reforming kinetics

The working principle of an SOFC is shown in figure 2.7. In this figure the chemical reactions concerning SOFC operation (including direct internal reforming) are schematically depicted. The corresponding reaction equations are provided in table 2.1.

In the fuel channel two reactions take place: methane steam reforming (MSR) and water-gas shift (WGS). These are the DIR reactions. The Hydrogen oxidation reaction (HOR) takes place at the the anode-electrolyte-TPB. The three main reactions are explained in more detail in next paragraphs.

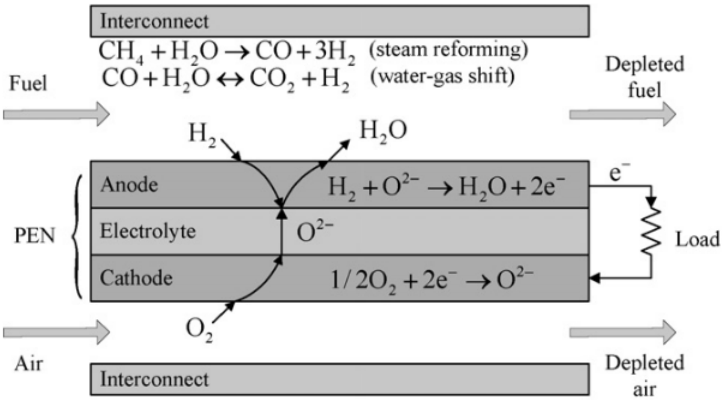

Figure 2.7: Schematic diagram of planar DIR-SOFC [28].

Table 2.1: Reactions SOFC-DIR. Δh^0 at $T^0 = 25°C$ and $p^0 = 1$ bar.

Id.	Reaction name	Reaction equation	Location	Δh^0 J mol^{-1}
MSR	Methane steam reforming	$CH_4 + H_2O \longrightarrow CO + 3\,H_2$	Fuel channel	206100
WGS	Water-gas shift	$CO + H_2O \longleftrightarrow CO_2 + H_2$	Fuel channel	-41150
-	Hydrogen oxidation	$H_2 + O^{2-} \longrightarrow H_2O + 2\,e^-$	Anode TPB	-
-	Oxygen reduction	$\frac{1}{2}O_2 + 2\,e^- \longrightarrow O^{2-}$	Cathode TPB	-
HOR	Hydrogen electrochemical oxidation	$H_2 + \frac{1}{2}O_2 \longrightarrow H_2O$	-	-241800

Methane steam reforming reaction rate

Methane steam reforming in the fuel channel (DIR) is an endothermic reaction, heat is required to drive the reforming process. The required reaction heat can be recovered from the fuel cell itself or from a separate heat source. Steam required for methane steam reforming is present, because steam is a product of the hydrogen oxidation reaction.

The reaction rate of MSR at SOFC anodes is a widely studied research topic, an extensively variety of fit equations and experimental parameters to express the kinetics can be found. Bao et al. [29] listed some representative expressions of the MSR and WGS reaction. Within this list the area specific MSR kinetic relation found by Achenbach and Riensche (eq, 2.3 [27]) is the most used one in comparable research [26]. This relation is based on experiments on a Ni–YSZ cermet surface.

$$r_{MSR} = k_{MSR} \cdot p_{CH_4} \cdot \left(1 - \frac{p_{CO} \cdot p_{H_2}^3}{p_{CH_4} \cdot p_{H_2O} \cdot K_{eq,MSR}}\right) \cdot exp\left(-\frac{E_a}{RT}\right) \tag{2.3}$$

Where r_{MSR} is the reaction rate (mol m^{-2} s^{-1}), E_a is the activation energy of the steam reforming reaction (82 kJ mol^{-1}), p_i the species partial pressure in the channel in bar, k_{MSR} is the steam reforming reaction constant (=4274 mol s^{-1} m^{-2} bar^{-1} [27]). The equilibrium constant $K_{eq,MSR}$ depends on the change of Gibbs free energy, specific gas constant, and temperature.

Water-gas shift reaction rate

WGS reaction takes place in the fuel channel and takes care of the reduction of carbon monoxide. Although carbon monoxide can be electrochemically oxidised, it is often assumed that it is not directly oxidized and only converted by the WGS reaction [26]. In the WGS reaction the carbon monoxide reacts with water vapour to carbon dioxide and hydrogen. WGS is a moderate exothermic process. At higher temperatures the reaction rate is higher. The WGS reaction is fast and hence this reaction can be considered at equilibrium [26]. The equilibrium-limited WGS reaction rate expression is given eq. 2.4.

$$r_{WGS} = k_{WGS} \cdot p_{CO} \cdot \left(1 - \frac{p_{H_2} \cdot p_{CO2}}{p_{H_2O} \cdot p_{CO} \cdot K_{eq,WGS}}\right) \tag{2.4}$$

Since the WGS reaction (r_{WGS} $\mathrm{mol\,m^{-2}\,s^{-1}}$) is fast, the WGS reaction constant k_{WGS} is arbitrarily high [26]. The equilibrium constant $K_{eq,WGS}$ depends on the change of Gibbs free energy, specific gas constant, and temperature.

Hydrogen electrochemical oxidation reaction rate

The HOR is the chemical reaction responsible for electricity production. If the required current density (i) is set, Faraday's law of electrolysis relates the flux of reactants and products to this electric current density. According to this law, and when only hydrogen oxidation is present[1], the amount of H_2 and H_2O produced is described by eq. 2.5.

$$r_{HOR} = \frac{i}{2F} \tag{2.5}$$

Where r_{HOR} is the reaction rate ($\mathrm{mol\,m^{-2}\,s^{-1}}$), i is the current density ($\mathrm{A\,m^{-2}}$) and F the Faraday constant ($\mathrm{C\,mol^{-1}}$).

2.1.5. SOFC fuel utilization and anode off-gas recycling

Fuel is never completely utilized in an SOFC. The ratio of fuel consumption for electrochemical power generation to fuel supply is called fuel utilization U_f. Fuel utilization is one of the main variables determining SOFC system efficiency and functional SOFC lifetime.

Operating fuel cells at high fuel utilization is required in SOFC standalone systems to achieve high system efficiency. Such systems operate at around 90 % fuel utilization. Operating the SOFC at higher fuel utilization is challenging due to greater degradation risks, because of unequal fuel distribution over the active cell area, hydrogen depletion leads to oxidation of the anode material (fuel starvation). This degradation mechanism reduces the catalytic activity and increases the polarization losses [30–32]. Besides, 100 % fuel utilization is also impossible, because the cell voltage adjusts to the lowest chemical potentials for the gas mixture at the exit of the anode and cathode chambers. To maintain the chemical reactions, there must be fuel at the exit of the anode.

Recycling part of the anode off-gas is a commonly used solution to achieve high SOFC stand-alone system efficiencies while using low single pass fuel utilization ($U_{f,sp}$). When anode off-gas recycling is implemented, the SOFC anode exhaust gas is partially returned to the pre-reformer and recycled. The net fuel utilization ($U_{f,net}$) is kept on a high ratio, which explains an higher efficiency. Moreover, water vapour present in the AOG is used for methane steam reforming in the pre-reformer and can contribute to reduce external steam supply. To summarize, the achieved SOFC efficiency improvement by AOG recycling depends on the recycling ratio, net fuel utilization, and additional recycling pump losses (blower or ejector). The anode off-gas recycling ratio is defined as in eq. 2.6.

Another solution for achieving high efficiency, while extending fuel cell lifetime by holding acceptable fuel utilization is SOFC operation in a hybrid system. This a reason for present research.

$$AOGRR = \frac{\dot{N}_{AOGR}}{\dot{N}_{SOFC\ out}} \tag{2.6}$$

2.1.6. SOFC modeling

To improve performance and keeping experimental costs low, engineering research mostly relies on the mathematical representation of the physical system under investigation. This is also the case for SOFC- design, optimization, control, and diagnostic purposes. Depending upon the application, different levels of model details are described in literature. A good summery of the development of SOFC models is presented by Marra [25].

On topside of the model hierarchy are the highly detailed physical models. With the aid of computational fluid dynamics (CFD) the conservation and physical relations are solved for a discretized representation of the fuel cell. This type of modeling is accurate, but complex and requires a firm computational capacity. On the other side of the hierarchy are the black-box models. Black-box models correspond to a purely mathematical description of the phenomena and do not rely on physical governing equations. This type of modeling can be accurate and fast, however their working principle relies on performed experiments in order to map output data to input data. Regression and neural networks are typical examples of black-box models.

---

[1] This relation relies on the fact that solid electrolytes such as YSZ are pure ionic conductors, and so only oxygen ions can permeate through the electrolyte to take part in the oxidation reaction at the anode electrolyte triple phase boundary.

In the centre of the modeling hierarchy are the 1-D models and 0-D models (lumped parameter models). 0-D models have been the center of attention and have been largely used for system studies. The great benefit of using 0-D models is simplicity of model development and short calculation time. However, the disadvantage is that they can only account for mean values of parameters (current density, composition, and temperature) and it follows that more detailed investigation of the cell is needed to check for undesirably effects such as locally exceeding temperature limits and carbon formation. Moreover, a 0-D model is not able to predict spatial evolution of parameters in stream wise direction. Although a 0-D model has no spacial parameter distribution in stream wise direction, perpendicular to stream wise direction the model is represented by a number of layers. Figure 2.8 illustrates a single cell model composed out of four layers: interconnect, fuel channel, PEN structure, air channel. The conservation laws and constitutive relations are solved for each layer to predict cell performance.

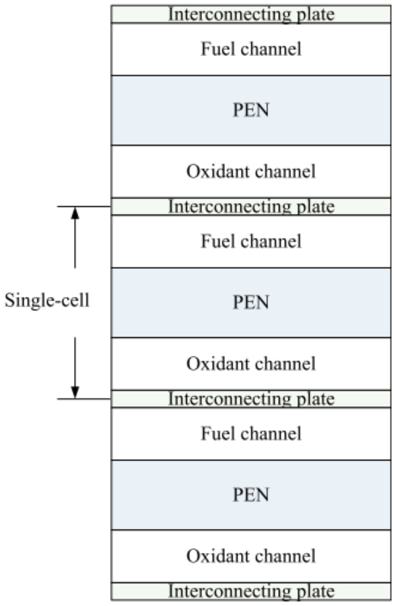

Figure 2.8: Schematic side view of 3 stacked SOFC cells with 5 layers in each single cell [33].

A significant part of in literature described 0-D models rely on experimental data for calibrating computed output results. For example, in ref.[34] look-up tables with experimentally obtained voltage losses are invoked during simulation. A reference is made to ref. [31, 34–37] for more details about lumped modeling supported by experimentally obtained data. 0-D models only based on first principles are less commonly described. The only model found by this author is developed by Qi et al. [38], but this 0-D tubular SOFC model has not been validated, so the accuracy is unknown.

2.2. Internal Combustion Engine

Internal combustion engines transform chemical energy stored in fuel into thermal energy by a combustion reaction. Successively the thermal energy is converted into mechanical energy. The gaseous products of combustion are acting on the moving surfaces of the engine, such as the face of a piston in reciprocating engines or on a turbine blade in a continuous combustion engines. In this work the term internal combustion engine (ICE) is representing the reciprocating internal combustion engine.

When considering reciprocating internal combustion engines there are many different types. A first classifying feature can be the type of fuel used in the engine. From the type of fuel, the method of ignition (spark ignition or compression ignition) and combustion characteristics are following. Another classifying feature can be the working cycle of the engine, 2-stroke or 4-stroke engines are the most common engine cycles. In present work only 4-stroke engine are considered.

The complete process of a 4-stroke engine is as follows: when the inlet valve is open (IO) air flows into the cylinder until the inlet valve closes (IC). When all valves are closed, the piston moves upwards and the cylinder content is compressed. After compression, around the point where the piston reached top dead centre (TDC), combustion takes place and the gas pressure in the cylinder forces the piston down. This is the working stroke of the cycle. Before the piston reaches bottom dead centre (BDC) the exhaust valve opens (EO) and the gas exhausts until the valve closes (EC).

2.2.1. In-cylinder process

The process between the closure of the inlet valve (IC) and the opening of the exhaust valve (EO) is called the in-cylinder process and comprising: compression, combustion and expansion. The in-cylinder process can be explained by a Seiliger process model. The Seiliger process characterizes the engine process effectively into stages as listed below and as depicted in the p-V diagram in figure 2.9 [1].

- 1-2: Polytropic compression.
- 2-3: Isochoric combustion.
- 3-4: Isobaric combustion.
- 4-5: Isothermal combustion and expansion.
- 5-6: Polytropic expansion.
- 6-1: Heat rejection to the environment.

Using Seiliger, the in-cylinder process is specified by a number of parameters. Parameters a, b, and c are combustion parameters indicating the three combustion phases respectively. The polytropic exponent n_c and effective compression ratio r_c describe the polytropic compression phase. The polytropic exponent n_e and expansion ratio r_e describe the expansion phase. When these parameters are known, together with initial conditions (or trapped conditions) and thermodynamic properties of the working medium, the obtained work per Seiliger stage can be calculated. The mathematical description of Seiliger parameters is provided in table 2.2. V is the stroke volume, p is the pressure, and T the temperature.

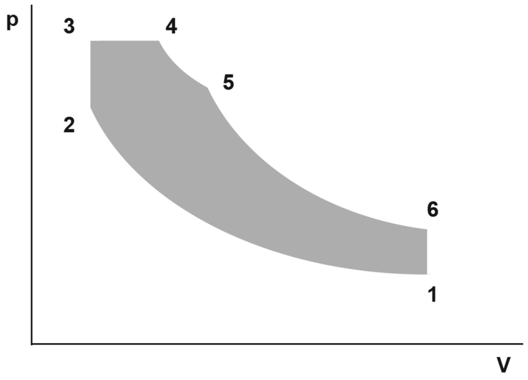

Figure 2.9: Typical six stage Seiliger plot, pressure versus volume diagram, taken from [1].

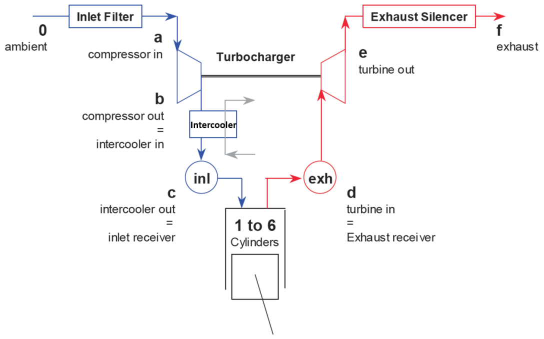

Figure 2.10: Station numbering, figure taken from [1].

2.2.2. Gas exchange process

The processes between the opening of the exhaust valve (EO) until the closure of the inlet valve (IC) are part of the gas exchange process and comprising: air induction, blowdown, gas exhaust, and scavenging [1]. The process stations concerning the gas exchange process are labelled 'a' to 'e' in figure 2.10. Air induction and scavenging are further examined since these processes are deviating from regular diesel engine operation.

Considering air induction, in case of diesel engine, only air is compressed and the fuel is directly injected into the combustion chamber around TDC. For a gas engine the air induction can be combined with fuel admission. When the gaseous fuel is injected at the inlet manifold or before the turbocharger, it is called homogeneous charge (HC). This principle is illustrated in figure 2.11 and 2.12. Other types of fuel admission principles for gas engines are: port injection, where the gas fuel and air are mixed in the inlet ports and cylinder, low-pressure direct injection, where the gas fuel is injected into the cylinder early during the compression stroke when the pressure is low, and high-pressure direct injection, where the gas fuel is injected into the burning pilot fuel (duel fuel ignition, next sub-section).

Table 2.2: Seiliger process parameters and definition, taken from [1].

Seiliger stage	Parameter	Parameter definition	Seiliger definition
1-2	r_c, n_c	$\frac{V_1}{V_2} = r_c$	$\frac{p_2}{p_1} = r_c^{n_c}$
2-3	a	$\frac{p_3}{p_2} = a$	$\frac{V_3}{V_2} = 1$
3-4	b	$\frac{V_4}{V_3} = b$	$\frac{p_4}{p_3} = 1$
4-5	c	$\frac{V_5}{V_4} = c$	$\frac{T_4}{T_5} = 1$
5-6	r_e, n_e	$\frac{V_6}{V_5} = r_e$	$\frac{p_5}{p_6} = r_e^{n_e}$

The scavenging process is preferably not applicable for gas engines when the gas fuel is injected at the inlet manifold or before the turbocharger (HC). If scavenging is present in such engines, a valve overlap (inlet and exhaust valves are open) pushes the exhausted gas-charge out of the cylinder and draws in a fresh charge of air-fuel mixture for the next cycle. In this case, a small portion of fresh charge (including fuel) will slip through from the inlet to the exhaust port during the valve overlap period. In literature this is called methane slip, which is an emission. A disadvantage of missing the scavenging process is a reduced engine's efficiency. The amount of residual gas from previous cycle limits the amount of fuel and fresh air which can be swallowed into the new cycle. Moreover, without scavenging the exhaust valve temperature can become critical since no air stream is cooling the valve.

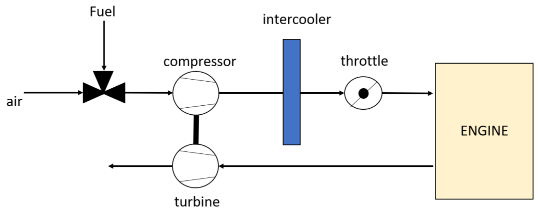

Figure 2.11: Fuel admission before turbocharger.

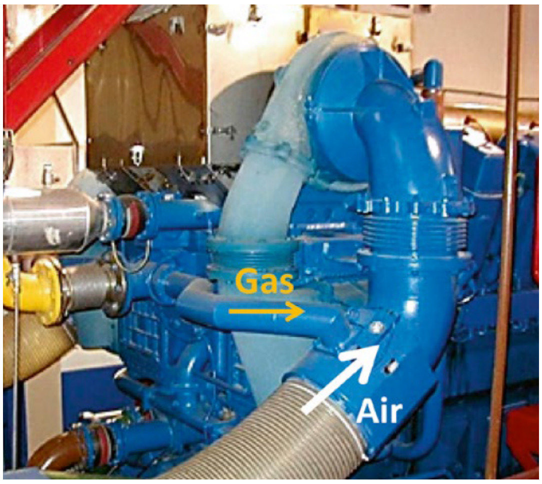

Figure 2.12: Homogeneous charged gas engine; gaseous fuel injection before turbocharger [39].

2.2.3. Ignition

There are different types of ignition within gaseous fuelled reciprocating engines. The most common are: gas-only spark-ignition (SI) and duel-fuel compression ignition (CI). Since the self-ignition temperature of natural gas is too high to be reached by a regular compression cycle in the cylinder, the combustion must be initiated by an ignition source. Engines running only on gas use a spark plug to initiate the combustion process. Dual fuel engines use a pilot fuel to start the combustion process. A small amount of pilot fuel (< 1 %) is injected into the cylinder, where it is ignited by the high temperature of the air mixture at the end of compression cycle.

A novel and advanced method is homogeneous charge compression ignition (HCCI) and often associated with SOFC-ICE hybrid systems. HCCI is a mode of combustion in which a (diluted) premixed gaseous air-fuel mixture is supplied into the cylinder and is compressed by the piston so that the gas temperature and pressure are high enough to induce auto-ignition of the premixed mixture. HCCI is generally regarded as a promising technology for future power generation concepts. Due to high compression ratio and fast combustion it allows the engine to operate with high thermal efficiency and very low emissions of particle matter and NO_x [40–43]. However HCCI operation has been known for more than thirty years, it is not applied in commercial applications. Significant technical challenges must be overcome before HCCI engines become practice. Technical challenges such as: controlling ignitions timing over a range of speeds and loads (operation between knock and misfire), and extending the operating range to high loads. Particularly the latter challenge excludes HCCI engines for marine applications at this moment [39–41, 44, 45].

2.2.4. Gas engine operation - air excess ratio

In literature, it has been reported that the use of natural gas as a fuel already leads to a significant reduction of emissions compared to diesel fuelled engines [46–48]. The low carbon to hydrogen ratio of natural gas reduces the carbon-based emissions and the low combustion rate of natural gas combined with lean air-to-gas ratio engine operation increases efficiency and reduces NO_x emissions. As is depicted by the red line (NO_x) and orange line (thermal efficiency) in figure 2.13.

Combustion is considered lean when excess air is introduced into the engine along with the fuel. In lean operations the important parameter in the process is the air-to-gas ratio or λ. In stoichiometric natural gas engines $\lambda = 1.0$ and in lean-burn engines ($\lambda > 1.0$). In lean-burn engines the combustion process is enhanced by pre-mixing the air and fuel upstream of the turbocharger before introduction into the cylinder (HC).

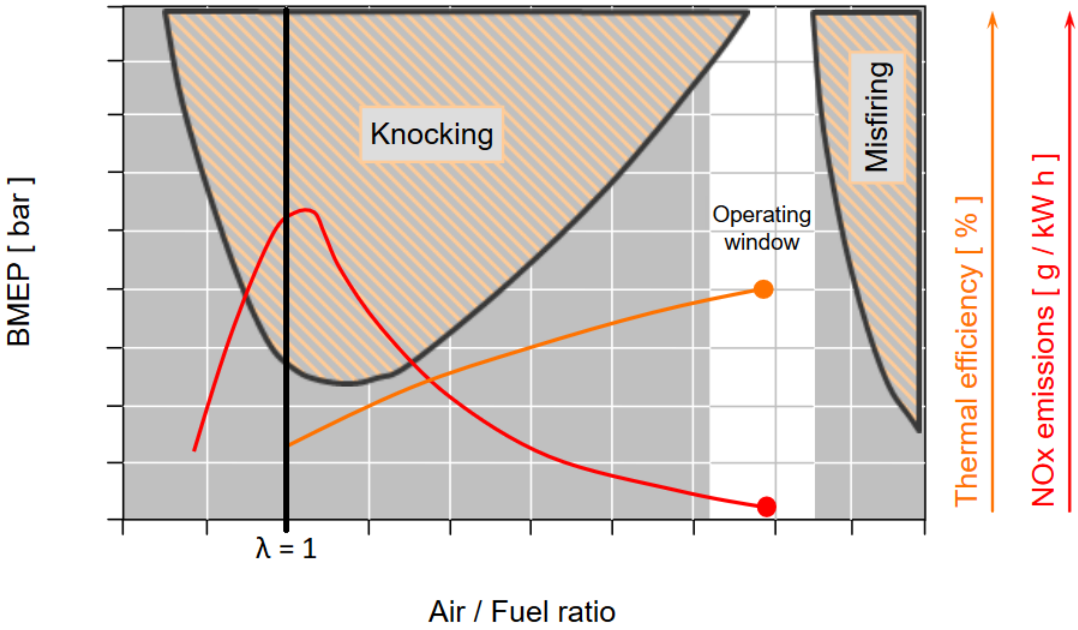

Figure 2.13: Detonation chart with optimal operating window of a lean-burn gas engine. Taken from *Wärtsilä*.

Lean-burn gas fuelled engines carry some disadvantages: lean air-to-gas mixtures slow down the flame propagation speed, and increase the cycle-to-cycle variations (engine misfire) because the lean mixture is harder to ignite. Engine operation with richer air-to-fuel mixtures is restricted by detonation or knock [2] [49]. To obtain a stable combustion process, the combustion is restricted within a narrow operating window between knock and misfire. As can be seen in figure 2.13 the operating range of a gas fuelled engine is limited by substantial knock and misfire areas. This narrow operating window results in limiting transient capabilities of the marine natural gas engine. This is the reason that natural gas engines for marine applications are preferably restricted to generator applications compared to conventional diesel engines.

2.2.5. Effects of anode off-gas on engine performance

Apart from natural gas, H_2 and CO_2 are the most important species of the engine intake fuel, when considering AOG-natural gas blends. The effects of H_2 and CO_2 on ICE performance are discussed in next paragraphs. It

---

[2] Knock is the name given to the noise which is transmitted through the engine structure when essentially spontaneous ignition of a portion of end-gas occurs. End-gas is the fuel, air, residual gas, mixture ahead of the propagating flame[49].

is assumed that anode off-gas H_2O-vapour is removed from the fuel blend in order to reduce the amount of fuel bound inert species and keeps flame speeds on acceptable levels for SI operation. H_2O-vapour can be removed by cooling the fuel such that water is condensed.

Hydrogen effects on engine performance

Mixing natural gas with fuels that posses faster burning speeds and a smaller ignition energy is an effective way to help reduction of combustion duration and increase combustion rate and so reduces cyclic variations[3]. Hydrogen has approximately eight times the laminar flame speed and lower ignition energy compared to that of natural gas [17].

Previous research has been focused on hydrogen-enrichment for purposes in the automotive industry, the results indicate that hydrogen addition in natural gas engines can reduce engine emissions and can enhance operation limits [16–19]. Sapra et al. [20] investigated the effects of hydrogen-natural gas for marine applications by performing experiments where natural gas is replaced with 10 volume-% and 20 volume-% hydrogen. This research is a relevant addition to the automotive industry's research, because the addition of hydrogen to natural gas has a direct effect on NO_x emissions. The emission regulation for marine engines is different than those for automotive engines and hence demarcate a different operating window [50]. Furthermore, the operating window between knock and misfire gets narrower when increasing brake mean effective pressure (BMEP) (figure 2.13). Higher BMEP is of increasingly interest for marine engines, as modern marine engines operate at very high BMEP of 30 bar ($W\ddot{a}rtsil\ddot{a}$ [51]).

In ref.[20] it is found that the high combustion rate of hydrogen improved combustion stability, which allowed for better air-excess ratio control and allowing higher air-excess ratios (leaning), hence extending the limited operating window. Moreover it is shown that hydrogen addition improved brake thermal efficiency by 1.2 %, while keeping NO_x emissions below the marine emission regulations.

CO and CO_2 effects on natural gas engine performance

There are no previous studies found on the effects of CO and CO_2 addition to natural gas on marine engine performance. Considering CO, the effects on engine performance are unknown as of yet. Considering CO_2, studies describing the effects of CO_2 when exhaust gas recirculation (EGR) is applied can be illustrative.

EGR is an effective technique available for reducing NO_x emissions in internal combustion engines. EGR works by recirculating a part of the engine's exhaust gas back to the engine's air intake. This exhaust gas recirculation provides CO_2 and H_2O vapor at the intake of the engine cylinder.

Three effects are explaining the impact of EGR and can be compared with the effects of blending AOG-CO_2 with natural gas in present work [52]. Although this section presents no quantitative results, the qualitative effects should be in mind when designing SOFC-ICE hybrid system configurations.

1. The dilution effect: the intake oxygen concentration is reduced by replacing the intake air with CO_2 and H_2O-vapour. This component replacement lowers the oxygen availability in the engine cylinder, increasing the mixture time, increasing ignition delay, and results in lower flame temperature and flame speeds (decreasing the net reaction rate).

2. Thermal effect: the addition of CO_2 and if present H_2O vapor increases the heat capacity of the in-cylinder charge, leading to lower flame temperature during the combustion process. Due to lower flame temperatures, NO_x emissions reduce and knock limits expel. However, it decreases also BMEP and destabilize the combustion which leads to engine misfire (higher cycle-to-cycle variability and poor combustion phasing).

3. The chemical effect: the endothermic dissociation of CO_2 and H_2O-vapour lower the flame temperature and flame speeds.

2.2.6. ICE modeling

Internal combustion engine modeling can be categorized by the same level of details as defined for SOFC modeling. The extent of underlying physical principles determines the level of details considered in the model.

On top of the hierarchy are computational fluid dynamic combustion models (CFD) and multi-zone combustion models. CFD models are basically intended to accurately model the processes in the cylinder by discretizing the combustion chamber in a large number of elements. The mass, momentum, and energy

---

[3] Cycle-by-cycle variations in cylinder pressure versus time measurements [49].

balances, and chemical reaction rate equations are solved for these elements. CFD combustion models are used to gain more detailed insights into the heat transfer process in the cylinder during combustion, e.g. to predict soot formation and NO_x production [53]. A multi-zone combustion model is a variant of the CFD model, which uses a smaller number of elements (zones). Multi-zone models are also used to predict NO_x formation [54].

On the other side of the modeling hierarchy are empirical models. These models are purely based on mathematical equations derived from experiments. These models are developed to predict engine parameters as torque and fuel consumption and are used to analyse the behaviour of one specific engine. Due to the dependency of measured data these models are not able to run simulations when changing specific engine parameters (e.g. load scaling up or down).

In the centre of the model hierarchy are the filling and emptying engine models (FE) [55], and the mean value first principle engine models (MVFP) [56]. In the FE model the various subsystems of the engine are modeled as control volumes in its entirety (e.g. combustion chamber, intake, exhaust, piping). For each control volume the mass and energy conservation laws are considered. The time step is in the order of a crank angle. Based on the FE approach are the MVFP models. In MVFP engine models the time step is one engine revolution (cycle), which means that the crank angle subsystem process values are replaced by mean values per cycle. Because of the cycle time scale, MVFP models can quickly and efficiently simulate the complete turbocharged engine system, which make them very suitable for integration in a larger system model, such as the drive train of a ship or an hybrid power plant system.

A simplified variant of MVFP modeling uses pre-defined Seiliger parameters to characterize the in-cylinder process. This is possible when knowing the cylinder initial conditions and the thermodynamic state of the cylinder content (e.g. by experiments). How to characterize combustion phases and define Seiliger parameters based on experimentally obtained engine data is extensively discussed by Ding in ref. [57]. A MVFP model proposed by Ding et al. in ref. [58] uses the MVFP approach for the inlet and exhaust receiver control volumes in combination with compressor and turbine maps and extensive calibration. Geertsma et al. [59] modified this MFVP model such that it can be calibrated with measured engine data and thus without compressor and turbine maps and extensive heat release measurements as proposed in ref. [58]. This makes this modified MFVP model strategy employable with less detailed engine information and suitable for this system level research.

2.3. Marine power plants

On board a ship, propulsion and electric power supply are two important functions that need to be performed to fulfil the ship's mission. When an all-electric concept is considered, this means that the propulsion is driven by an electric motor, the power supply for the electric propulsion and for other electrical systems has to be delivered by a power plant.

Van Biert et al. [60] performed a literature review to the suitability of fuel cells for marine applications and compares fuel cell systems to convectional marine power plant solutions according to the criteria listed below. These criteria should be kept in mind when designing SOFC-ICE hybrid system configurations. For further information the original text from van Biert et al. [60] is recommended.

1. Power and energy density.
2. Load transients and system start-up.
3. Environmental impact.
4. Safety and reliability.
5. Economics.

2.4. SOFC-ICE hybrid systems

This section presents a review of previous studies performed on SOFC-ICE hybrids systems. Since SOFC-ICE integration is a novel technology, not much research has been published as of yet. The here mentioned studies are the only relevant publications on found.

Park et al. [7] proposed a hybrid system where an SOFC stack was combined with an HCCI internal combustion engine. In this hybrid system the HCCI engine replaces the conventional combustor and burns the anode off-gas to produce additional power. Park et al. conducted steady state simulations and demonstrated an electrical efficiency of 59.5 % (103.6 kWe) at a power split of 12.7 %-ICE, 87.3 %-SOFC and a SOFC fuel utilization of 75 %. This result is promising, however certainly more detailed research is required to make this concept feasible. Park's work can be seen as an preliminary study on SOFC-ICE hybrid system.

Elaborating on Park's study, Kang and Ahn [61] developed a dynamical model of the by Park proposed hybrid system and studied the dynamic behaviour during transients. The simulation results were clearly indicating the different time scales of the SOFC and the engine. For the SOFC it took more than one hour to reach a new thermal steady state value after a load change, while the engine reached steady state at each cycle. The in this study imposed load changes were affecting AOG composition and successively affecting engine performance. As explained, the HCCI engine was only fuelled by anode off-gas, this means that no fuel by-pass with additional fuel supply to the engine was designed. To improve dynamic load capabilities of the complete system a fuel by pass (e.g. additional supply to engine) is expected to be necessary. In the study of Kang and Ahn no efficiency calculations were reported.

Van Biert et al. [13] conducted a thermodynamic comparison study of SOFC-combined cycles. Relevant for this work are the simulations conducted with the SOFC- spark-ignited reciprocating engine bottoming cycle model. In this study no fuel by-pass to the engine was present. The simulations results were inducing the interest for further research. In the computational simulations a maximum system electrical efficiency of 64 % was achieved at a SOFC fuel utilization of 90 % (electric power was not reported) and at a power split of 5 %-ICE, 95 %-SOFC.

Chuahy and Kokjohn [14] developed an SOFC-ICE hybrid system and conducted a system level optimization strategy to predict the maximum performance achievable by the integrated system. Thereupon HCCI engine experiments were conducted to validate if the ICE was capable of operating with the predicted conditions. The authors predicted an electric efficiency of 70.9 % with the computational model (1104.3 kWe, at a SOFC fuel utilization of 64.4 % and a power split of 14.7 %-ICE, 85.3 %-SOFC), but they reported practical problems with stability during HCCI combustion and even during RCCI combustion[4]. These problems made them finally conclude to investigate future SOFC-hybrid system research in spark-ignition combustion. Chuahy and Kokjohn [14] were expecting SI combustion as a more stable and robust mode of combustion for SOFC-ICE hybrid systems. This final conclusion is important for current research.

An experimental study only focused on the engine part of the SOFC-ICE hybrid system was carried out by Choi et al. [62]. Choi conducted experiments with an HCCI engine fuelled with anode off-gas. He finally achieved operation but it was reported that the engine experiments were performed on a small single cylinder engine. Scalability to higher power ratings and dynamic operation of HCCI combustion was assessed as doubtful by Manofsky et al. [41] and Epping et al. [44].

The studies of: Park [7], Kang [61], Choi [62], and Chuahy [14] are all considering HCCI- reciprocating engines as bottoming cycle in the hybrid system. While this type of combustion has been achieved in laboratory setting, HCCI technology is still far away from practical applications, particularly at high specific power outputs [39, 41, 45]. It can be concluded that more research is required before these advanced combustion strategies can be successfully integrated in marine transport applications.

2.5. Conclusion

It is found that a planar, co-flow SOFC design is currently the most applied SOFC type. It is explained that an intermediate operating temperature (600-900 °C) allows for a wider range of materials and more cost effective fabrication. The SOFC structure commonly applied for intermediate temperature SOFCs is an electrode-supported structure. It is found that a combination of methane pre-reforming and direct internal reforming allows high performance with lower SOFC degradation risks.

SOFC electrochemistry is explained, also SOFC chemistry and reforming kinetics are treated. The chemical reactions of interest are methane steam reforming, water-gas shift, and hydrogen oxidation.

In this chapter it is explained that fuel utilization is an important parameter for fuel cell efficiency and fuel cell life time. High fuel utilization leads to high SOFC efficiency, but increases the risks on cell degradation. Anode off-gas recycling is another important operational parameter for SOFC systems. Recycling part of the anode off-gas back to the SOFC anode inlet is a common solution to achieve high system efficiency while operating low single-pass cell fuel utilizations. Also the water-vapour in the anode-off gas recycling stream is re-used for methane steam pre-reforming and reduced external steam supply.

A literature study is conducted to the insights of gas fuelled reciprocating internal combustion engines. The in-cylinder process is explained with the aid of Seiliger parameters. Also the gas exchange processes, ignition,

---

[4] Sort of dual fuel engine combustion technology, where in this case the engines gets an extra burst of natural gas

air excess ratio, and the effects of AOG-natural gas-blending are explained. In literature it is demonstrated that hydrogen addition to natural gas engines improves combustion stability and enhances the engine's thermal efficiency. It is expected that hydrogen available in AOG can have the same improvements. However, also higher cylinder peak pressures and temperatures can be expected and require attention, particularly when considering engine design and NO_x-emission limitations imposed by IMO.

Finally, a literature review of previous SOFC-ICE hybrid system studies has demonstrated the potential SOFC-ICE hybrid systems. The projected SOFC-ICE hybrid system efficiencies in literature are: Park et al.: η_{HS} = 59.5 %, van Biert et al.: η_{HS} = 64 %, and Chuahy et al.: = η_{HS} 70.9 %. Although these results are promising, two observations should be made: all three systems are considering bottoming cycles. This means that the engine is only supplied by anode off-gas, which limits dynamic capabilities. And two out of three studies are considering HCCI engines as combustion strategy, which is currently only achieved in a laboratory setting and is far away form commercial applications.

3

Methodology

The objective of this thesis is to identify operating parameters and system configurations of SOFC-ICE hybrid systems for marine applications and to find their influence on system efficiency and performance. To meet this objective component models are developed and are combined to a hybrid system, thereafter performance simulations are conducted. This chapter describes the model approach and simulation strategy.

3.1. Model approach

3.1.1. Hybrid system configuration

The proposed hybrid system is presented in figure 3.1 and works as follows: natural gas (methane) is partially reformed by flowing through a pre-reformer. The partially reformed fuel enters the SOFC stack to generate electrical power and leaves the stack as anode off-gas. Because the anode off-gas includes a high amount of steam, it flows into a steam separator to remove the water contents by condensing the water-vapour. Then the dehydrated anode off-gas is mixed with an additional amount of natural gas and enters the internal combustion engine to generate additional electrical power. The amount of natural gas flowing into the engine will depend on the power demand. Controller II controls this amount of natural gas depending on the equivalent fuel proportion of anode off-gas from the SOFC.

Anode off-gas recycling can be applied to increase net SOFC fuel utilization and to reduce the pre-reformer external steam requirement (for MSR). Heat from the engine exhaust and steam separator is used to produce the external steam required of the pre-reformer. On the cathode side; ambient air enters the heat exchanger and is heated by the cathode exhaust air of the SOFC stack. Fuel pre-heating is carried out by heat exchange with anode-off gas. Direct current (DC) produced in the SOFC must be treated with power conversion equipment to convert it to grid-compliant alternating current (AC) of suitable voltage and frequency.

In contrary to the configurations treated in previous studies (chapter 2.4), where the engine is only fuelled with anode off-gas (bottoming cycle), in this work an additional natural gas supply is mixed with anode-off gas before it is introduced into the engine (combined cycle). This additional fuel supply before engine intake increases power redundancy, improves system dynamic capabilities, shortens start-up times, reduces power density and allows for operating at several power split options.

3.1.2. SOFC and pre-reformer model

To study hybrid system performance, an SOFC model is required to determine the effects of different SOFC designs and operation parameters. The SOFC model has to solve conservations and constitutive equations to compute SOFC performance and outlet properties. The SOFC input conditions are: fuel and air composition, temperature, and pressure. The control parameters are: current density, fuel utilization, and air excess. The model is simulating a planar, anode supported, co-flow, intermediate temperature SOFC model including direct internal reforming, as selected by the literature study. The computing time of the model has to be short, therefore a 0-D modeling approach is selected.

As part of the SOFC system a pre-reformer model is required. This model has to compute pre-reformer fuel output based on control parameters such as: methane pre-reforming ratio, pressure, temperature, and oxygen to carbon ratio. The pre-reformer input is the natural gas supply and optionally recycled anode off-gas. The models are explained in chapter 4.

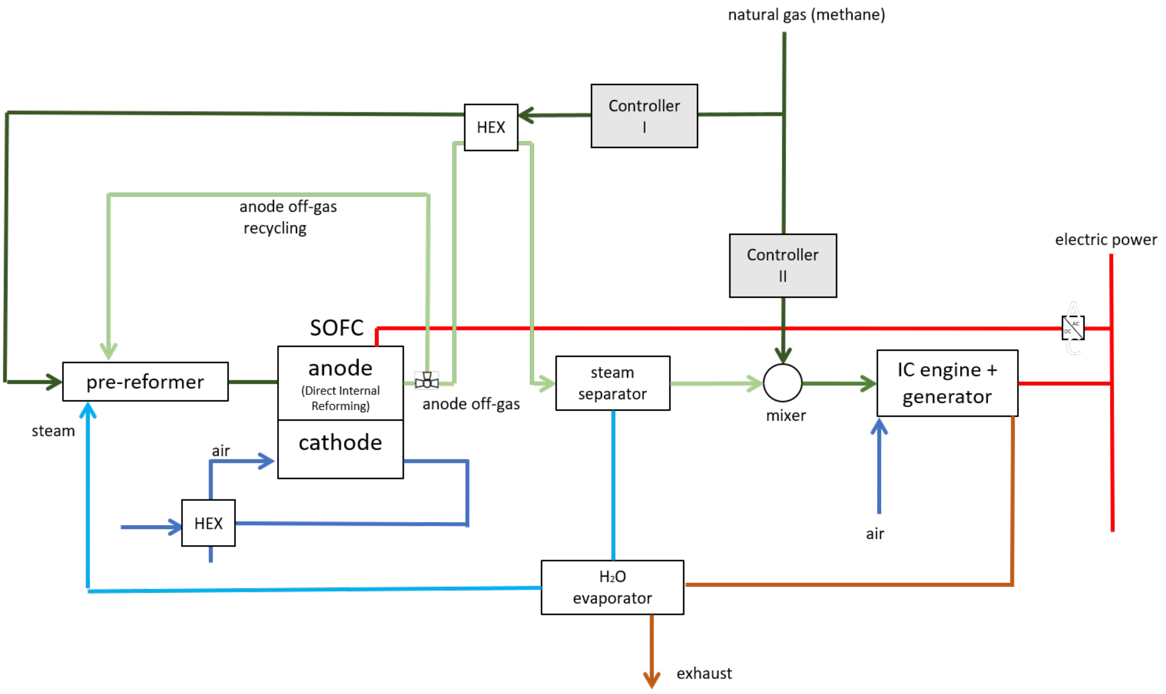

Figure 3.1: Diagram of proposed SOFC-ICE hybrid system.

3.1.3. ICE model

To determine the performance of the hybrid system, an ICE model is required to compute engine performance based on the fuel composition available at the engine intake. Also ICE exhaust-gas heat capacity has to be predicted for adequate heat integration of the engine in the hybrid system.

Developing an engine model which can operate on a variety of fuel blends is a complex operation. Hence, to keep engine modeling feasible within a thesis project, a mean value first principle model (MVFP) is developed which relies on experimental data for calibration. This work is considering a production ready reciprocating internal combustion engine technology. The selected engine to simulate is an eight cylinder, turbocharged, spark-ignited gas engine with a rated power of 500 kWe at 1500 rpm (Caterpillar-G3508). The experimental data set is considering three types of fuel blends at a fixed load of 375 kWe, 1500 rpm, $NO_x = 500\ \mathrm{mg/nm^3}$ (at 5% oxygen)[1]. Table 3.1 provides the fuel blends. Particularly, due to the dependency on this experimental data set, the engine model is considering hydrogen-natural gas blends. Effects of other anode off-gas species are not considered in this work. The engine model is explained in chapter 5.

Table 3.1: Tested hydrogen-natural gas fuel blends

Fuel blends	**Natural gas volume [%]**	**Hydrogen volume [%]**
NG	100	0
10HNG	90	10
20HNG	80	20

3.1.4. Heat integration

Heat integration is an important aspect for successful operation of an SOFC-ICE hybrid system. Recovery of residual heat from hot streams is done with heat exchangers and is supplied to cold streams. The hybrid system study is considering two designs of pre-reformer and SOFC heat integration. The proposed configurations are:

- Configuration A: the pre-reformer is part of the integrated stack module (ISM). The reaction heat required for the (endothermic) methane steam reforming reaction is withdrawn from the SOFC-stack.

---

[1] Accounting for the maritime emission regulations: IMO TIER-III limit $= 9 \cdot n^{-0.2}\ \mathrm{g\,kW^{-1}\,h^{-1}}$. For this engine n=1500 rpm, thus the NO_x limit is $2.08\ \mathrm{g\,kW^{-1}\,h^{-1}} \approx 500\ \mathrm{mg/nm^3}$ (at 5% oxygen), Marpol IV, Reg. 13 [50]

The pre-reformer operation temperature is the same as the SOFC inlet temperature. In literature, this configuration is called indirect internal reforming (IIR)

- Configuration B: the pre-reformer is an individual component, operating at 500 °C. The heat required for the (endothermic) methane steam pre-reforming reaction is withdrawn from residual heat in the hybrid system coming from steam separator and engine exhaust gas system. The heat integration of these components is an essential factor to increase hybrid system efficiency and is a novel concept.

A heat flow analysis (pinch analysis) is conducted to determine if the hybrid system contains enough heat to maintain all stream temperatures as required. Modeling and optimizing the heat exchanger network falls outside the scope of present work. The heat integration and pinch analysis are conducted in chapter 6.

3.2. Simulation strategy and analysis

To find the optimum performance of the SOFC-ICE hybrid system, an integration of component models is adopted for system simulations. The system simulations should provide insights of system behaviour depending on varying operating parameters.

At first, a power split ratio of 50%-ICE and 50%-SOFC is selected, because it is expected to be a good trade-off between: performance, power density, and dynamic capabilities. The ICE has a fixed power of 375 kWe (AC), hence the power output of the SOFC is also 375 kWe (AC) and the total power output of the hybrid system is 750 kWe (AC). A system study is focused around the effects of the following parameters:

- Effect of the SOFC current density on hybrid system efficiency will be investigated. A suitable current density is a compromise between efficiency, power density, capital costs, stable operation, and degradation risks [63].
- Effect of fuel utilization on hybrid system efficiency will be investigated using a conventional single-pass configuration (no anode off-gas recycling). Fuel utilization is not a standalone controllable parameter, it depends on fuel feed stream (controller I in figure 3.1) and the current drawn.
- Effect of methane pre-reforming ratio (REF) on hybrid system efficiency will be investigated. The best pre-reforming ratio is a compromise between efficiency and installation sizing.
- Effect of anode off gas recycling on hybrid system efficiency will be investigated. Both anode off-gas recycling ratio ($AOGRR$) and fuel utilization are the varying parameters.

Moreover, an analysis to stream composition and volumetric flow rate is done. An important condition to investigate is the hydrogen-natural gas percentage and diluted species percentage of the stream introduced in the engine, the engine model should indicate these operation limits. Then, the hybrid system is subjected to a pinch-analysis in order to investigate if heat integration is possible as proposed. Also effect of varying power split ratios is studied to investigate the performance gain while considering maximum hydrogen blend ratios at ICE intake. Finally, a comparison study is carried out to investigate the differences in performance, power and energy density between the SOFC-ICE hybrid system and conventional marine power plants. The hybrid system study and results are described in chapter 6.

4

SOFC model

A dynamic 0-D SOFC model including pre-reformer is developed in MATLAB Simulink. This chapter describes the development, validation and parameter sensitivity analysis. The model is developed in such a way that either the dynamic performance can be predicted or the steady state results can be used in the hybrid system study.

4.1. Model description

Figure 4.1 depicts a schematic representation of a multiple-cell SOFC stack. The SOFC stack model is composed of multiple single cell models. Each single cell model consists of four layers: fuel channel, PEN structure, air channel, and interconnect. For each layer conservation and constitutive equations are set up and solved. Figure 4.2 depicts the causal diagram of the modules forming the single cell model. The grey blocks indicate the modules where the physics are accommodated. The direction of the arrows represents the relation between input, output, and calculation modules.

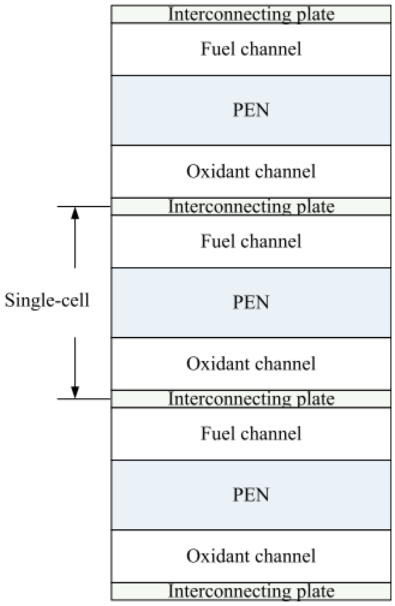

Figure 4.1: SOFC stack composed out of single cells. A single cell formed with 5 layers , picture taken from [33].

4.1.1. Model assumptions

The model is developed under the following assumptions:

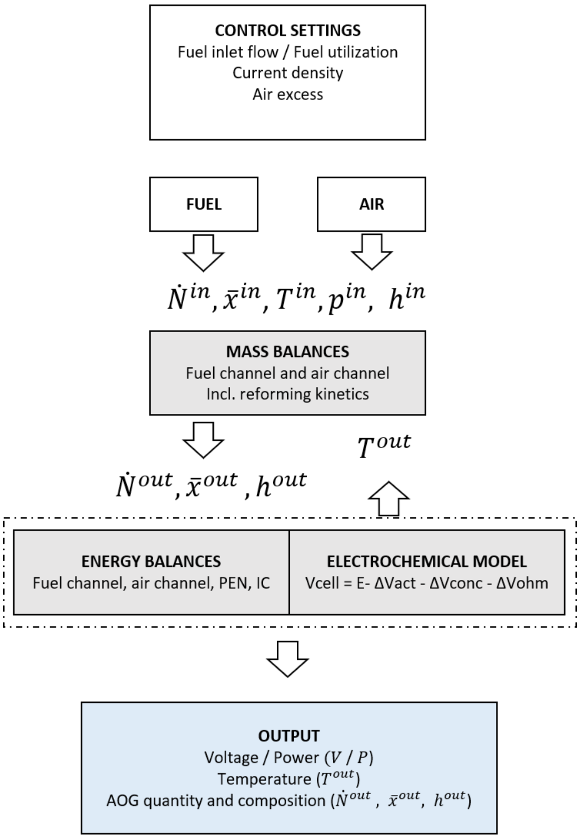

Figure 4.2: Schematic diagram of single cell model (0-D SOFC).

- Gas and air stream is considered as a laminar flow between parallel plates with fully developed hydrodynamics.

- All gases are assumed to be ideal gasses, since the SOFC operates at high temperature (around 1100 K) and moderate pressure (1 bar).

- Pressure difference along the fuel and air channel is assumed to be very small and therefore neglected. Accumulation of momentum is neglected.

- Temperature gradient across the PEN structure can be neglected, because the PEN structure is very thin (perpendicular to stream wise direction).

- CO is not directly oxidized but converted through the water-gas shift reaction [26].

- Cell voltage is calculated using Nernst equation and considering activation, concentration, and Ohmic losses as a function of cell current and temperature.

- Mass, thermal conductivity, and isobaric heat capacity of the gasses in the fuel and air channel are determined for inlet conditions and are taken as constant values throughout the channel. A study to the effects of this assumption is done afterwards and has justified this assumptions, see appendix D.

- The SOFC stack is packed in an insulated module. The maximum module outside surface temperature is allowed to be 50 °C. The assumed environmental temperature is 25 °C. It is assumed that the module insulation is designed to cope for these temperature specifications. The outside surfaces of the SOFC stack are undergoing convective and radiative heat loss to the environment. The final stack heat loss is proportionally included as a heat sink in the single cell energy balance.

- The fuel and air supply and stack exhausts are assumed to be adiabatic.

4.1.2. Model equations, single cell model

In this section the physical phenomena concerning SOFC operation are characterized by mathematical equations. The phenomena are schematically depicted in figure 4.3. The control volumes, indicated by red dashed lines, are used in below explanation. The relevant phenomena that are accounted for are:

- Mass and heat sources and sinks from the chemical reactions. The location of theses reactions is an approximate representation as implemented in the model.
- Energy accumulation in the gas flows, electrolyte and interconnects;
- Convective heat transfer between gas flows and solid elements;
- Radiative heat transfer between (anode/cathode) side of the PEN and interconnects.
- Hydrogen oxidation within the PEN structure, methane steam reforming reaction and water-gas shift reaction in the fuel channel. Table 4.1 provides the reactions.

Table 4.1: Reaction equations SOFC.

Id.	**Reaction name**	**Reaction equation**	**Location**
MSR	Methane steam reforming	$CH_4 + H_2O \longrightarrow CO + 3\,H_2$	Fuel channel
WGS	Water-gas shift	$CO + H_2O \longleftrightarrow CO_2 + H_2$	Fuel channel
-	Hydrogen oxidation	$H_2 + O^{2-} \longrightarrow H_2O + 2\,e^-$	Anode TPB
-	Oxygen reduction	$\frac{1}{2}O_2 + 2\,e^- \longrightarrow O^{2-}$	Cathode TPB
HOR	Hydrogen electrochemical oxidation	$H_2 + \frac{1}{2}O_2 \longrightarrow H_2O$	-

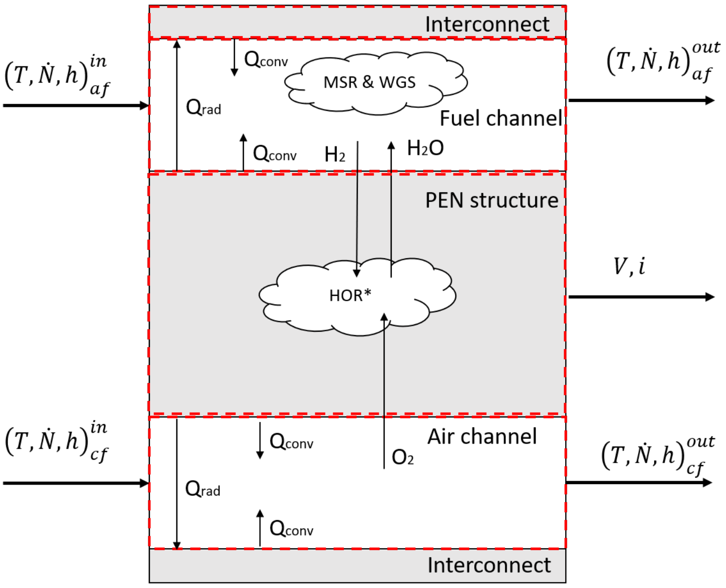

* It is assumed that the hydrogen oxidation reaction enthalpy is released at the PEN structure

Figure 4.3: Single cell composed out of control volumes which are indicated with red dashed lines. The MSR, WGS, and HOR 'clouds' are an approximate representation of the heat source location, as implemented in the model. Further included are: ingoing and outgoing molar flow rates with temperature and enthalpy, and modes of heat transfer between control volumes.

Mass balances

The single cell model consists of two mass balances. The fuel channel mass balance is considering the species: CH_4, H_2O, H_2, CO, and CO_2. The air channel mass balance is considering the species: O_2 and N_2.

Partially pre-reformed methane flows into the fuel channel (control volume) and undergoes steam reforming and water-gas shift reactions with the catalytic aid of the nickel component of the anode. Meanwhile hydrogen and water vapour diffuse across the channel surfaces (control volume). Mass balances for species in the fuel channel are in given in eq. 4.1 to 4.5.

$$\frac{dC_{CH_4}}{dt} = \frac{u_{af}}{L} \cdot \left(C_{CH_4}^{in} - C_{CH_4}^{out}\right) - \frac{1}{H_{af}} \cdot r_{MSR} \tag{4.1}$$

$$\frac{dC_{H_2O}}{dt} = \frac{u_{af}}{L} \cdot \left(C_{H_2O}^{in} - C_{H_2O}^{out}\right) + \frac{1}{H_{af}} \cdot r_{HOR} - \frac{1}{H_{af}} \cdot r_{MSR} - \frac{1}{H_{af}} \cdot r_{WGS} \tag{4.2}$$

$$\frac{dC_{H_2}}{dt} = \frac{u_{af}}{L} \cdot \left(C_{H_2}^{in} - C_{H_2}^{out}\right) - \frac{1}{H_{af}} \cdot r_{HOR} + 3 \cdot \frac{1}{H_{af}} \cdot r_{MSR} + \frac{1}{H_{af}} \cdot r_{WGS} \tag{4.3}$$

$$\frac{dC_{CO}}{dt} = \frac{u_{af}}{L} \cdot \left(C_{CO}^{in} - C_{CO}^{out}\right) + \frac{1}{H_{af}} \cdot r_{MSR} - \frac{1}{H_{af}} \cdot r_{WGS} \tag{4.4}$$

$$\frac{dC_{CO_2}}{dt} = \frac{u_{af}}{L} \cdot \left(C_{CO_2}^{in} - C_{CO_2}^{out}\right) + \frac{1}{H_{af}} \cdot r_{WGS} \tag{4.5}$$

C_i is the species concentration (mol m^{-3}), u the stream velocity (m s^{-1}), L the length of the channel (m), H the height of the channel (m), and r the area specific reaction rate (mol m^{-2} s^{-1}). The subscript af denotes the anode flow, thus through the fuel channel.

In the air channel some oxygen leaves the control volume, diffuses into the cathode (part of the PEN structure), and participates in the electrochemical reaction (HOR). No reaction product enters this control volume. Mass balances for O_2 and N_2 are given in eq. 4.6 and 4.7.

$$\frac{dC_{O_2}}{dt} = \frac{u_{cf}}{L} \cdot \left(C_{O_2}^{in} - C_{O_2}^{out}\right) - \frac{1}{2} \cdot \frac{1}{H_{cf}} \cdot r_{HOR} \tag{4.6}$$

$$\frac{dC_{N_2}}{dt} = \frac{u_{cf}}{L} \cdot \left(C_{N_2}^{in} - C_{N_2}^{out}\right) \tag{4.7}$$

The subscript cf denotes cathode flow, thus through the air channel. Equation 4.8, 4.9, and 4.10 are describing the area specific reactions rates r (mol m^{-2} s^{-1}).

$$r_{MSR} = k_{MSR} \cdot p_{CH_4} \cdot \left(1 - \frac{p_{CO} \cdot p_{H_2}^3}{p_{CH_4} \cdot p_{H_2O} \cdot K_{eq,MSR}}\right) \tag{4.8}$$

$$r_{WGS} = k_{WGS} \cdot p_{CO} \cdot \left(1 - \frac{p_{H_2} \cdot p_{CO2}}{p_{H_2O} \cdot p_{CO} \cdot K_{eq,WGS}}\right) \tag{4.9}$$

$$r_{HOR} = \frac{i}{2F} \tag{4.10}$$

In these expressions are the equilibrium constants ($K_{eq,MSR}$ and $K_{eq,WGS}$) are represented by eq. 4.11 and 4.12.

$$K_{eq,MSR} = exp\left(\frac{-\Delta G_{MSR}}{RT_{af}}\right) \tag{4.11}$$

$$K_{eq,WGS} = exp\left(\frac{-\Delta G_{WGS}}{RT_{af}}\right) \tag{4.12}$$

In this model chemical equilibrium was not achieved at the anode outlet when using the Achenbach MSR kinetics as discussed in the literature study. To achieve chemical equilibrium the equilibrium equation for methane steam reforming is applied (eq. 4.8), and hence the Achenbach MSR kinetics are not used in this model. Which is not required for a 0-Dimensional approach. In above equations the partial pressures p_i is expressed in (bar), both constants, k_{MSR} and k_{WGS}, are 1000 (mol s^{-1} m^{-2} bar^{-1}). ΔG_{MSR} and ΔG_{WGS} (J mol^{-1}) is the change in Gibbs free energy which implemented as a first order polynomial as derived in appendix B. The species concentration is determined with the ideal gas law (eq. 4.13 and 4.14).

$$C_{af}^{in} = \frac{p_{af}}{R \cdot T_{af}^{in}} \tag{4.13}$$

$$C_{cf}^{in} = \frac{p_{cf}}{R \cdot T_{cf}^{in}} \tag{4.14}$$

p_{af} is equal to the fuel inlet pressure and p_{cf} to the air inlet pressure (Pa). The stream velocity u in above equations is derived with eq. 4.15 and 4.16.

$$u_{af} = \frac{1}{A_{ch}} \frac{\dot{N}_{af}^{in} \cdot R \cdot T_{af}}{p_{af}^{in}} \tag{4.15}$$

$$u_{cf} = \frac{1}{A_{ch}} \frac{\dot{N}_{cf}^{in} \cdot R \cdot T_{cf}}{p_{cf}^{in}} \tag{4.16}$$

Where the ingoing molar flow rate $\dot{N}_{af}^{in}$ ($\mathrm{mol\,s^{-1}}$) is related to fuel utilization factor U_f (eq. 4.17) and $\dot{N}_{cf}^{in}$ is related to air excess ratio (eq. 4.18). The term in parenthesis in eq. 4.17 represents the total number of possible H_2 molecules that can be obtained from the inlet fuel.

$$U_f = \frac{i A_{act}}{2F\left(4x_{CH_4}^{in} + x_{H_2}^{in} + x_{CO}^{in}\right)\dot{N}_{af}^{in}} \tag{4.17}$$

$$\lambda_{air} = \frac{x_{O_2}^{in} \cdot \dot{N}_{cf}^{in}}{i \cdot A_{act}/4F} \tag{4.18}$$

The fuel channel molar outlet flow rates are calculated as follows:

$$\begin{gathered} \dot{N}_{af}^{in} \text{ is determined with eq.4.17} \\ \dot{m}_{af}^{in} = \dot{N}_{af}^{in} \cdot \sum_i x_i^{in} \cdot M_i \\ i \in (\mathrm{CH_4, H_2O, H_2, CO, CO_2}) \end{gathered} \tag{4.19}$$

$$\dot{m}_{O_2}^{in} = \frac{I}{4F} \cdot M_{O_2} \tag{4.20}$$

$$\dot{m}_{af}^{out} = \dot{m}_{af}^{in} + \dot{m}_{O_2}^{in} \tag{4.21}$$

$$\begin{gathered} \dot{N}_{af}^{out} = \frac{\dot{m}_{af}^{out}}{\sum_i x_i^{out} \cdot M_i} \\ i \in (\mathrm{CH_4, H_2O, H_2, CO, CO_2}) \end{gathered} \tag{4.22}$$

The air channel molar outlet flow rates are calculated as follows:

$$\begin{gathered} \dot{N}_{cf}^{in} \text{ is determined with eq.4.18} \\ \dot{m}_{cf}^{in} = \dot{N}_{cf}^{in} \cdot \sum_i x_i^{in} \cdot M_i \\ i \in (\mathrm{O_2, N_2}) \end{gathered} \tag{4.23}$$

$$\dot{m}_{O_2}^{out} = \frac{I}{4F} \cdot M_{O_2} \tag{4.24}$$

$$\dot{m}_{cf}^{out} = \dot{m}_{cf}^{in} - \dot{m}_{O_2}^{in} \tag{4.25}$$

$$\begin{gathered} \dot{N}_{cf}^{out} = \frac{\dot{m}_{cf}^{out}}{\sum_i x_i^{out} \cdot M_i} \\ i \in (\mathrm{O_2, N_2}) \end{gathered} \tag{4.26}$$

Where $\dot{m}$ is the mass flow ($\mathrm{kg\,s^{-1}}$), I the current (A), and F Faraday's constant ($\mathrm{C\,mol^{-1}}$).

Energy balances

Four energy balances are used (fuel channel, air channel, PEN structure and interconnect). The energy balances are written in terms of temperature dependent molar specific enthalpy.

The fuel gas temperature T_{af} is affected by several factors: reforming and water-gas shift reactions, internal energy carried by the incoming and outgoing flows, and convective heat transfer to the PEN structure and interconnect. Radiative heat transfer to the fuel flow is neglected since the gas mixtures behaves as a transparent media. The fuel channel energy balance is given in eq. 4.27.

$$\begin{aligned} \frac{N_{af} c_{p,af} dT_{af}}{dt} &= \sum_i \dot{N}_i^{in} h(T_{af})_i^{in} - \sum_i \dot{N}_i^{out} h(T_{af})_i^{out} - A_{act} \cdot r_{HOR} \cdot \left[h(T_{af})_{H2} - h(T_{PEN})_{H_2O} \right] + \ldots \\ &\quad \dot{Q}_{an-PEN}^{conv} + \dot{Q}_{an-ICa}^{conv} \\ &\quad i \in (\mathrm{CH_4}, \mathrm{H_2O}, \mathrm{H_2}, \mathrm{CO}, \mathrm{CO_2}) \end{aligned} \tag{4.27}$$

With:

$$\dot{Q}_{af-PEN}^{conv} = \alpha_{af} \cdot W \cdot L \cdot (T_{PEN} - T_{af}) \tag{4.28}$$

$$\dot{Q}_{af-ICa}^{conv} = \alpha_{af} \cdot W \cdot L \cdot (T_{ICa} - T_{af}) \tag{4.29}$$

The air temperature T_{cf} is affected by the ingoing and outgoing heat flows and convective heat transfer with the PEN structure and interconnect. Radiation to the air flow is neglected since air is transparent media. The air channel energy balance is given in eq. 4.30.

$$\begin{aligned} \frac{N_{cf} c_{p,cf} dT_{cf}}{dt} &= \sum_i \dot{N}_i^{in} h(T_{cf})_i^{in} - \sum_i \dot{N}_i^{out} h(T_{cf})_i^{out} - 0.5 \cdot A_{act} \cdot r_{HOR} \cdot h(T_{cf})_{O_2} + \ldots \\ &\quad \dot{Q}_{cf-PEN}^{conv} + \dot{Q}_{cf-ICc}^{conv} \\ &\quad i \in (\mathrm{O_2}, \mathrm{N_2}) \end{aligned} \tag{4.30}$$

With:

$$\dot{Q}_{cf-PEN}^{conv} = \alpha_{cf} \cdot W \cdot L \cdot (T_{PEN} - T_{cf}) \tag{4.31}$$

$$\dot{Q}_{cf-ICc}^{conv} = \alpha_{cf} \cdot W \cdot L \cdot (T_{ICc} - T_{cf}) \tag{4.32}$$

The first two terms on the right hand side in eq. 4.27 and 4.30 represent the energy in and out carried by the molar flow rate. The molar specific enthalpy h_i ($\mathrm{J\,mol^{-1}}$) of each species is approximated using first order polynomials of temperature as listed in appendix B. These first order polynomials are based on data which is computed with the ideal gas law thermodynamic model (Gasmix) in *FluidProp* [64]. c_p is the specific heat capacity at constant pressure ($\mathrm{J\,mol^{-1}\,K^{-1}}$), T temperature (K), $\dot{Q}^{conv}$ is the convective heat flow (W), α denotes the convective heat transfer coefficient ($\mathrm{W\,m^{-2}\,K^{-1}}$) and is calculated within the gas channel under the hypothesis that the flow regime is laminar and can be treated as flow through two infinite flat plates, $W \cdot L$ is the heat transfer area ($\mathrm{m^2}$). The subscripts af, cf, PEN, ICa, ICc denote: anode flow, cathode flow, PEN structure, interconnect anode side, and interconnect cathode side.

The endothermic methane steam reforming reaction takes place in the fuel channel. The heat absorption of this reaction is included in the enthalpy difference between inlet and outlet stream. Also the exothermic water-gas shift reaction takes place in the fuel channel. The heat supply of this reaction is also included in the enthalpy difference between inlet and outlet stream. Both are captured in first two terms right hand side eq. 4.27.

The PEN structure control volume encloses the anode, cathode, and electrolyte. Hydrogen and oxygen diffuses across control surfaces and enters the PEN structure. The reaction product, water, diffuses out of this control volume to the fuel channel. Through electrochemical reactions, part of the chemical energy converts to electrical power (output), while the other part is converted to heat and released to the surroundings of the control volume by radiation and convection. The energy balance is expressed in eq. 4.33.

$$\begin{aligned} m_{PEN} c_{PEN} \frac{dT_{PEN}}{dt} &= A_{act} \cdot r_{HOR} \cdot \left[\ h(T_{af})_{H2} + 0.5 h(T_{cf})_{O_2} - h(T_{PEN})_{H_2O}\ \right] - V_{cell} i_{cell} A_{act} - \ldots \\ &\quad \dot{Q}_{ICa-PEN}^{rad} - \dot{Q}_{ICc-PEN}^{rad} - \dot{Q}_{cf-PEN}^{conv} - \dot{Q}_{af-PEN}^{conv} \end{aligned} \tag{4.33}$$

With:

$$\dot{Q}^{rad}_{ICa-PEN} = \frac{\sigma \cdot \epsilon_{ICa} \cdot \epsilon_{PEN} \cdot W \cdot L \cdot (T^4_{ICa} - T^4_{PEN})}{\epsilon_{ICa} + \epsilon_{PEN} - \epsilon_{ICa} \cdot \epsilon_{PEN}} \tag{4.34}$$

$$\dot{Q}^{rad}_{ICc-PEN} = \frac{\sigma \cdot \epsilon_{ICc} \cdot \epsilon_{PEN} \cdot W \cdot L \cdot (T^4_{ICc} - T^4_{PEN})}{\epsilon_{ICc} + \epsilon_{PEN} - \epsilon_{ICc} \cdot \epsilon_{PEN}} \tag{4.35}$$

Where m is the mass of the triple layered PEN structure (kg), c the specific heat capacity of PEN materials excluding gasses ($\mathrm{J\,kg^{-1}\,K^{-1}}$). $\dot{Q}^{rad}$ denotes the radiative heat flow for two gray body surfaces forming an enclosure (W), in this case the view factor is 1, σ is the Stefan Boltzmann constant ($\mathrm{W/(m^2 \cdot K^4)}$), and ϵ is the surface emissivity (-).

The electrochemical reaction of hydrogen oxidation takes place in the PEN structure, where hydrogen and oxygen migrate from the fuel and air channel. The water produced by the oxidation reaction diffuses back to the fuel channel. Therefore, the enthalpy fluxes associated with the flow of oxygen and hydrogen to the PEN structure and the flow of water from the PEN structure are taken into account in the PEN energy balance (first term right hand side eq. 4.33). The third term on the right hand side of eq. 4.27 and 4.30 refers to the respective enthalpy fluxes to and from the fuel and air channel.

The interconnecting plates divide one cell from the adjacent ones and separate the fuel channel and the air channel. No chemical reactions and mass transfer takes place within these plates, only heat exchanges to the surroundings by radiation and convection. The energy balance of the interconnect is given by eq. 4.36.

$$m_{IC} c_{IC} \frac{dT_{IC}}{dt} = \dot{Q}^{rad}_{ICa-PEN} + \dot{Q}^{rad}_{ICc-PEN} - \dot{Q}^{conv}_{af-ICa} - \dot{Q}^{conv}_{cf-ICc} \tag{4.36}$$

The convective heat flow from the PEN structure and interconnects to the fuel and air stream depends on the convective heat transfer coefficient α ($\mathrm{W\,m^{-2}\,K^{-1}}$). α is calculated by empirical correlations using the dimensionless Nusselt number Nu (eq. 4.41). The Nussselt number is computed with the Reynolds number Re and Prandtl number Pr of the bulk flow (eq. 4.37). Mills [65] provides eq. 4.37 to calculate the Nusselt number. Using the assumption that the flow is considered as a laminar flow between parallel plates with fully developed hydrodynamics. The dynamic viscosity μ, thermal conductivity k, and isobaric heat capacity c_p of each gas component is calculated in appendix B. Also, appendix B describes the method to obtain these properties for a multi-component gas mixture.

$$Nu = 7.54 + \frac{0.03(D_h/L)Re_{D_h}Pr}{1 + 0.016[(D_h/L)Re_{D_h}Pr]^{2/3}} \tag{4.37}$$

$$D_h = \frac{4A_{ch}}{P_{ch}} \tag{4.38}$$

$$Pr = \frac{\mu c_p}{k} \tag{4.39}$$

$$Re_{D_h} = \frac{\rho u D_h}{\mu} \tag{4.40}$$

$$\alpha = Nu \frac{k}{D_h} \tag{4.41}$$

Electrochemical model

The voltage of an operating cell is generally given by eq. 4.42.

$$V_{cell} = E - \Delta V_{act} - \Delta V_{conc} - \Delta V_{ohm} \tag{4.42}$$

The open circuit voltage E (V) is calculated with eq. 4.43. Where E^0 stands for the open-circuit voltage at standard pressure (V). E^0 (eq. 4.44) is calculated using the temperature dependent Gibbs free energy of hydrogen oxidation ΔG_{HOR}. Eq. 4.45 (derived in appendix B).

$$E = E^0 + \frac{RT_{PEN}}{nF} ln\left(\frac{p_{H_2} \cdot p_{O_2}^{0.5}}{p_{H2O}}\right) \tag{4.43}$$

$$E_0 = \frac{-\Delta G_{HOR}}{nF} \tag{4.44}$$

$$\Delta G_{HOR} = (-54.6 \cdot T_{PEN} + 2.478 \cdot 10^5) \tag{4.45}$$

The activation losses ΔV_{act} are depending on the exchange current density i_0 ($\mathrm{A\,m^{-2}}$) (eq. 4.47 and 4.48). k_a and k_c are pre-exponential coefficients ($\Omega^{-1}\,\mathrm{m}^{-2}$), and $E_{a,a}$ and $E_{a,c}$ is the activation energy for the anode and cathode ($\mathrm{J\,mol^{-1}}$), these values are obtained from literature [26] and provided in table 4.4. T is the temperature (K) and is directly obtained from the energy balance.

$$\Delta V_{act} = \frac{RT_{PEN}}{F}\sinh^{-1}\left(\frac{i}{2i_{0,a}}\right) + \frac{RT_{PEN}}{F}\sinh^{-1}\left(\frac{i}{2i_{0,c}}\right) \tag{4.46}$$

$$i_{0,a} = \frac{RT_{PEN}}{2F} \cdot k_a \cdot exp\left(\frac{-E_{a,a}}{RT_{PEN}}\right) \tag{4.47}$$

$$i_{0,c} = \frac{RT_{PEN}}{2F} \cdot k_c \cdot exp\left(\frac{-E_{a,c}}{RT_{PEN}}\right) \tag{4.48}$$

To calculate concentration losses ΔV_{conc} a relation between the partial pressures p of H_2, H_2O, and O_2 at the triple phase boundaries and the current density is necessary. It is assumed H_2 and H_2O from the anode are diffusing (one-dimensional) through the pores to the PEN structure, and only o_2 from the cathode diffuses to the PEN structure. The local partial pressures are therefore given by eq. 4.50-4.51 [66].

$$\Delta V_{conc} = \frac{RT_{PEN}}{2F}\ln\left(\frac{p_{H_2O,TPB} \cdot p_{H2,af}}{p_{H2O,af} \cdot p_{H_2,TPB}}\right) + \frac{RT_{PEN}}{4F}\ln\left(\frac{p_{O_2,cf}}{p_{O_2,TPB}}\right) \tag{4.49}$$

$$p_{H_2,TPB} = p_{H_2,af} - \frac{RT_{PEN}\tau_{anode}}{2FD_{eff,anode}} i \tag{4.50}$$

$$p_{H_2O,TPB} = p_{H_2O,af} - \frac{RT_{PEN}\tau_{anode}}{2FD_{eff,anode}} i \tag{4.51}$$

$$p_{O_2,TPB} = p_{cf} - (p_{cf} - p_{O_2,cf}) - exp\left(\frac{RT_{PEN}\tau_{cathode}}{4FD_{eff,cathode}p_{cf}} i\right) \tag{4.52}$$

$$D_{eff,i} = \frac{material\ porosity}{tortuosity\ factor} \cdot D_{molecular,i} \qquad i \in (H_2, H_2O, O_2) \tag{4.53}$$

In this model, D_{eff} is the average effective diffusivity coefficient ($\mathrm{m^2\,s^{-1}}$) and is related to the molecular diffusivity $D_{molecular}$. In this model D_{eff} is taken from literature [26] and is provided in table 4.3. In case the material porosity and tortuosity of the SOFC are known, D_{eff} can also be calculated with eq. 4.53.

The ohmic losses ΔV_{ohm} are implemented as described in the literature review. Eq. 4.54 and 4.55 express the used equations.

$$\Delta V_{ohm} = i \cdot r_{ohm} \tag{4.54}$$

$$r_{ohm} = \frac{\tau_{ae}}{\sigma_{ae}} + \frac{\tau_{ce}}{\sigma_{ce}} + \frac{\tau_{se}}{\sigma_{se}} \tag{4.55}$$

Performance indication

Performance parameters usually adopted in fuel cell research are power density and first law efficiency. The power density (eq. 4.56) is the amount of power per unit area ($\mathrm{W\,m^{-2}}$). The first law efficiency (eq. 4.57) represents the fraction of the total chemical energy in the inlet fuel that is converted into electrical energy.

$$Pd_{cell} = i \cdot V_{cell} \tag{4.56}$$

$$\eta_{SOFC,LHV} = \frac{i \cdot V_{cell} \cdot A_{act}}{\left(x^{in}_{CH_4} \cdot LHV_{CH_4} + x^{in}_{H_2} \cdot LHV_{H_2} + x^{in}_{CO} \cdot LHV_{CO}\right) \dot{N}^{in}_{af}} \tag{4.57}$$

Where the lower heating values (LHV) are LHV_{CH_4} is $802.6 \cdot 10^3\ \mathrm{J\,mol^{-1}}$, $LHV_{CO} = 283.0 \cdot 10^3\ \mathrm{J\,mol^{-1}}$, and $LHV_{H_2} = 241.8 \cdot 10^3\ \mathrm{J\,mol^{-1}}$ [67].

4.1.3. SOFC stack design

The total SOFC stack power is determined by multiplying single cell power with the total number of stacked cells (eq. 4.58).

$$P_{stack} = (\text{number of cells}) \cdot V_{cell} \cdot I_{cell} \tag{4.58}$$

The single cell model is used to predict operating conditions for the whole stack. For the single single cell model, adiabatic boundary conditions are assumed. This physically means that the cell is positioned in the middle of the stack. When conducting simulations of the complete stack, the outside boundaries cannot be assumed adiabatic any more, as the temperature difference between stack surface and environment is large. This means that heat loss to the environment becomes important for thermal management of the SOFC stack. Achenbach [68] studied the effects of stack heat loss on the temperature distribution in the stack and concluded that an effective thermal insulation is necessary to protect the stack from cooling out. Stack heat loss is denoted by $Q_{stack\ heat\ loss}$ (W).

In this work a constant stack module outside surface temperature of 50 °C is assumed. The module is loosing heat by convective and radiative heat transfer to the environment. When running stack simulations the total stack heat loss is proportionally included as a heat sink in the single cell energy balance. The stack heat loss is determined with eq. 4.59. For this calculation is an effective thermal insulation layer assumed which avoids exceeding the maximum surface temperature. The situation is schematically depicted in figure 4.4. The SOFC stack model outside surface area is a rough estimation and is assumed to be similar to the energy server ’5’ of Bloomenergy (300 kW) [69]. The present stack dimensions are determined to be: 5.5 x 2.5 x 2 m, which is including pre-reformer, heat exchangers, and pipe work.

$$Q_{stack\ heat\ loss} = Q_{stack\ rad\ in} - Q_{stack\ rad\ out} - Q_{stack\ conv} \tag{4.59}$$

Where:

$$Q_{stack\ rad\ in} = \alpha \cdot \sigma \cdot A \cdot (T^4_{surface} - T^4_{environment}) \tag{4.60}$$

$$Q_{stack\ rad\ out} = \epsilon \cdot \sigma \cdot A \cdot (T^4_{surface} - T^4_{environment}) \tag{4.61}$$

$$Q_{stack\ conv} = h_c \cdot A \cdot (T_{surface} - T_{environment}) \tag{4.62}$$

Where $\alpha = 0.85$ is the absorption coefficient of the module, $\epsilon = 0.9$ the surface emissivity of the module, A is the module outside area (59.5 $\mathrm{m^2}$), $h_c = 25\ \mathrm{W\,m^{-2}\,K^{-1}}$ the convective heat transfer coefficient. α, ϵ, and h_c are assumed values for commonly used isolation material.

4.1.4. SOFC properties

Table 4.2, 4.3 and 4.4 present the SOFC geometry and material property data. This data is typical for planar, anode supported, intermediate temperature SOFCs [26].

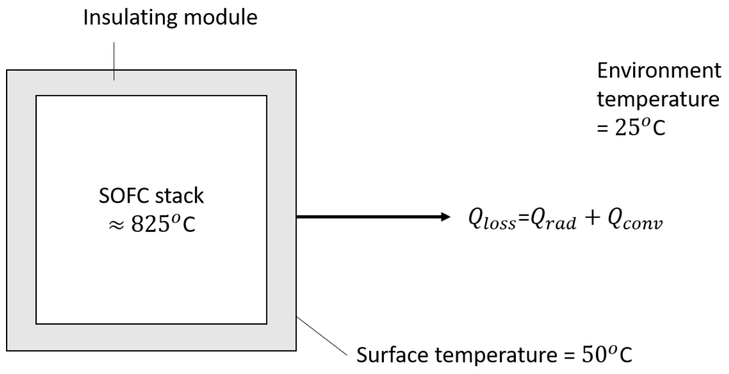

Figure 4.4: SOFC stack in insulated module.

Table 4.2: Geometrical properties single cell SOFC.

Geometrical properties	**Symbol**	**Value**	**Unit**
Cell width (active)$^{(1)}$	W	0.1	m
Cell length (active)	L	0.4	m
Channel height (air and fuel)	h	$1\cdot10^{-3}$	m
Anode thickness	τ_a	$500\cdot10^{-6}$	m
Cathode thickness	τ_c	$50\cdot10^{-6}$	m
Electrolyte thickness	τ_e	$20\cdot10^{-6}$	m
Interconnect thickness	τ_{ic}	$500\cdot10^{-6}$	m

(1) The cell length multiplied by cell width represents the active cell area.

Table 4.3: Physical properties single cell SOFC.

Physical properties	**Symbol**	**Value**	**Unit**
Specific heat PEN structure	c_{PEN}	500	$\mathrm{J\,kg^{-1}\,K^{-1}}$
Specific heat interconnect	c_{ic}	500	$\mathrm{J\,kg^{-1}\,K^{-1}}$
Density PEN structure	ρ_{PEN}	5900	$\mathrm{kg\,m^{-3}}$
Density interconnect	ρ_{ic}	8000	$\mathrm{kg\,m^{-3}}$
Electronic conductivity anode $^{(1)}$	σ_{ae}	$8.0\cdot10^{4}$	$\Omega^{-1}\,\mathrm{m^{-1}}$
Electronic conductivity cathode $^{(1)}$	σ_{ce}	$8.4\cdot10^{3}$	$\Omega^{-1}\,\mathrm{m^{-1}}$
Electronic conductivity electrolyte	σ_{ee}	$33400exp(-10300/T_{PEN})$	$\Omega^{-1}\,\mathrm{m^{-1}}$
Emmisivity PEN$^{(2)}$	ϵ_{PEN}	0.8	–
Emmisivity interconnect$^{(2)}$	ϵ_{ic}	0.1	–
Diffusivity effective anode	$D_{eff,a}$	$3.66\cdot10^{-5}$	$\mathrm{m^2\,s^{-1}}$
Diffusivity effective cathode	$D_{eff,a}$	$1.37\cdot10^{-5}$	$\mathrm{m^2\,s^{-1}}$
Electrode porosity	ϵ_p	0.3	–
Electrode tortuosity	$\tau_{tortuosity}$	6	–
Average pore radius	$\bar{r}_{pore}$	$0.5\cdot10^{-6}$	m

(1) The temperature dependence of the anode and cathode electronic conductivity is considered to be negligible for the temperature range in which this model operates [26, 70].
(2) The PEN and interconnect emissivity values are considered typical of ceramic and stainless steel materials [26, 70].

Table 4.4: Reaction and electrode properties single cell SOFC.

Reactions	**Symbol**	**Value**	**Unit**
MSR equilibrium reaction constant	k_{MSR}	1000	$\mathrm{mol\,s^{-1}\,m^{-2}\,bar^{-1}}$
WGS reaction constant	k_{WGS}	1000	$\mathrm{mol\,s^{-1}\,m^{-2}\,bar^{-1}}$
Activation Energy MSR	E_a	$82 \cdot 10^3$	$\mathrm{J\,mol^{-1}}$
Electrode properties	**Symbol**	**Value**	**Unit**
Pre-exponential coefficient anode	k_a	$6.54 \cdot 10^{11}$	$\Omega^{-1}\,\mathrm{m^{-2}}$
Pre-exponential coefficient cathode	k_a	$2.35 \cdot 10^{11}$	$\Omega^{-1}\,\mathrm{m^{-2}}$
Activation Energy anode	E_{aa}	$140 \cdot 10^3$	$\mathrm{J\,mol^{-1}}$
Activation Energy cathode	E_{aa}	$137 \cdot 10^3$	$\mathrm{J\,mol^{-1}}$

4.2. Pre-reformer model

A pre-reformer model is developed to partially pre-reform the methane feed stream before it enters the SOFC model. The model is able to predict pre-reformer outlet properties which then become SOFC inlet properties.

4.2.1. Model description

A pre-reforming reactor is installed upstream the SOFC anode inlet in order to reduce the risk of carbon depositing in SOFC's anode channels and to limit large temperature gradients in the SOFC stack, caused by strong cooling effect of the fast reforming reactions at the inlet of the fuel channel [27].

The composition at the pre-reformer outlet depends on the following parameters: chemical species composition at the pre-reformer inlet[1], methane pre-reformer conversion factor REF, required oxygen-over-carbon ratio O/C, and operating temperature and pressure. In this model the pressure is assumed to be atmospheric. The operating temperature is equal to the SOFC inlet temperature for configuration A, and is set to be 500 °C for configuration B. A pre-reformer temperature of 500 °C is found as a common practice in literature [5]. The methane pre-reformer conversion factor is defined as in eq. 4.64.

Inside the pre-reformer the methane steam reforming (MSR) and water-gas shift (WGS) reactions take place (table 2.1). In order to maintain the MSR reaction, steam has to be fed to the system. The steam is supplied by either the external steam supply or as compound in the AOG recycling stream. The external steam supply is controlled to maintain a required oxygen to carbon ratio at the pre-reformer inlet composition. Usually a steam to carbon ratio $S/C > 2$ is the control parameter for the reformer in order to prevent carbon depositing [9]. However when considering AOG-recirculation, oxygen to carbon ratio is a more suitable indicator, as anode off-gas contains large amounts of carbon dioxide as well (eq. 4.63) [13]. No carbon depositing is expected for $O/C > 2$. In present pre-reformer model a PI controller controls the steam supply to the reformer based on the O/C requirement greater than 2. When AOG recirculation is applied the external steam supply is automatically decreased to zero if sufficient steam is supplied by the AOG recirculation flow. Figure 4.5 depicts the system boundaries, the feed streams, and the outlet streams.

$$O/C = \frac{\dot{N}_{H_2O} + \dot{N}_{CO} + 2\dot{N}_{CO_2}}{\dot{N}_{CH_4} + \dot{N}_{CO} + \dot{N}_{CO_2}} \tag{4.63}$$

$$REF = 1 - \frac{\dot{N}_{CH_4}^{pre,out}}{\dot{N}_{CH_4}^{pre,in}} \tag{4.64}$$

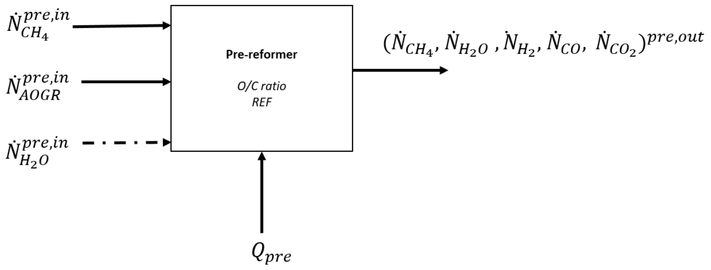

Figure 4.5: Pre-reformer model system borders.

Pre-reformer model assumptions

The following assumptions are made:

- The operating pressure is atmospheric. Pressure losses are neglected within the reformer.
- All gases are assumed to obey the ideal gas law.
- The pre-reformed methane is reformed in CO and H_2 by stoichiometric ratios.
- In this model REF is an artificial control mechanism to set the CH_4-ratio to be pre-reformed.

---

[1] Methane, or a composition of methane and AOG-Recycling stream

- The WGS reaction is in equilibrium. The WGS reaction equilibrium constant ($K_{eq,WGS}$) depends on the change of Gibbs free energy as shown in eq. 4.12. The change of Gibbs free energy is determined using fit functions as described in appendix B. The used fit function is also constructed for atmospheric pressure.

Pre-reformer model equations

The following mole balances hold for the elements: carbon (eq. 4.65), hydrogen (eq. 4.66), and oxygen (eq. 4.67):

$$0 = \dot{N}_{CH_4}^{pre,out} + \dot{N}_{CO}^{pre,out} + \dot{N}_{CO_2}^{pre,out} - \dot{N}_{CH_4}^{pre,in} - \dot{N}_{CO}^{pre,in} - \dot{N}_{CO_2}^{pre,in} \tag{4.65}$$

$$0 = 4\dot{N}_{CH_4}^{pre,out} + 2\dot{N}_{H_2}^{pre,out} + 2\dot{N}_{H_2O}^{pre,out} - 4\dot{N}_{CH_4}^{pre,in} - 2\dot{N}_{H_2O}^{pre,in} - 2\dot{N}_{H_2}^{pre,in} \tag{4.66}$$

$$0 = \dot{N}_{H_2O}^{pre,out} + \dot{N}_{CO}^{pre,out} + 2\dot{N}_{CO_2}^{pre,out} - \dot{N}_{H_2O}^{pre,in} - \dot{N}_{CO}^{pre,in} - 2\dot{N}_{CO_2}^{pre,in} \tag{4.67}$$

In order to calculate the five unknowns (outlet molar flow): $\dot{N}_{H2}^{pre,out}$, $\dot{N}_{H_2O}^{pre,out}$, $\dot{N}_{CH4}^{pre,out}$, $\dot{N}_{CO}^{pre,out}$, and $\dot{N}_{CO2}^{pre,out}$ as a function of reformer conversion factor (eq. 4.64) a fifth equation is added, which is directly derived from the WGS equilibrium equation (eq. 4.68). The set of 5 equations (eq. 4.64 - 4.68) is solved in MATLAB for each time step.

$$K_{eq,WGS}(p,T) = \frac{\dot{N}_{H_2}^{pre,out} \cdot \dot{N}_{CO_2}^{pre,out}}{\dot{N}_{H_2O}^{pre,out} \cdot \dot{N}_{CO}^{pre,out}} \tag{4.68}$$

The net reaction heat required to maintain the reaction is calculated as follows:

$$\begin{aligned} Q_{pre} &= \sum_i \dot{N}_i^{pre,in} \cdot h(T_{pre})_i - \sum_i \dot{N}_i^{pre,out} \cdot h(T_{pre})_i \\ i &\in (\mathrm{CH_4}, \mathrm{H_2O}, \mathrm{H_2}, \mathrm{CO}, \mathrm{CO_2}) \end{aligned} \tag{4.69}$$

Depending on the chosen configuration (A or B) this heat is included as a heat sink in the single cell energy balance (configuration A) or provided by residual heat available due to system heat integration (configuration B).

4.3. Anode off-gas recycling

If anode off-gas recycling is applied, a part of the SOFC anode off-gas is directed backwards to the pre-reformer inlet. The molar flow rate of this stream depends $\dot{N}_{AOGR}$ on the anode-off gas recycling ratio ($AOGRR$) and is calculated with eq. 4.70. The composition of this stream is equal to the SOFC anode outlet composition. The pre-reformer inlet flow rates are now computed with eq. 4.71 to 4.75.

$$\dot{N}_{AOGR} = AOGRR \cdot \dot{N}_{af}^{out} \tag{4.70}$$

$$\dot{N}_{CH_4}^{pre,in} = \dot{N}_{AOGR} \cdot x_{CH4}^{af,out} + \dot{N}_{CH4}^{feed} \tag{4.71}$$

$$\dot{N}_{H_2O}^{pre,in} = \dot{N}_{AOGR} \cdot x_{H_2O}^{af,out} + \dot{N}_{H_2O}^{steam} \tag{4.72}$$

$$\dot{N}_{H_2}^{pre,in} = \dot{N}_{AOGR} \cdot x_{H_2}^{af,out} \tag{4.73}$$

$$\dot{N}_{CO}^{pre,in} = \dot{N}_{AOGR} \cdot x_{CO}^{af,out} \tag{4.74}$$

$$\dot{N}_{CO_2}^{pre,in} = \dot{N}_{AOGR} \cdot x_{CO_2}^{af,out} \tag{4.75}$$

4.4. SOFC model validation

In this section the SOFC model is validated with results from literature. To have a benchmark conditions for validation, a set of initial conditions is determined (table 4.5). The provided fuel composition is considered as a gas mixture of CH_4, H_2O, H_2, CO, and CO_2 and results from a pre-reforming reaction with a oxygen to carbon ratio of 2, 10 % CH_4 pre-reforming, no AOG-recycling, and where the water-gas shift reaction is at equilibrium.

Based on an operating voltage of around 0.7 V, the operating current density is initially set at 5000 $\mathrm{A\,m^{-2}}$. Aguiar et al. [26] demonstrated that this range of operation is a good compromise between cell efficiency, power density, low capital costs, and stable operation. The species thermodynamic properties are implemented as explained in appendix B.

Table 4.5: Input parameters single cell model.

Input parameter	**Symbol**	**Value**	**Unit**
Air inlet temperature	T_{air}	1023	K
Fuel inlet temperature	T_{af}	1023	K
Air inlet pressure	p_{cf}	$1 \cdot 10^5$	Pa
Fuel inlet pressure	p_{af}	$1 \cdot 10^5$	Pa
Operating condition	**Symbol**	**Value**	**Unit**
Current density	i	5000	$\mathrm{A\,m^{-2}}$
Air excess	λ_{air}	8.5	-
Fuel utilization	U_f	0.75	-
Fuel inlet composition	**Symbol**	**Value**	**Unit**
Mole fraction CH_4	$x_{CH_4}^{in}$	0.282	-
Mole fraction H_2O	$x_{H_2O}^{in}$	0.566	-
Mole fraction H_2	$x_{H_2}^{in}$	0.121	-
Mole fraction CO	x_{CO}^{in}	0.004	-
Mole fraction CO_2	$x_{CO_2}^{in}$	0.027	-
Air inlet composition	**Symbol**	**Value**	**Unit**
Mole fraction O_2	$x_{O_2}^{in}$	0.210	-
Mole fraction N_2	$x_{N_2}^{in}$	0.790	-

4.4.1. Model verification

It is verified that mass, element and energy is conserved in the model. Also the chemical composition at the model output is verified with a computed chemical equilibrium from *Factsage*. Appendix C describes these verification analysis in detail.

4.4.2. Model validation

The steady state and dynamic performance of developed model is compared with results from literature. Although several publications about dynamic modeling of SOFCs are found, complete sets of measured (time-dependent) data and parameters suitable for validation of present model are not found. The 1-D SOFC model developed by Aguiar et al.[26] is used as benchmark for validation in this work. While Aguiars work is not validated either, this reference is selected because it described accurately the model properties, model development, and results. Moreover it is a widely accepted publication in this research field. Reference [26] presents the model design and its steady state performance, reference [71] is a related publication and presents the model's dynamic performance.

Electrochemical model

At first, the electrochemical model is validated. The characteristic curves for cell voltage and power density as a function of current density are constructed using an undepleted fully reformed fuel mixture[2] and constant operating temperature. These curves are the results of the electrochemical model only and are not influenced by other parts of the model which makes them suitable for an electrochemical-model comparison with literature.

Figure 4.6 and 4.7 depict the results. Figure 4.6 presents the individual contributions of all the various potential losses at a operating temperature of 1073 K. Figure 4.7 presents cell voltage and power density for 923, 1023, 1073 K. The marked lines in these figures depict the data from ref. [26]. As can be seen in the figure, at lower current densities the electrochemistry-model concurs with the reference model. A deviation arises at higher current densities. Mainly caused by a deviation in anode-activation voltage loss becoming significant at current density greater than 10000 $\mathrm{A\,m^{-2}}$.

---

[2] Although current is drawn, the fuel composition in the fuel channel stays constant: x_{H2O}=0.16, x_{H2}=0.64, and x_{O2}=0.21 (= undepeleted).

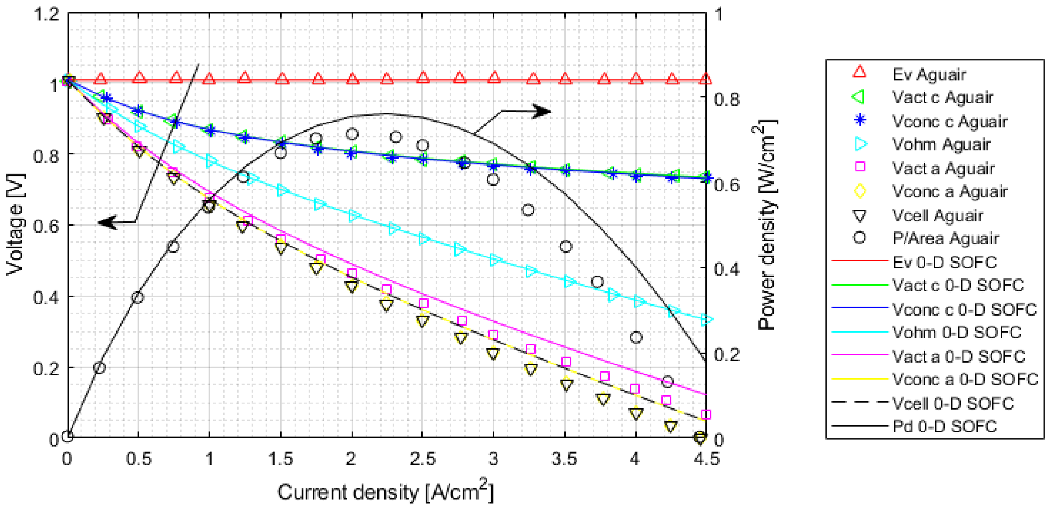

Figure 4.6: Cell voltage and power density as a function of current density at 1073 K for an undepleted fully reformed fuel mixture.

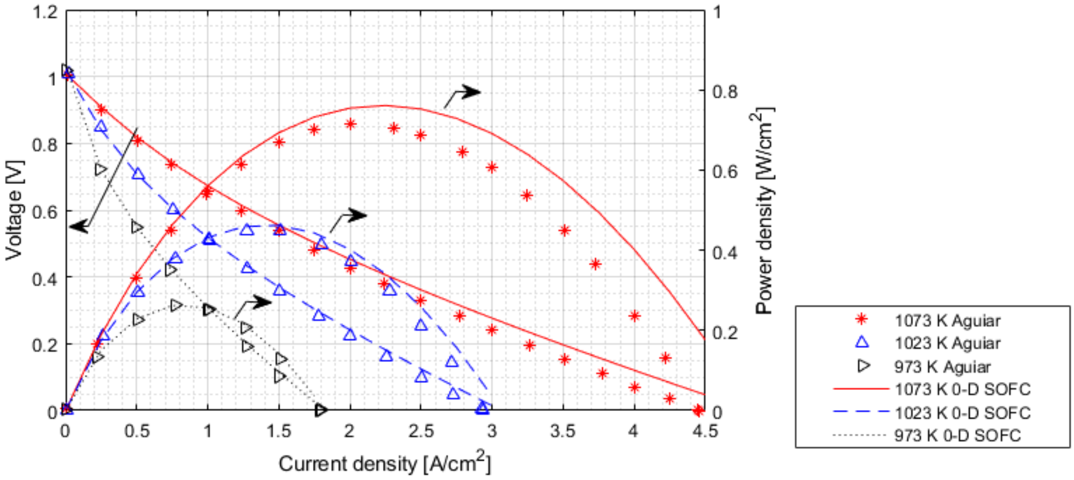

Figure 4.7: Cell voltage and power density as a function of current density at 973, 1023, 1073 K for an undepleted fully reformed fuel mixture.

Steady state validation

Table 4.6 provides steady-state results from the single cell SOFC model compared with the 1-D model of Aguiar [26]. The input data is provided in table 4.5.

The here-developed SOFC model predicts 8 % higher cell performance and 2 to 3 % lower temperatures compared to the reference model. It appears that these deviations are due to the different modeling approach, lumped modeling versus distributed parameter modeling. The 1-D SOFC model developed by Aguiar et al. predicts minimum and maximum current density and distributed temperature information as illustrated in figure 4.8 and 4.9. As shown in figure 4.9 the maximum current density is 9362 $\mathrm{A\,m^{-2}}$ in the reference paper. Generally, a higher local current density results in a lower voltage. The peak current density is dominant for predicting final cell voltage. As an example, when operating the electrochemical model of here-developed SOFC model at 9362 $\mathrm{A\,m^{-2}}$, the final results are comparable with the reference results (table 4.5).

Summarizing: the distributed-parameter model is more accurate in predicting final cell voltage compared to 0-D models. While higher order models are in theory more accurate, this is at the expense of computation time (it approximately takes 40 times longer to reach steady state conditions [33]). In this work these performance deviations are accepted, future work should investigate the possibilities to calibrate 0-D models with experimental data or accurate higher order models.

Table 4.6: Validation of single cell model (5000 $\mathrm{A\,m^{-2}}$ and 9362 $\mathrm{A\,m^{-2}}$). Steady state simulation results are compared with data from ref. [26] operating at an average current density of 5000 $\mathrm{A\,m^{-2}}$. For other input parameters see table 4.5.

Parameter	**Aguiar et al. avg. i = 5000** $\mathrm{A\,m^{-2}}$	**0-D SOFC i = 5000** $\mathrm{A\,m^{-2}}$	**Deviation [%]**	**0-D SOFC i = 9362** $\mathrm{A\,m^{-2}}$	**Deviation [%]**
V_{cell} [V]	0.663	0.716	8.0	0.658	0.7
P_{el} [W]	132.6	143.1	8.0	131.5	0.7
i_{min} [$\mathrm{Am^{-2}}$]	2500	-	-	-	-
i_{max} [$\mathrm{Am^{-2}}$]	9362	-	-	-	-
i_{avg} [$\mathrm{Am^{-2}}$]	5000	5000	-	9362	-
η_{fuel} [%]	46.8	50.5	7.9	46.5	0.6
T_{PEN} [K]	1134	1096	3.4	1119	1.3
T_{ic} [K]	1120	1095	2.2	1119	0
T_{af} [K]	1128	1094	3.0	1116	1.1
T_{cf} [K]	1108	1093	1.4	1113	0

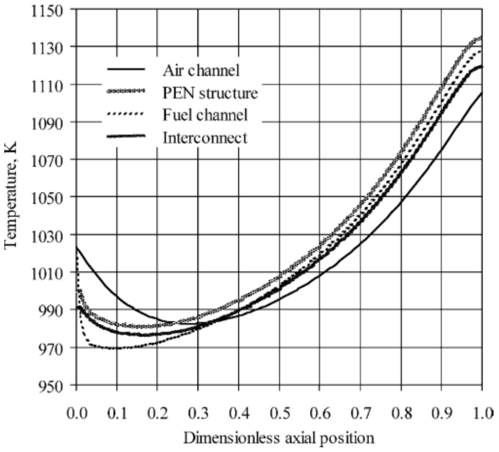

Figure 4.8: Fuel and air channels, PEN structure, and interconnect temperature along the cell length [26].

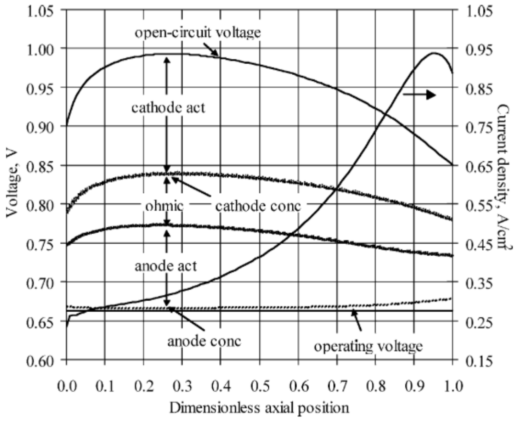

Figure 4.9: Predicted voltage, current density, and contribution of all the various potential losses along the cell length [26].

Dynamic validation

In this section the dynamic behaviour of the 0-D model is compared with results presented by Iora et al. [72] and by Salogni et al. [33]. Both publications report dynamic simulation results computed with the 1-D SOFC model developed by Aguiar et al. [26]. To validate the 0-D SOFC model on dynamic behaviour the model is tested with a ramp change in current density of $+-2000\,\mathrm{A\,m^{-2}}$ in 60 seconds. This load change is introduced when the model achieved steady state conditions (t=0). During this load change the fuel utilization and air excess ratio are kept constant, which means that the fuel and air mass flow rates are adjusted to maintain the pre-set fuel utilization and air excess ratio.

Figure 4.10 depicts the normalized voltage curve. Figure 4.11 depicts the normalized PEN temperature curve. The model input parameters are as provided in table 4.5.

Figure 4.10 shows that overall dynamic behaviour of the 0-D model and reference model qualitatively concur. The simulation shows an overshoot of cell voltage followed by a relaxation period, leading to the final steady-state voltage. This overshoot behaviour can be assigned to the difference in time scale of the chemical and thermodynamic physics. Direct after the load change, the chemical model adapts and the cell voltage follows. The thermodynamic response lags behind and needs more time to establish steady state. Figure 4.11 shows that overall thermodynamic behaviour concurs.

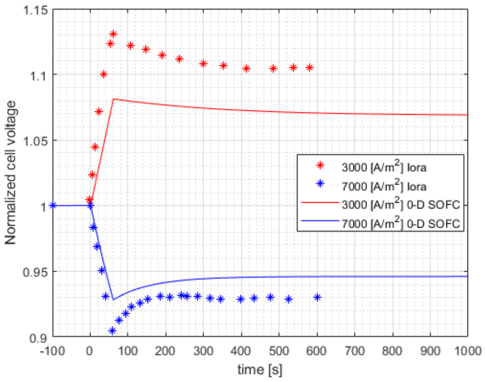

Figure 4.10: Normalized cell voltage responses to load changes, from $i = 5000$ A m^{-2} to $i = 3000$ A m^{-2} and $i = 7000$ A m^{-2} compared with data from ref. [72].

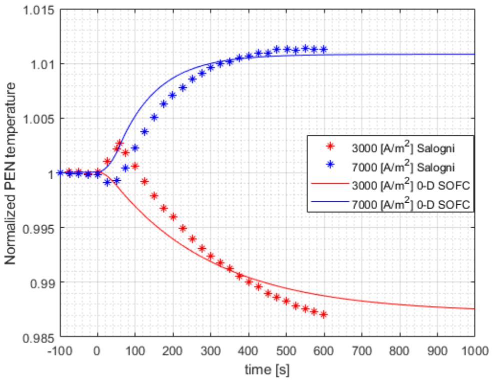

Figure 4.11: Normalized PEN temperature response to to load changes, from $i = 5000$ A m^{-2} to $i = 3000$ A m^{-2} and $i = 7000$ A m^{-2} compared with data from ref. [33].

4.5. SOFC model operating parameter sensitivity analysis

This section describes the operational parameter sensitivity analysis of the developed SOFC model including pre-reformer and anode off-gas recycling. Unless otherwise stated, the inlet conditions for this analysis are provided in table 4.7. In this analysis, the pre-reformer is operated at the same temperature as the SOFC stack and subtracts its reforming heat from the SOFC stack[3].

Table 4.7: SOFC model analysis benchmark initial conditions.

Parameter	**Value**	**Unit**
T_{air}	1023	K
p_{air}	$1 \cdot 10^5$	Pa
T_{fuel}	1023	K
p_{fuel}	$1 \cdot 10^5$	Pa
i	5000	A m^{-2}
U_f	81	%
λ_{air}	8.5	-
n_{cells}	11000	-
$T_{prereform}$	1023	K
$p_{prereform}$	$1 \cdot 10^5$	Pa
$O/C_{prereform}$	2	-
REF	0.1	-
$AOGRR$	0	-

Figure 4.12 and 4.13 depict the cell voltage and temperature for varying current density. The cell voltage transient curves concur with the evolution of the temperature profiles. As already indicated by literature (figure 2.6) the highest cell voltage (and efficiency) is achieved at the lowest current density. Operating at higher SOFC current density results in a higher PEN temperature also.

Figure 4.14 and 4.15 depict cell voltage and SOFC efficiency for varying fuel utilization. If fuel utilization increases, open-circuit voltage E decreases and concentration losses ΔV_{conc} increase, hence cell voltage V_{cell} decreases (Eq. 4.42). If fuel utilization increases, also the PEN temperature increases (figure 4.16). At higher temperatures, the Ohmic losses ΔV_{ohm} and activation losses ΔV_{act} decrease, hence cell voltage increases. For demonstrated fuel utilizations the highest cell voltage is achieved at 81 % fuel utilization. SOFC standalone efficiency is calculated with ingoing fuel only, the left-over fuel in the anode off-gas is considered as loss (eq. 4.57). Therefore the highest efficiency is achieved at the highest fuel utilization (with constant air excess,

---

[3] In configuration A, the pre-reformer reaction heat sink is included in the SOFC single cell energy balance.

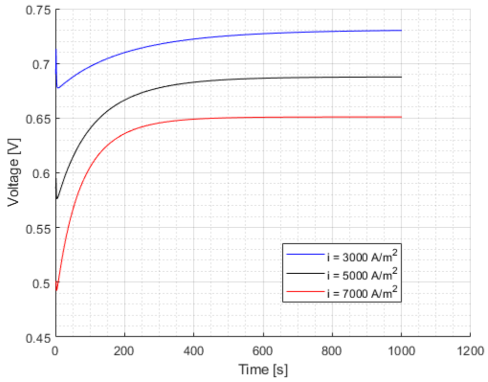

Figure 4.12: Predicted cell voltage against time for i = 3000, 5000, and 7000 $\mathrm{A\,m^{-2}}$.

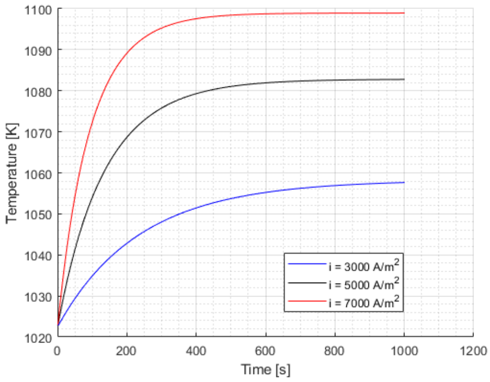

Figure 4.13: Predicted PEN temperature against time for i = 3000, 5000, and 7000 $\mathrm{A\,m^{-2}}$.

or in-active controlled stack temperature).

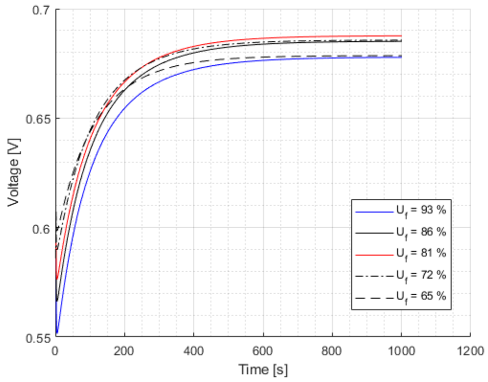

Figure 4.14: Predicted cell voltage against time for U_f = 93, 86, 81, 72, and 65 %

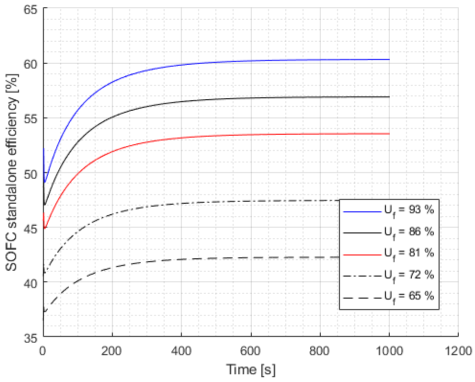

Figure 4.15: SOFC stand alone efficiency (LHV, DC) against fuel utilization for U_f = 93, 86, 81, 72, and 65 %

Figure 4.17 and 4.18 depict the cell voltage and temperature for varying air excess ratio. The excess air is flowing along the cathode and provides cooling to the SOFC stack, as can be seen in figure 4.18. As mentioned before, high operating temperatures improves cell voltage. However, to avoid thermal stresses in a cell, the maximum allowable temperature gradient is 10 $\mathrm{K\,cm^{-1}}$ [71]. In order to optimize operating temperature, and hence cell voltage, the air excess ratio is controlled by a PI controller. Figure 4.19 depicts the air excess against running time. The initial air excess was 2 and is increased to 3.9 in order to keep the SOFC stack temperature within allowable temperature limits (in this case ΔT_{cell} = 100 K).

Figure 4.20 and 4.21 depict the cell voltage and temperature for varying methane pre-reforming ratios. The solid lines depict configuration A, where the pre-reformer is integrated in the SOFC stack module (ISM), and obtained its reaction heat from the SOFC cell. The pre-reformer is operated at SOFC inlet temperature (1023 K) in configuration A. The dashed lines represent configuration B, where the pre-reformer is operated as stand-alone component, at 773 K (500 °C). As can be seen in the figures, increasing the pre-reformer ratio has opposite effects on configuration A and configuration B. For configuration A: when the pre-reformer ratio is increased, it is shown that more heat is extracted from the SOFC stack, thus the PEN temperature is decreased. The cell voltage is increased for higher pre-reformer ratios, so the electrochemical conversion is more effective. For configuration B: when the pre-reformer ratio is increased, the heat absorption by direct internal reforming is decreased and the cell heats up. Due this high PEN temperature, the cell voltage is further increased compared to configuration A. In order to get a higher cell voltage with configuration A, the cell temperature should be increased by lowering the air excess (taking the limits into account).

Figure 4.22 and 4.23 depict the cell voltage and temperature for varying anode off-gas recycling ratios. If anode off-gas recycling is applied, the cell voltage is increased and PEN temperature decreased. Two important observations can be made at the inlet of the SOFC. First: due to applied anode off-gas recycling, the fuel

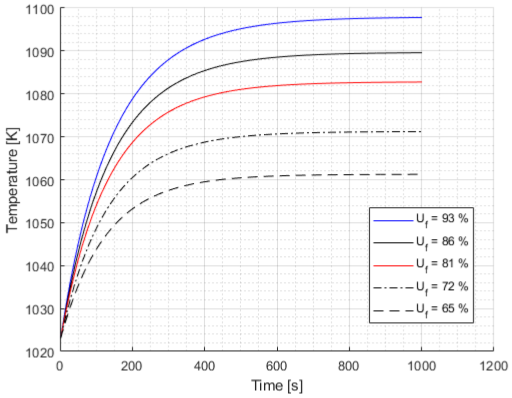

Figure 4.16: Predicted PEN temperature against time for U_f = 93, 86, 81, 72, and 65 %

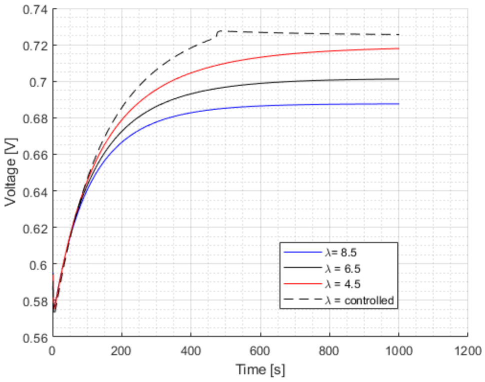

Figure 4.17: Predicted cell voltage against time for air excess ratios: λ = 8.5, 6.5, 2.5, and PI controlled.

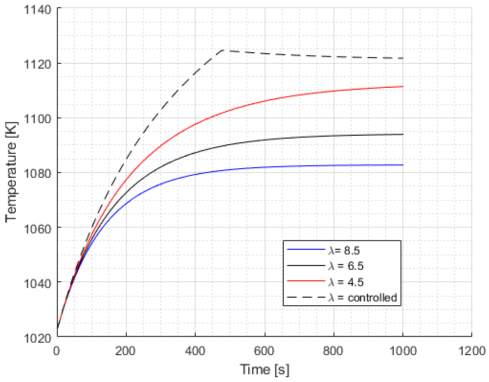

Figure 4.18: Predicted PEN temperature against time for air excess ratios: λ = 8.5, 6.5, 2.5, and PI controlled.

flow rate at the SOFC-anode is increased, which reduced single pass fuel utilization and decreased PEN temperature. Second: the fuel mixture at the SOFC-anode contains relative more hydrogen, which makes the SOFC electrochemistry more effective and thus increases cell voltage. Moreover, when $AOGRR$ is increased, amount of required pre-reformer-steam is reduced or even cancelled (table 4.8). Pre-reformer steam demand affects standalone SOFC system efficiency and is an important loss factor, which can be reduced by applying anode off-gas recycling.

Table 4.8: Pre-reformer external steam supply [kg/s] and fuel utilization for varying $AOGRR$.

Parameter	**$AOGRR$ = 0**	**$AOGRR$ = 0.3**	**$AOGRR$ = 0.6**	**Unit**
$\dot{m}_{steam}$	$3.1 \cdot 10^{-2}$	$1.6 \cdot 10^{-2}$	0	$\mathrm{kg\,s^{-1}}$
$U_{f,sp}$	81	75	63	%
$U_{f,net}$	81	81	81	%

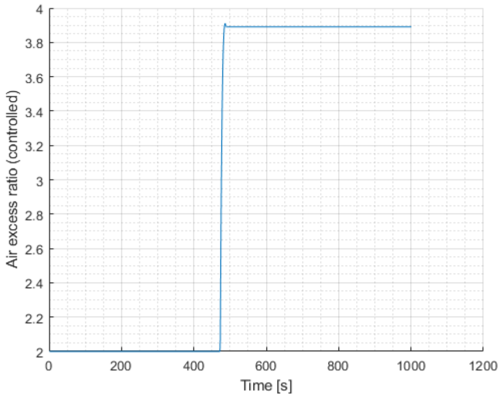

Figure 4.19: Air excess ratio controlled by a PI controller.

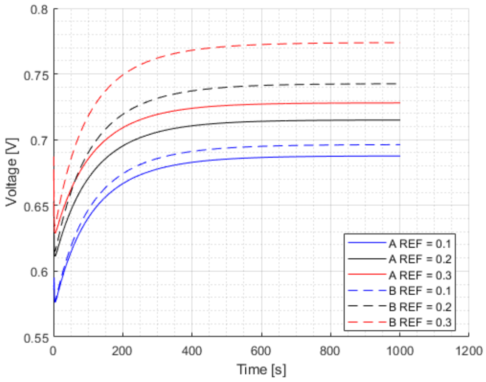

Figure 4.20: Predicted cell voltage againt time for *REF* = 0.1, 0.3, 0.5 and configuration A (solid line) and B (dashed line).

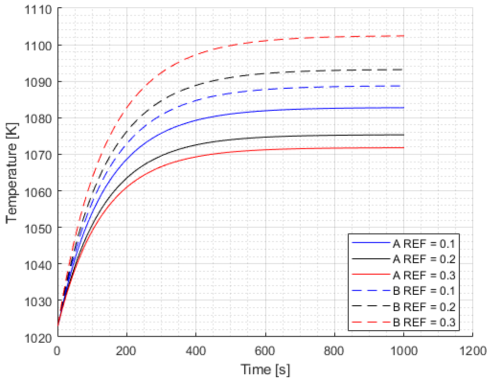

Figure 4.21: Predicted PEN temperature against time for *REF* = 0.1, 0.3, 0.5 and configuration A (solid line) and B (dashed line).

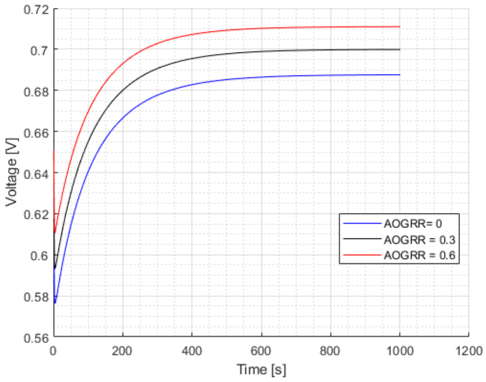

Figure 4.22: Predicted cell voltage againt time for *AOGRR* = 0, 0.3, and 0.6.

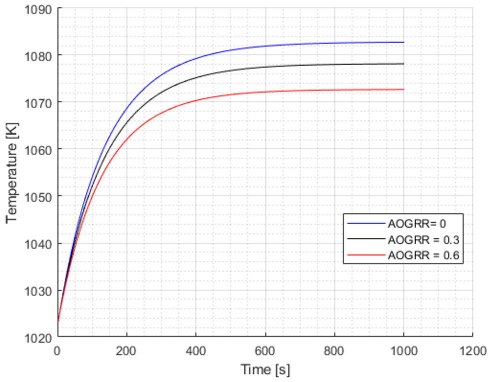

Figure 4.23: Predicted PEN temperature against time for *AOGRR* = 0, 0.3, and 0.6.

4.6. Conclusion

A computationally fast and dynamic 0-D SOFC model including a methane pre-reformer is developed. The model can compute temperature curves, anode off-gas composition, flow rates, and electric power. Input parameters are: fuel flow rate (or fuel utilization), current density, air excess ratio, and methane pre-reforming ratio. The dynamic model is developed in such a way that either the dynamic performance can be predicted or steady state results can be used in the hybrid system study.

A model validation is conducted consisting of electrochemical model analyses, steady state analyses, and a qualitative dynamic analyses. To validate the model, a comparison is made with reference data published in ref. [26, 33, 72]. In general, the model predicts the SOFC behaviour as physically expected. The dynamical behaviour concurs with the reference model. The steady state validation shows some deviations with reference values and can potentially be assigned to the lumped parameter approach versus the distributed parameter approach of the reference model. For this work these deviations are accepted. If more accurate prediction of SOFC performance is required, the 0-D model has to be calibrated with experimental data or with data obtained from higher order models.

A parameter sensitivity analysis is performed to investigate the dependency of cell voltage and cell temperature to various operating parameters. It is concluded from this analyses that:

- Operating low current density results in highest cell voltage, which is at the expense of power density.
- High fuel utilization results in high SOFC stand alone efficiency, but is not linearly coupled to cell voltage increase due to the effects of changing cell temperature.
- Air excess ratio is an important parameter to optimize SOFC temperature in order to obtain maximum cell voltage.
- Increasing amount of methane pre-reforming has a positive effect on cell voltage, the temperature development depends on the method of pre-reformer-heat integration.
- It is shown that anode off-gas recycling positively affects cell voltage at lower single pass fuel utilization. Operating at low single pass fuel utilization reduces SOFC degradation risks as discussed in section 2.1.5.

5

Internal Combustion Engine model

The ICE model is developed based on an in-house developed mean value first principle (MVFP) engine model [56, 59], and is calibrated with an experimental research carried out by Sapra et al. [20]. The relevant engine is a Caterpillar-G3508 eight cylinder turbocharged spark-ignited gas engine with a rated power of 500 kW at 1500 rpm. The developed engine model provides insights of engine behaviour when fueled with a hydrogen-natural gas blend and is used in the hybrid system study for performance calculations and heat integration. The used hydrogen-natural gas blends are provided in table 5.1. The ICE model is developed in MATLAB Simulink.

Table 5.1: Hydrogen-natural gas fuel blends for ICE modeling.

Fuel blends	**Natural gas volume [%]**	**Hydrogen volume [%]**
NG	100	0
10HNG	90	10
20HNG	80	20

5.1. Model description

The ICE model consists of two sub-models: a sub-model describing the in-cylinder process, which is expressed using a Seiliger cycle (figure 5.1) and a gas exchange sub-model simulating the interaction between the in-cylinder process and the turbocharger system (figure 5.2).

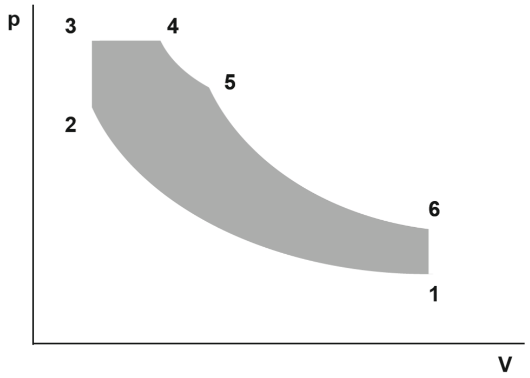

Figure 5.1: In-cylinder process depicted as six stage Seiliger cycle in a p-V diagram [1].

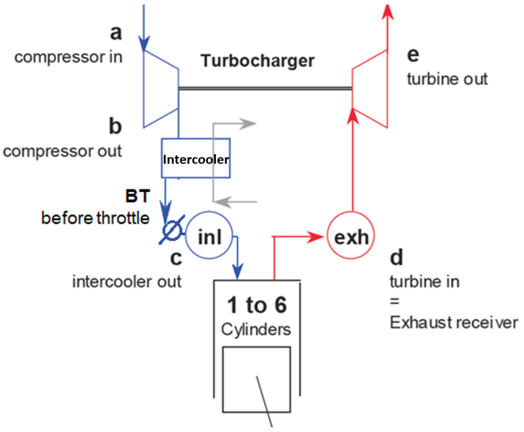

Figure 5.2: Gas exchange process (labelled a-e) coupled with in-cylinder process (labelled 1-6). The stage 'before throttle' (BT) is typical for this type of HC gas engines. Original taken from [1].

The applied MVFP modeling approach relies on experimental data which is pre-processed in a detailed engine model. Figure 5.3 depicts the MVFP model with the the preceding steps. The physical principles which are indicated in this figure are explained in the next paragraphs.

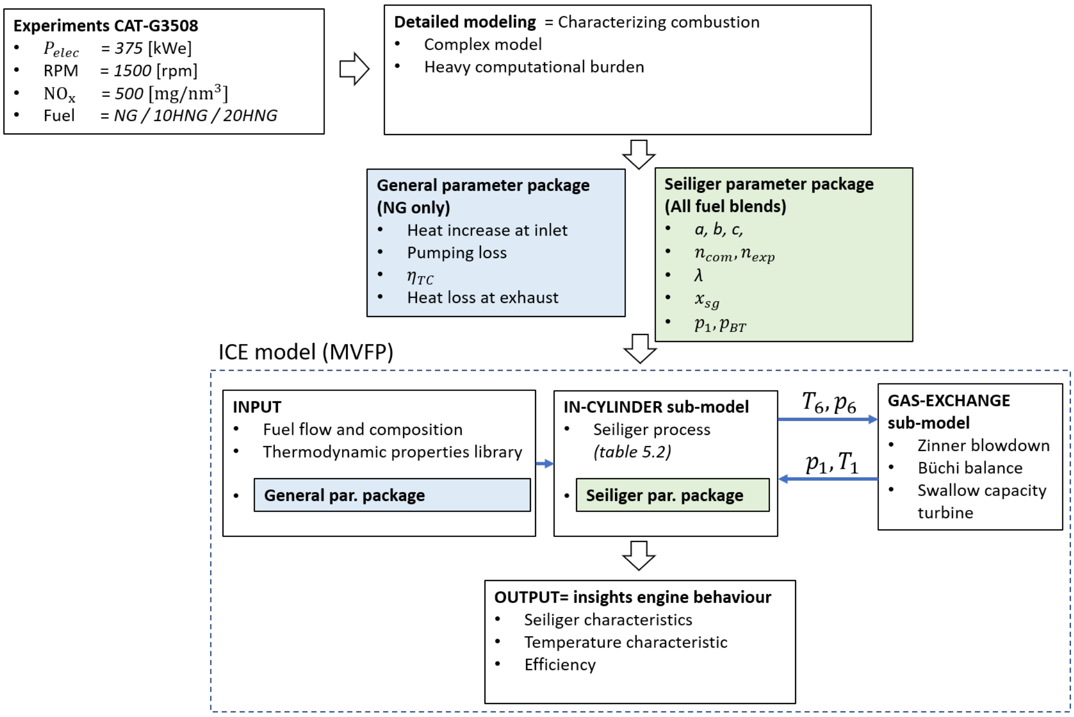

Figure 5.3: ICE model in relation with experiments and detailed modeling

5.1.1. In-cylinder sub-model

The in-cylinder sub-model computes indicated work of the engine cycle using Seiliger equations. The in-cylinder conditions at point ’1’, also called trapped conditions, are the input of these equations. The trapped mass at the start of compression m_1 (kg) is determined with the ideal gas law eq. 5.1.

$$m_1 = \frac{p_1 V_1}{R_1 T_1} \tag{5.1}$$

The charge air pressure p_1 (Pa) follows from the turbocharger-compressor pressure ratio which is calculated in the gas exchange sub-model. V_1 is the cylinder volume at start of the compression (m^3). For cylinder geometric calculations see appendix E. The gas constant R_1 (J kg^{-1} K^{-1}) can be determined when the mass fraction ($x_{sg,\ air,\ and\ f}$) of the trapped mass is known (eq 5.2). The gas constant $R_{sg,\ air,\ and\ f}$ for each constituent is invoked from the thermodynamic properties library.

$$R_1 = x_{sg} \cdot R_{sg} + x_{air} \cdot R_{air} + x_f \cdot R_f \tag{5.2}$$

Typical for this gas engine is that the gaseous fuel is introduced at the air intake before the compressor. This means that the engine is filled with a pre-mixed air-fuel mixture. In other words, together with air, a fraction of fuel is also present in the trapped mass. Moreover, as no scavenging is applied, a substantial amount of residual gas (of previous cycle) is also present. The residual gas consists of stoichiometric gas and air. From experiments the stoichiometric gas mass fraction x_{sg} is known. From the fuel specifications the stoichiometric air to fuel ratio σ is set, and from experiments, the air excess ratio λ is known. With these known parameters the trapped mass compositions are calculated with eq. 5.3-5.5.

$$x_{sg} = 0.175 \quad \text{from experiments} \tag{5.3}$$

$$x_f = \frac{(1 - x_{sg})}{(1 + \sigma \cdot \lambda)} \tag{5.4}$$

$$x_{air} = 1 - x_{sg} - x_f \tag{5.5}$$

T_1 is the trapped mass temperature at start of compression and depends on an amount of heat pick up from the inlet duct and a certain amount of heat increase due mixing with residual mass from previous cycle. T_1 (K) is estimated with eq. 5.6, where ϵ is a fitting parameter[1]. T_{INL} is the inlet duct temperature and T_c is the charge air temperature. Both can be measured during experiments.

$$T_1 = T_c + \epsilon(T_{inl} - T_c) \tag{5.6}$$

With the trapped conditions the Seiliger equations can be solved (table 5.2). The parameters characterizing the Seiliger shape (a, b, c, n_c, n_e) are used to calculate the state parameters at the six stages. With the calculated temperatures and the thermodynamic properties, at corresponding stage, the corresponding stage specific heat q_{ij} ($\mathrm{J\,kg^{-1}}$) and stage specific work w_{ij} ($\mathrm{J\,kg^{-1}}$) are calculated. The calculated pressure and temperature after expansion, at Seiliger point 6, are required as input for the gas exchange sub-model. The sum of the stage specific work is the indicated specific work w_i of the cycle (eq. 5.7).

$$w_i = w_{12} + w_{34} + w_{45} + w_{56} \tag{5.7}$$

To calculate the amount of effective work per cycle, a certain amount of work loss due to gas exchange (pumping loss) is taken into account. Pumping loss is loss when the fresh charge pressure during the intake stroke is less than the exhaust gas pressure during the exhaust stroke. Figure 5.4 illustrates the pumping loss principle in a complete cycle. In the model a pumping loss of 4.0 % is applied which functions as a tuning parameter to fit the model data to experimental data.

$$w_{cycle} = w_i \cdot (1 - 0.04) \tag{5.8}$$

Using the work per cycle, the engine brake power is calculated. The electric power P_e (We) and efficiency are calculated assuming a generator efficiency of 95 % and an engine mechanical efficiency of 90 % (eq. 5.9 and 5.10).

$$P_e = m_1 \cdot w_{cycle} \cdot \frac{n \cdot i}{k} \cdot \eta_{mech} \cdot \eta_{gen} \tag{5.9}$$

$$\eta_e = \frac{P_e}{m_f \cdot \frac{n \cdot i}{k} \cdot LHV} \tag{5.10}$$

In this equation, n is the engine speed in revolutions per second, i is the number of cylinders, k is the number of revolutions per cycle ($k = 2$ for 4-stroke engines), η_{mech} is the engines mechanical efficiency, η_{gen} is the generator efficiency, m_1 is the trapped mass per cylinder per cycle (kg), and m_f is the mass of fuel per cylinder per cycle (kg).

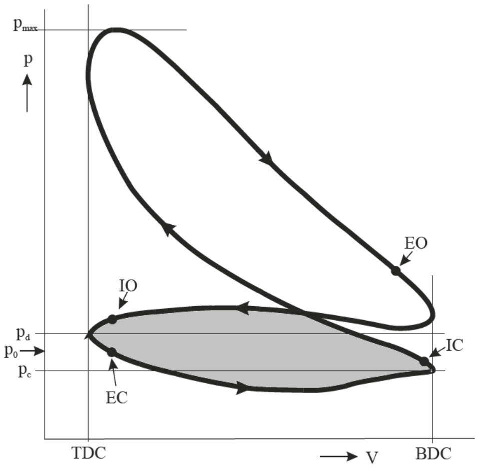

Figure 5.4: Pumping loss (grey field) in p-V diagram, original taken from [73].

---

[1] Based on the detailed model as part of ref. [20]

Table 5.2: Seiliger cycle equations, taken from [1].

Seiliger stage	**Volume** V	**Pressure** p	**Temperature** T	**Specific work** w	**specific heat** q
1-2	$\frac{V_1}{V_2} = r_c$	$\frac{p_2}{p_1} = r_c^{n_c}$	$\frac{T_2}{T_1} = r_c^{(n_c-1)}$	$w_{12} = \frac{-R_{cyl}(T_2-T_1)}{(n_c-1)}$	$q_{12} = 0$
2-3	$\frac{V_3}{V_2} = 1$	$\frac{p_3}{p_2} = a$	$\frac{T_3}{T_2} = a$	$w_{23} = 0$	$q_{23} = c_{v,cyl23}(T_3 - T_2)$
3-4	$\frac{V_4}{V_3} = b$	$\frac{p_4}{p_3} = 1$	$\frac{T_4}{T_3} = b$	$w_{34} = R_{cyl}(T_4 - T_3)$	$q_{23} = c_{p,cyl34}(T_4 - T_3)$
4-5	$\frac{V_5}{V_4} = c$	$\frac{p_4}{p_5} = c$	$\frac{T_5}{T_4} = 1$	$w_{45} = R_{cyl} T_4 \ln(c)$	$q_{45} = R_{cyl} T_4 \ln(c)$
5-6	$\frac{V_6}{V_5} = \frac{r_{EO} r_c}{bc}$	$\frac{p_5}{p_6} = \left(\frac{r_{EO} r_c}{bc}\right)^{n_e}$	$\frac{T_5}{T_6} = \left(\frac{r_{EO} r_c}{bc}\right)^{(n_e-1)}$	$w_{56} = \frac{R_g(T_5-T_6)}{(n_e-1)}$	$q_{56} = 0$

5.1.2. Gas exchange sub-model

The gas exchange sub-model predicts the trapped pressure p_1 required for in-cylinder sub-model, while the input of the sub-model is the pressure and temperature (p_6 and T_6) which are computed outputs of the in-cylinder sub-model. In order to compute p_1, the gas exchange sub-model solves a set of equations consisting of: the Zinner blowdown, swallow characteristic turbine, and the Büchi balance.

Zinner blowdown

The blowdown and exhaust process of the cylinder is based on a theory by Zinner [74]. Zinner assumed that after opening of the exhaust valve, the gases in the cylinder instantaneously blow down in the outlet receiver. At the start of this process the temperature and pressure in the cylinder are T_6 and p_6 and the pressure in the outlet receiver is p_d. At the end of the process the cylinder and outlet receiver are considered as one and the same volume with temperature and pressure T_{bld} and p_d. The derivation of this equation is expressed by Stapersma in [73]. The blowdown temperature is computed with eq. 5.11.

$$T_{bld} = T_6 \left(\frac{1}{n_{bld}} + \frac{n_{bld} - 1}{n_{bld}} \frac{p_d}{p_6} \right) \tag{5.11}$$

Where n_{bld} is the polytropic expansion coefficient of the blowdown process taking care for heat loss in the cylinder, exhaust valve, and duct. Since in this engine no scavenging is present, and thus no slipped air, the temperature at stage 'd' is equal to the blow down temperature (eq. 5.12).

$$T_d = T_{bld} \tag{5.12}$$

Swallow capacity turbine

The pressure before the turbine p_d is determined by the swallow characteristic of the turbine. In previous engine modeling it was conventional to use compressor and turbine maps to determine this air swallow capacity, however an alternative method is using an 'ellipse law expression' to estimate the variation in swallowing capacity with pressure ratio as derived by Dixon [75]. Geertsma et al. [76] uses Dixon's ellipse law to derive an expression for the exhaust pressure and is given in eq. 5.13.

$$p_d = \sqrt{\frac{(m_1 \cdot \frac{n \cdot i}{k})^2 \cdot R_g \cdot T_d}{\alpha_z^2 \cdot A_{eff}^2} + p_e^2} \tag{5.13}$$

Where α_z is the Zinner turbine area decrease factor, which is assumed to be 1 for a constant pressure turbocharger [73]. A_{eff} is the effective area of the turbine in (m^2), p_e is the pressure after the turbine, which is assumed to be atmospheric pressure. In this equation R_g is representing the gas constant for exhaust gas. R_g is determined alike eq. 5.2, but in this case with: $x_{sg} = \frac{(\sigma+1)}{(\lambda\sigma+1)}$, $x_{air} = 1 - x_{sg}$, and $x_f = 0$. Eq. 5.11 and 5.13 combined are solved as a quadratic equation as shown in eq. 5.14.

$$0 = p_d^2 - \left[\frac{\left(m_1 \cdot \frac{n \cdot i}{k}\right)^2 \cdot R_g \cdot T_6 \cdot \frac{(n_{bld}-1)}{n_{bld}}}{\alpha_z^2 \cdot A_{eff}^2 \cdot p_6} \right] \cdot p_d - \left[(\frac{\left(m_1 \cdot \frac{n \cdot i}{k}\right)^2 \cdot R_g \cdot T_6 \cdot \frac{1}{n_{bld}}}{\alpha_z^2 \cdot A_{eff}^2} + p_e^2 \right] \tag{5.14}$$

Büchi balance

Turbocharging of the engine works according to a principle first proposed by the Swiss engineer Alfred Büchi. The principle is as follows: the compressor is driven by a turbine that receives its power from the enthalpy flow of the exhaust gases. The turbine is located in the gas stream after the exhaust receiver which collects the outlet gases of the cylinders. The compressor is located after the inlet filter and feeds compressed air (and fuel) to an inlet receiver that is supplying charge to the cylinders. The power necessary to drive the compressor in the turbocharger must be equal to the power delivered by the turbine. In practice the intake and outlet losses and the efficiencies of compressor an turbine are far from ideal. Nevertheless, it is possible to operate a turbocharger as a bottom cycle under a in-cylinder cycle and at the same time have a positive pressure difference across the engine[2] due to the fact that the specific heat constant of the hot exhaust gas in the turbine is higher than the specific heat constant of the relative cool air in the compressor. With this principle, the Büchi balance is expressed and is the main equation for turbocharging (eq. 5.15). Particularly for this model, the Büchi balance is used to determine the charge pressure (pressure before inlet receiver throttle p_{BT}) that can be delivered by the compressor. The pressure before throttle p_{BT} is calculated with the compressor ratio as in eq. 5.16.

$$\pi_{com} = \left[1 + \beta \cdot \delta_f \cdot \frac{c_{p,g}}{c_{p,a}} \cdot \eta_{TC} \cdot \frac{T_d}{T_a} \cdot \left(1 + \frac{1}{\pi_{tur}^{\frac{\gamma_g - 1}{\gamma_g}}} \right) \right]^{\frac{(\gamma_a - 1)}{\gamma_a}} \tag{5.15}$$

$$\pi_{com} = \frac{p_{BT}}{p_{amb}} \tag{5.16}$$

$$\pi_{tur} = \frac{p_d}{p_e} \tag{5.17}$$

$$\tag{5.18}$$

Where β is 1 for a constant pressure system [73] and δ_f is the fuel addition factor. In this case δ_f is 1 because the fuel is added before the compressor. Between compressor and turbine no extra mass is added or lost. The specific heats (c_p) at constant pressure and the ratio of specific heats γ at station 'a' and for exhaust gas (subscript g) is calculated using mass fractions and chemical species depending properties.

To get the charge pressure and p_1, an 'orifice factor' is used to simulate a pressure decrease due to a throttle valve located before inlet receiver (depicted in figure 5.2). p_1 is calculated with eq. 5.19, the orifice factor is based on experimental data.

$$p_1 = p_c = p_{BT} \cdot \text{orifice factor} \tag{5.19}$$

Exhaust gas temperature

The exhaust temperature T_e is calculated from the cylinder discharge temperature T_d, using isentropic turbine efficiency $\eta_{turb,is}$ and a certain amount of heat loss in exhaust gas receiver and duct (eq. 5.20-5.25).

$$T_{e,ID} = T_d - \frac{w_{turb}}{c_{p,g}} \tag{5.20}$$

$$w_{com} = c_{p,a} \cdot (T_b - T_a) \tag{5.21}$$

$$w_{turb} = w_{com} \frac{\eta_{turb,is}}{\eta_{TC}} \tag{5.22}$$

$$T_{e,ID} = T_d - \frac{\eta_{turb,is}}{c_{p,g} \cdot \eta_{TC}} \cdot c_{p,a} \cdot (T_b - T_a) \tag{5.23}$$

$$T_{e,ID} = T_d - \frac{\eta_{turb,is}}{c_{p,g} \cdot \eta_{TC}} \cdot c_{p,a} \cdot \left(\left(\frac{p_b}{p_{amb}} \right)^{(\frac{\gamma_a - 1}{\gamma_a})} - T_a \right) \tag{5.24}$$

$$T_e = T_{e,ID} - \frac{q_{hl\ exhaust}}{c_{p,g}} \tag{5.25}$$

Where $q_{hl\ exhaust}$ is determined using the measured exhaust temperature from experiments (general parameter package) (eq.5.26).

$$q_{hl\ exhaust} = c_{p,g} \cdot (T_{e,ID} - T_{e,experiment}) \tag{5.26}$$

---

[2] The inlet receiver pressure of the engine can be higher than the exhaust receiver pressure that is required before the turbine.

5.1.3. Thermodynamic properties library

As part of the model input a thermodynamic properties library is invoked to determine thermodynamic properties of: air, stoichiometric gas, and (blended fuel). These properties are: gas constant R, isobaric heat capacity c_p, fuel lower heating value (LHV), and stoichiometric ratio σ. The calculation methods applied in the thermodynamic properties library are explained in appendix F. For this work the fuel input is limited to natural gas with 0 %, 10 %, or 20 % hydrogen addition (table 5.1).

5.1.4. Engine specifications and experimental data set

The MVFP model depends on experimentally obtained data and pre-processing results from a detailed engine model. The experiments and detailed modeling is conducted and made available by Sapra et al. [20] as part of a study to investigate hydrogen-natural gas engines for marine applications. An extensive description of both essential preceding steps is outside the scope of present thesis. For a detailed description of the experimental set-up a reference is made to ref. [20]. A comprehensive description of the pre-processing can be found in ref. [57]. The result of pre-processing work, required for this work, is provided in table 5.3.

Table 5.3: Seiliger parameter package

Symbol	NG	10HNG	20HNG	unit
a	1.3639	1.4162	1.4769	-
b	1.4522	1.3870	1.3369	-
c	1.7919	1.7651	1.6845	-
n_e	1.2818	1.2830	1.2841	-
n_c	1.3318	1.3320	1.3324	-

Experimental set up

Engine measurements were performed on the Caterpillar-G3508 test engine operating at 375 kWe and 1500 rpm. The engine is coupled to a generator for constant speed operation. At the engine's fuel intake, the natural gas flow was partially replaced by 10 volume percent and 20 volume percent hydrogen. See table 5.4 for engine specifications.

During the experiments the engine air-intake is controlled (λ) such that the engine is operating on the one hand considering NO$_x$ emission as a limit (IMO TIER-III regulation [50]) and on the other hand considering engine misfire as a limit (leaning limit of the engine operating window). The final reported results are taken at the maximum allowed NO$_x$ emissions for this engine (500 mg/nm^3 at 5 % oxygen). The maximum engine power during experiments was limited to 375 kWe at 1500 rpm, since it turned out that at higher power ratings the turbocharger becomes a limiting factor when operating on natural gas-hydrogen blends [3]. Finally three sets of measured data are available for present study (table 5.5) [20].

Table 5.4: Engine specifications, CAT-G3508.

Parameter	Symbol	Value	unit
Number of cylinders	i	8	-
Bore	D_B	0.17	m
Stroke	L_s	0.19	m
Rated speed	N	1500	rpm
Rated power	P_b	500	kW
Compression ratio	ϵ	12:1	-
Engine mechanical eff.	η_{mech}	0.9	-
General efficiency	η_{gen}	0.95	-

---

[3] Engine operation with hydrogen-natural gas blends leads to a higher trapped mass (explained in section 5.2), which means a higher demand of the turbocharger capacity. Operating at a maximum of 375 kWe prevents that the turbocharger's maximum swallow capacity limits the experiments.

Table 5.5: Engine experimental results.

Symbol	**NG**	**10HNG**	**20HNG**	**unit**
% H_2	0	10	20	%
P_e	375	375	375	kWe
η_e	33.68	34.25	34.77	%
$\dot{\phi}_{NG}$	123.4	117.2	110.58	$m^3 h^{-1}$
$\dot{\phi}_{H_2}$	0	13.0	27.7	$m^3 h^{-1}$
T_e	650	639	631	K
p_1	1.68	1.72	1.74	bar
p_{BT}	1.92	1.86	1.86	bar
λ	1.6265	1.6857	1.7378	-
x_{sg}	0.175	0.1705	0.182	-
NO_x	500	500	500	mg/nm^3 (at 5 % oxygen),

5.1.5. Model validation

Three parameter sets (table 5.3) are loaded in the developed MVFP engine model in order to validate engine performance. The results are compared with performance results from experiments and detailed engine modeling. It can be concluded that the MFVP model is computing accurate results, the deviation is 1.5 %, see appendix G.

5.2. Simulations: effect of hydrogen addition on engine behaviour

ICE model simulations are carried out to investigate effects of hydrogen addition to natural gas on engine performance. The simulations are done with the three available fuel blends. Figure 5.5 shows the p-V diagram, figure 5.6 depicts the temperatures at the in-cylinder Seiliger points. On the basis of this figures the following conclusions are drawn.

- Looking to the p-V diagram and particularly to the Seiliger characteristics (figure 5.5): hydrogen addition increased the maximum cylinder pressure (increasing Seiliger parameter a) and reduces combustion duration (decreasing Seiliger parameter b and c). This characteristic change increases combustion stability and reduces cycle-to-cycle variations. A higher overall combustion rate reduces cycle-to-cycle variations as indicated by Robinet et al. [77] and demonstrated by Sapra et al. [20]. This fact allows the engine to lean to higher air-excess ratios. In other words hydrogen extends the engine's operating window, which makes the engine dynamically stronger (expands the operating window which is depicted in figure 2.13).
- As indicated in figure 5.5, hydrogen addition requires more work form the compression stroke, as there is more trapped mass to compress. Hydrogen addition makes the expansion stroke more effective due an earlier end of combustion (Seiliger point 5).
- Typically for this set of experiments is that the maximum cylinder temperatures are equal, regardless of the amount of hydrogen addition. As shown in figure 5.6, the temperatures at Seiliger point 4 and 5 are approximately the same. This is because the experiments are conducted at fixed NO_x emissions. Generally, NO_x emissions depend on engine speed, air intake and in-cylinder temperature. Since engine speed is kept constant (1500 rpm), the NOx emissions depend only on air intake and temperature. The Air intake is continuously controlled to investigate engine performance at constant NOx emissions (500 mg/nm^3), thus at fixed NO_x emissions the maximum cylinder temperature is also fixed [78].
- When adding hydrogen, the temperature after isochoric combustion is higher (figure 5.6, Seiliger point 3), due to a higher combustion rate of the blend. The temperature before blowdown is lower (Seiliger point 6), due to the more effective expansion stroke.
- The cylinder discharge temperature T_d is also lower, which results in reduced turbocharger work. To compensate for reduced turbocharger work, while keeping engine power and NO_x on the same level,

the engine manifold throttle has to be opened further and the turbocharger has to spool up to ensure enough air is trapped in the cylinder (open 'BT' in figure 5.2).

- Hydrogen addition helps to improve engine's first law efficiency for simulated engine at fixed power (375 kWe, 1500 rpm) and NO_x-emissions (500 mg/nm^3, at 5 % oxygen). The efficiency is calculated as defined in eq. 5.27.

$$\eta_{ICE,LHV} = \frac{P_{e,ICE,AC}}{\dot{\phi}_{NG} \cdot \frac{1}{3600} \cdot LHV_{NG} + \dot{\phi}_{H_2} \cdot \frac{1}{3600} \cdot LHV_{H_2}} \tag{5.27}$$

Where $\dot{\phi}_{NG}$ is the volumetric flow rate of natural gas ($\mathrm{m^3\,h^{-1}}$), $\dot{\phi}_{H_2}$ is the volumetric flow rate of hydrogen ($\mathrm{m^3\,h^{-1}}$), the volumetric lower heating value of hydrogen is: $LHV_{H_2} = 1.0209\mathrm{e}4\ \mathrm{kJ\,m^{-3}}$ and the volumetric lower heating value of natural gas is $LHV_{NG} = 3.2488\mathrm{e}4\ \mathrm{kJ\,m^{-3}}$ (at atmospheric pressure and 300 K).

Table 5.6: Engine first law efficiency. CAT-G3508, 375 kWe, 1500 rpm, NO_x = 500 mg/nm^3 (at 5 % oxygen), at atmospheric pressure and 300 K.

Parameter	NG	10HNG	20HNG	unit
$\eta_{ICE,LHV}$	33.73	34.43	35.25	%

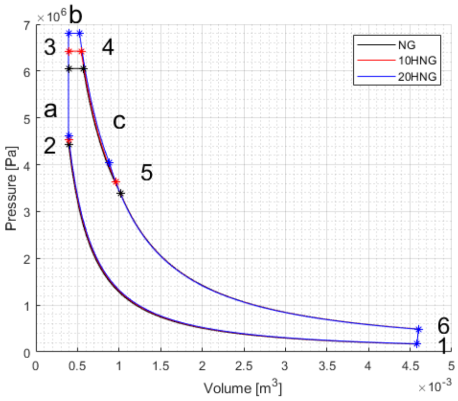

Figure 5.5: p-V diagram of MVFP engine model for: NG, 10HNG, and 20HNG. CAT-G3508, 375 kWe, 1500 rpm, NO_x = 500 mg/nm^3 (at 5 % oxygen).

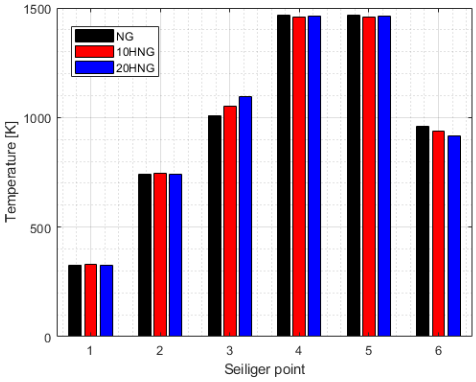

Figure 5.6: In-cylinder temperature of MVFP engine model for: NG, 10HNG, and 20HNG. CAT-G3508, 375 kWe, 1500 rpm, NO_x = 500 mg/nm^3 (at 5 % oxygen).

5.3. Engine model for hybrid system study

For the SOFC-ICE hybrid system study, the ICE model requirements are confined to fuel consumption in order to calculate system efficiency, and exhaust gas heat capacity which is required for system heat integration. Figure 5.7 depicts the engine model requirements for the hybrid system study.

The experimental data of interest for the hybrid system ICE model is provided in table 5.7. From this data two curves[4] are created to express natural gas volumetric flow rate $\dot{\phi}_{NG}$ ($\mathrm{m^3\,h^{-1}}$) and hydrogen volumetric flow rate $\dot{\phi}_{H_2}$ ($\mathrm{m^3\,h^{-1}}$) against hydrogen blend percentage. Successively, the inverse function is expressed which can calculate the hydrogen blend percentage in function of the hydrogen volumetric flow rate available in anode off-gas $\dot{\phi}_{AOG-H_2}$ (eq. 5.28). In other words: when considering the hybrid system, the hydrogen volumetric flow rate available in the AOG determines the amount of natural required to operate the engine at the required conditions (375 kWe, 1500 rpm, NO_x = 500 mg/nm^3 (at 5 % oxygen)). Figure 5.8 depicts the volumetric flow rate curves which are forming the ICE model for the hybrid system study. The volumetric flow rates at hydrogen blend percentages greater than 20 % (shaded area in figure) are based on extrapolated data and are not substantiated by experiments [20]. A similar approach is applied to express ICE exhaust gas heat capacity in function of hydrogen-blend-percentage. The ICE exhaust gas heat capacity is required for heat integration calculations.

---

[4] Second order polynomial

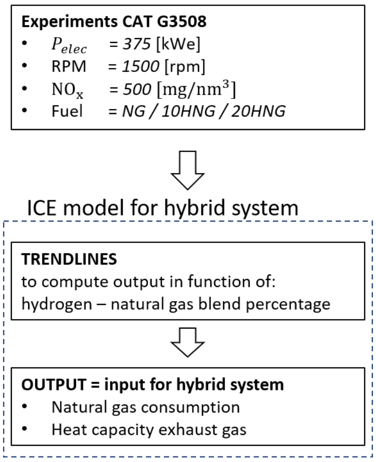

Figure 5.7: Engine model for hybrid system study

Table 5.7: Volume flow of natural gas and hydrogen at ICE intake. ICE exhaust gas temperature. Taken from engine experimental data CAT-G3508, 375 kWe, 1500 rpm, NO_x = 500 mg/nm^3 (at 5 % oxygen), at atmospheric pressure and 300 K.

Parameter	**NG**	**10HNG**	**20HNG**	**unit**
H_2 blend percentage	0	10	20	%
$\dot{\phi}_{NG}$	123.4	117.2	110.8	$m^3 h^{-1}$
$\dot{\phi}_{H_2}$	0	13.0	27.7	$m^3 h^{-1}$
Engine electric power	375	375	375	kWe (AC)
Temp. exhaust gas	650	639	631	K

Other AOG-species blended with the engine's natural gas supply are: CO_2, CO, and a small fraction of CH_4. While these species are also introduced in the ICE engine, the effects on engine performance are not taken into account in this work. Future ICE models for integration with SOFCs should focus on the effects of other AOG species on engine performance and should take the additional heating effects of CO and CH_4 into account.

$$blend_{H_2} = \frac{-1.2194 + \sqrt{1.2194^2 - 4 \cdot 0.0083 \cdot (\dot{\phi}_{AOG-H_2})}}{2 \cdot 0.0083} \tag{5.28}$$

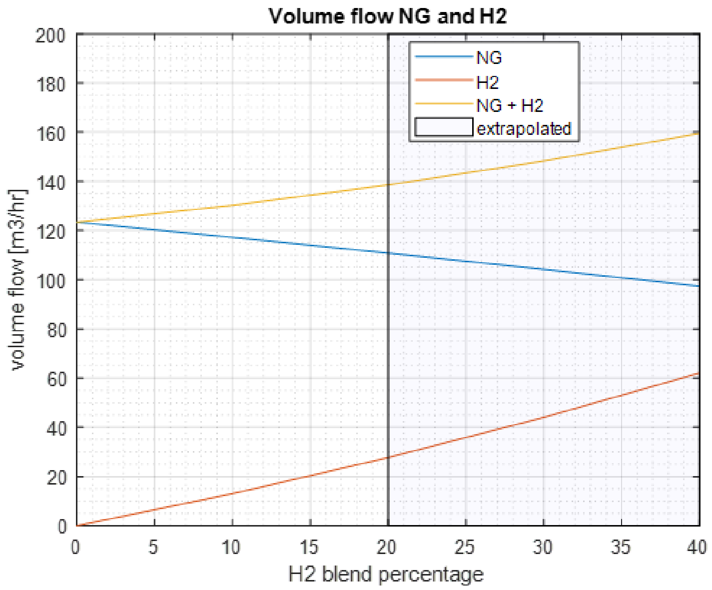

Figure 5.8: ICE model for hybrid system study. Total ICE fuel consumption: natural gas volumetric flow rate and hydrogen volumetric flow rate against hydrogen blend percentage. ICE at 375 kWe, 1500 rpm, NO_x = 500 mg/nm^3 (at 5 % oxygen). The shaded area (> 20 %) indicates extrapolated data.

5.4. Conclusion

The Caterpillar-G3508 spark ignited gas engine is selected to function as the reciprocating internal combustion engine in this SOFC-ICE hybrid system. This engine is selected because of the in-house availability of measured engine data which is based on experiments with three types of fuel blends. In this work these experimental data sets are used to calibrate the engine model. The used fuel blends are: (1) 100 % natural gas, (2) 10 % hydrogen - 90 % natural gas, and (3) 20 % hydrogen - 80 % natural gas. The experiments are carried out by Sapra et al. [20].

Operating the engine model as a standalone component provided understanding of engine behaviour when it is fueled with a hydrogen-natural gas blend. The following conclusions are drawn:

- Hydrogen-enrichment of natural gas improves engine efficiency. An addition of 20 % hydrogen to natural gas improves engine efficiency with 1.5 percent point.
- Hydrogen-enrichment of natural gas reduces engine's sensitivity for cycle-to-cycle variations which improves engine combustion stability and makes leaner engine operation possible.

Thereafter, a (simplified) ICE model for integration in the hybrid system model is developed. This version of the model computes the engine's natural gas consumption to calculate hybrid system efficiency, and provided the engine's exhaust gas heat capacity, which is required to compute hybrid system's heat integration.

6

Hybrid system model and simulations

Component models are developed in previous chapters, in this chapter these models are combined to form the SOFC-ICE hybrid system model. A hybrid system simulation study is conducted in order to identify relevant operating parameters and system configurations of SOFC-ICE hybrid systems for marine applications and to investigate their influence on system efficiency and performance.

6.1. Model description

The proposed SOFC-ICE hybrid system is introduced in chapter 3. Elaborating on this, a schematic representation of the proposed fuel streams is shown in figure 6.1. In this diagram the streams are labelled for further analysis.

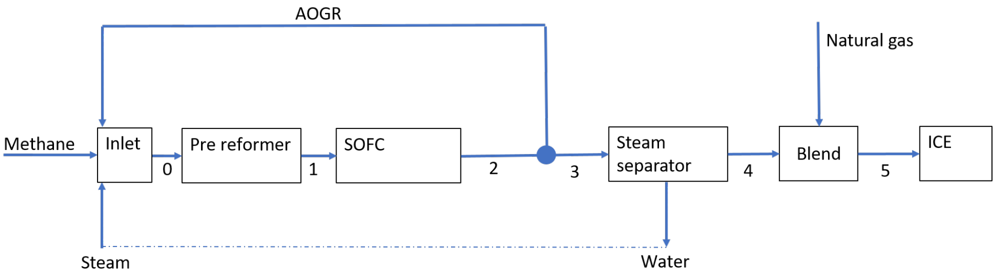

Figure 6.1: Functional scheme of fuel streams in hybrid system

Methane, steam, and optionally recycled AOG are fed to the pre-reformer inlet (stream 0). The pre-reformer model partially reforms the methane and predicts the outlet species composition based on temperature, pressure, oxygen over carbon ratio setting, and methane pre-reforming ratio. The pre-reformer outlet composition is the SOFC inlet composition (stream 1). In the SOFC model, by direct internal reforming reactions and hydrogen oxidation, the inlet fuel stream is (partially) utilized and converted to anode off-gas (stream 2). When AOG recycling is applied, a pre-set recycling ratio splits the AOG stream. One part is going back to the pre-reformer (stream AOGR) and the other part is continuing to the steam separator (stream 3). In the steam separator the water is condensed and removed from the anode off-gas (stream 4). After the steam separator, the dehydrated anode off-gas is blended with natural gas. The resulting AOG-natural gas blend is the fuel introduced to the ICE (stream 5).

6.1.1. Hybrid system model assumptions

Assumptions are made to model the hybrid system:

- This hybrid system study is limited to steady state analysis. The system run-time is set to 1000 seconds, as steady state is certainly achieved in this time. The engine model is steady state only.
- The engine model is based on experiments conducted with hydrogen-natural gas blends. In this study, the effects of other species present in dehydrated anode off-gas are neglected.

- Pressure losses in the pre-reformer, SOFC, steam separator, and heat exchangers are neglected.
- For calculating the system efficiency a fixed BoP parasitic power loss of 5 % of SOFC produced power (AC) is assumed, regardless of which system configuration is used (A or B). The power loss includes: fuel pump, air blower, anode off-gas recycling pump/blower, and water pump.
- The complete system piping is adiabatic i.e. no wall heat losses are taken into account.

6.1.2. Hybrid system model specifications

The SOFC stack geometry and properties are implemented in the hybrid system as modeled in chapter 4. The engine model is implemented as explained in section 5.3. The other SOFC-ICE hybrid system properties and inlet parameter conditions are provided in table 6.1.

Table 6.1: Operating conditions SOFC-ICE hybrid system.

Parameter	Symbol	Value	Unit
Target power SOFC (AC)	$P_{e\ SOFC\ AC}$	375	kWe
Power ICE generator (AC)	$P_{e\ ICE\ AC}$	375	kWe
BoP parasitic power loss	P_{aux}	5	%
SOFC air excess	λ	2 to 14	-
Number of cells in SOFC stack	-	11000	-
Max. temperature gradient SOFC cell	$\Delta T_{cell}/\Delta x$	10	$\mathrm{K\,cm^{-1}}$
Operating pressure SOFC	p_{op}	1.0e5	Pa
Ambient temperature	T_{amb}	300	K
Air inlet temperature SOFC	$T_{air\ in}$	1023	K
Fuel inlet temperature SOFC	$T_{fuel\ in}$	1023	K
Air inlet pressure SOFC	$p_{air\ in}$	1.0e5	Pa
Fuel inlet pressure SOFC	$p_{fuel\ in}$	1.0e5	Pa
Efficiency DC/AC converter	η_{conv}	95	%
Pre-reformer operating temp. config. A	$T_{pre\ ref}$	1023	K
Pre-reformer operating temp. config. B	$T_{pre\ ref}$	773	K
Oxygen over carbon ratio pre-reformer	O/C	2	-
Fuel temperature ICE intake	$T_{ICE\ in}$	300	K
Lower heating value natural gas	LHV_{NG}	3.8361e4	$\mathrm{kJ\,kg^{-1}}$
Lower heating value methane	LHV_{CH_4}	8.0260e2	$\mathrm{kJ\,mol^{-1}}$
Lower heating value hydrogen	LHV_{H_2}	2.418e2	$\mathrm{kJ\,mol^{-1}}$

6.1.3. Performance and controlling parameter equations

Hybrid system electric efficiency is the prime focus of this analysis and is calculated with eq. 6.1.

$$\eta_{HS,LHV} = \frac{P_{e,SOFC,DC} \cdot \eta_{conv} + P_{e,ICE,AC} - P_{aux}}{\dot{N}_{CH_4}^{in} \cdot LHV_{CH_4} + \dot{\phi}_{NG}^{in} \cdot \frac{1}{3600} \cdot LHV_{NG}} \tag{6.1}$$

Where $P_{e\ SOFC\ DC}$ (kWe) is the electric power generated by the SOFC stack (DC). η_{conv} is the DC/AC converter efficiency. $P_{e\ ICE\ AC}$ is the electric power (AC) generated by the ICE-generator. P_{aux} represents the BoP parasitic power losses, which are assumed to be 5% of SOFC produced power (AC). $\dot{N}_{CH_4}^{in}$ is the molar flow rate of methane supplied to the system ($\mathrm{mol\,s^{-1}}$). $\dot{\phi}_{NG}^{in}$ is the volumetric flow rate of natural gas supplied to the system ($\mathrm{m^3\,h^{-1}}$). The molar lower heating value of methane is: LHV_{CH_4} = 8.0260e2 $\mathrm{kJ\,mol^{-1}}$ and the volumetric lower heating value of natural gas is LHV_{NG} = 3.2488e4 $\mathrm{kJ\,m^{-3}}$ (at atmospheric pressure and 300 K).

The SOFC and ICE individual contribution to the hybrid system efficiency are expressed as in eq. 6.2 and 6.3. In eq. 6.3 only anode off-gas bounded hydrogen is taken into account, as the engine model considers only hydrogen from anode off-gas. The anode off-gas bounded carbon monoxide and methane is considered as loss.

$$\eta_{HS,SOFC,LHV} = \frac{P_{e,SOFC,DC} \cdot \eta_{conv} - P_{aux}}{\dot{N}_{CH_4}^{in} \cdot LHV_{CH_4} - \dot{N}_{H2}^{stream\ 3} \cdot LHV_{H_2}} \tag{6.2}$$

$\dot{N}_{H2}^{stream\ 3}$ represents the molar flow rate of H_2 coming from the SOFC anode.

$$\eta_{HS,ICE,LHV} = \frac{P_{e,ICE,AC}}{\dot{\phi}_{NG}^{in} \cdot \frac{1}{3600} \cdot LHV_{NG} + \dot{N}_{H2}^{stream\ 5} \cdot LHV_{H_2}} \tag{6.3}$$

$\dot{N}_{H2}^{stream\ 5}$ represents the molar flow rate of H_2 at the ICE intake (stream 5)[1].

The fraction of power generated by the ICE $f_{HS,ICE}$ is defined in eq. 6.4. The fraction of power generated by the SOFC $f_{HS,SOFC}$ is defined in eq. 6.5.

$$f_{HS,ICE} = \frac{P_{e,ICE}}{P_{HS}} \tag{6.4}$$

$$f_{HS,SOFC} = \frac{P_{e,SOFC,AC} - P_{aux}}{P_{HS}} \tag{6.5}$$

Where the total generated electric power (AC) of the hybrid system P_{HS} is calculated as follows:

$$P_{HS} = P_{e,SOFC,DC} \cdot \eta_{conv} - P_{aux} + P_{e,ICE} \tag{6.6}$$

Fuel utilization, anode off-gas recycling ratio, and methane pre-reforming ratio are operating parameters used in the hybrid system study. The equations of these parameters are given by eq. 6.7, 6.8, and 6.9 respectively.

$$U_f = 1 - \frac{\dot{N}^{stream\ 3} \cdot \left(4x_{CH_4} + x_{H_2} + x_{CO}\right)^{stream\ 3}}{4 \cdot \dot{N}_{CH_4}^{in}} \tag{6.7}$$

$$AOGRR = \frac{\dot{N}^{AOGR}}{\dot{N}^{stream\ 2}} \tag{6.8}$$

$$REF = 1 - \frac{\dot{N}_{CH_4}^{stream\ 0}}{\dot{N}_{CH_4}^{in}} \tag{6.9}$$

6.2. Hybrid system operating parameter sensitivity study

The SOFC-ICE hybrid system configuration is operated with a set of varying operating parameters in order to investigate their influence on system efficiency and performance. The focus in this study is the hybrid system electric efficiency (eq. 6.1), and the generated electric power (AC) (eq. 6.6). Moreover, the individual component efficiencies are demonstrated (eq. 6.2 and 6.3). In section 6.3.1 it is demonstrated that the performance difference between configuration A and B is small, therefore this analysis is using configuration A only. (configuration A: where pre-reformer is integrated with SOFC and is operated at SOFC temperature, or configuration B: where pre-reformer operates at lower temperature and is heated with hybrid system heat integration, see section 6.3).

- Figure 6.2 depicts efficiency against the SOFC current density. The hybrid system and component power generation is depicted in figure 6.3. An increase of the current density, at constant fuel utilization, requires more fuel and generates more SOFC power with a reducing SOFC efficiency and expected fuel cell lifetime. Because the SOFC fuel utilization is fixed, the volumetric flow rate of hydrogen (anode off-gas) before the ICE intake is increased with increasing current density, therefore the ICE efficiency is slightly improved. The ICE power is constant at 375 kWe, thus with increasing SOFC power, the SOFC power fraction is increased and therefore the hybrid system efficiency is increased.

  In table 6.2 the strong negative effect on SOFC efficiency due to the increase in current density is categorized with three minus signs (- - -). The engine efficiency improvement is because of the change in anode off-gas volume flow rate, and the hybrid system efficiency improvement is because of the change in power distribution (due to SOFC power increase with respect to a fixed ICE power), both effects are not assigned to current density and are categorized in the table with a *no*.

---

[1] $\dot{N}_{H2}^{stream\ 3} = \dot{N}_{H2}^{stream\ 5}$

- Figure 6.4 depicts efficiency against fuel utilization. Hybrid system efficiency is decreased with increasing fuel utilization for two reasons: First: the engine efficiency is decreased, because less hydrogen (anode off-gas) is blended with natural gas at the ICE intake. At low hydrogen blending percentages the hydrogen-related performance benefits are vanishing. Second: SOFC efficiency and SOFC power are decreased (figure 6.5) with increased fuel utilization. SOFC power is decreased, because the SOFC operates less effective (lower cell voltage) at high fuel utilization (as explained in section 4.5).

  In table 6.2 the strong negative effect of increase in fuel utilization on SOFC and ICE are categorized with three minus signs (- - -). Also the combined effect on hybrid system efficiency is categorized with three minus signs (- - -).

- Figure 6.6 depicts that SOFC efficiency is increased with incrasing methane pre-reforming ratio (REF). Figure 6.7 depicts generated power versus methane pre-reforming ratio (REF), where the SOFC power generation is increased with increasing REF. As indicated in figure 6.6, an increase of methane pre-reforming ratio has no effects on engine efficiency.

  In table 6.2 the moderate positive SOFC efficiency effect due to an increase in methane pre-reforming ratio is categorized with two plus signs (+ +). Since there are no efficiency effects due to REF on engine and hybrid system efficiency, these effects are labelled a *no*.

- Figure 6.8 depicts efficiency against anode off-gas recycling ratio for a fixed single pass fuel utilization of 81 %. The corresponding hybrid system and component power is depicted in figure 6.9. Usually anode off-gas recycling is applied to reduce the steam demand for pre-reforming, with that an improvement in efficiency is achieved. Because the steam production is done with residual heat in this hybrid system, the SOFC efficiency improvement through anode off-gas recycling is relatively small. Up to an $AOGRR$ of 0.6, there is a small improvement demonstrated (At $AOGRR$ = 0.6, a 0.4 percent point efficiency improvement). A further increase of $AOGRR$ leads to fuel dilution ($O/C > 2$) and reduced SOFC performance and accordingly reduced hybrid system performance.

  Figure 6.10 depicts hybrid system efficiency as a function of fuel utilization and anode off-gas recycling ratio ($AOGRR$) in a contour plot. The highest efficiency (45,9 %) is demonstrated at an $AOGRR$ of 0.6 and a single pass fuel utilization of 76 %.

  In table 6.2 the slightly improved SOFC efficiency due to an increase of $AOGRR$ is categorized with one plus sign (+). Due the re-utilization of anode off-gas through recycling, the amount of anode-off gas for engine combustions is lowered and therefore is engine efficiency slightly reduced and categorized with one minus sign (-). The combined efficiency in the hybrid system is is practically neutral and therefore assigned with a *no*.

Table 6.2 summarizes the effects of operating parameters on component level and hybrid system efficiency. An increase in current density has strong negative effects on SOFC efficiency and has no effects on engine performance (at constant fuel utilization) and hybrid system efficiency. Increase of fuel utilization has strong negative effects on both SOFC and ICE efficiency, and is therefore the most important operating parameter for controlling the hybrid system in order to gain highest efficiency results. Methane pre-reforming ratio is positive affecting SOFC efficiency, there is no resulting effect on ICE efficiency and hybrid system efficiency. Anode off-gas recirculation ratio has small positive effects on SOFC efficiency and negative effects on ICE efficiency, on hybrid system efficiency the total effect is very small and is neglected.

Table 6.2: Summary of effects of operating parameters on component and hybrid system performance. The number of + or - signs is indicating the strength of the effect. The efficiency calculations are expressed in eq. 6.1, 6.2, and 6.3.

Operating parameter (increase)	**Affecting SOFC efficiency** $\eta_{HS,SOFC,LHV}$	**Affecting ICE efficiency**$^{(1)}$ $\eta_{HS,ICE,LHV}$	**Affecting HS efficiency** $\eta_{HS,LHV}$
i	- - -	no	no
U_f	- - -	- - -	- - -
REF	+ +	no	no
$AOGRR$	+	-	no

(1) Due to changes in anode off-gas composition or flow rate.

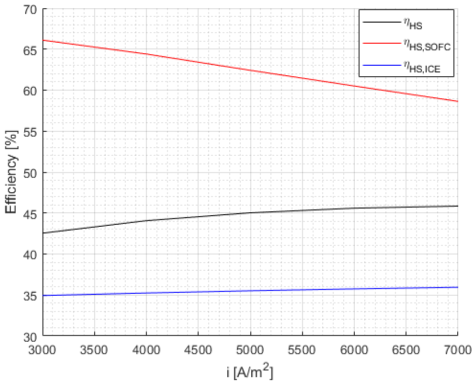

Figure 6.2: Electric efficiency of hybrid system (LHV, AC), SOFC, and ICE against current density. Configuration A, *AOGRR* = 0, fuel utilization = 81 %, *REF* = 0.1.

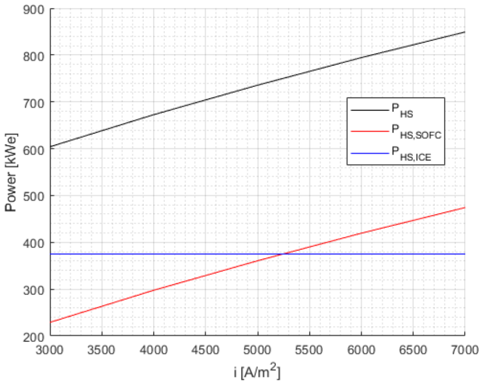

Figure 6.3: Electric power of hybrid system, SOFC, and ICE against current density. Configuration A, *AOGRR* = 0, fuel utilization = 81 %, *REF* = 0.1.

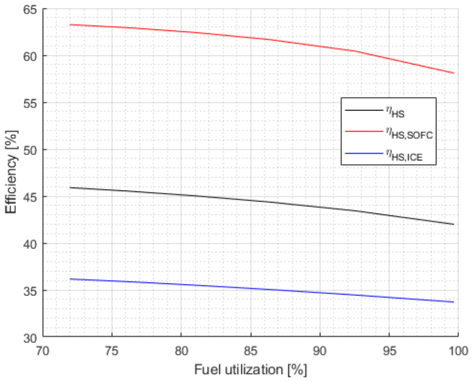

Figure 6.4: Electric efficiency of hybrid system (LHV, AC), SOFC, and ICE against fuel utilization. Configuration A, i = 5000 A m^{-2}, *AOGRR* = 0, *REF* = 0.1.

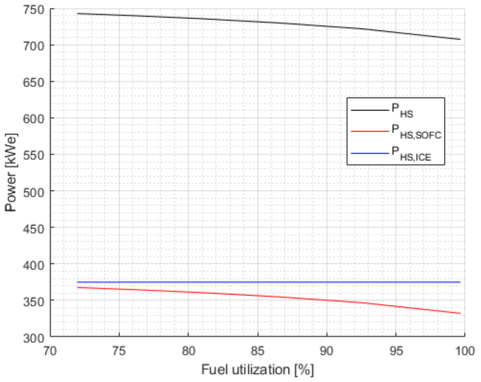

Figure 6.5: Electric power of hybrid system, SOFC, and ICE against fuel utilization. Configuration A, i = 5000 A m^{-2}, *AOGRR* = 0, *REF* = 0.1.

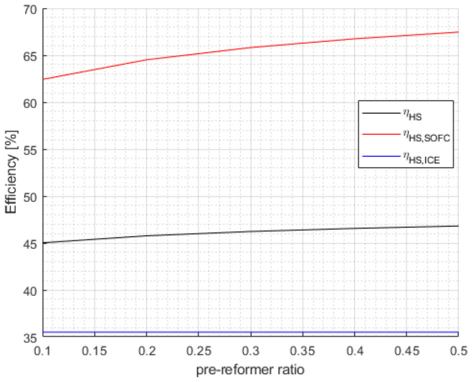

Figure 6.6: Electric efficiency of hybrid system (LHV, AC), SOFC, and ICE against CH_4 pre-reforming ratio. Configuration A, i = 5000 A m^{-2}, *AOGRR* = 0, fuel utilization = 81 %.

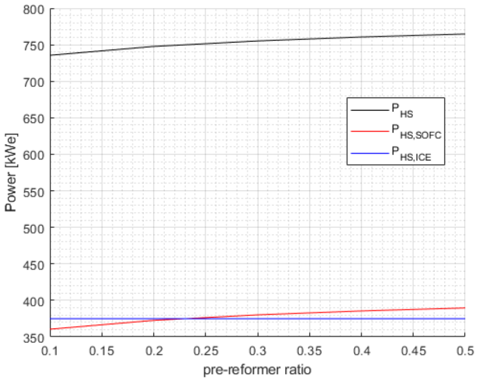

Figure 6.7: Electric power of hybrid system, SOFC, and ICE against CH_4 pre-reforming ratio. Configuration A, i = 5000 A m^{-2}, *AOGRR* = 0, fuel utilization = 81 %.

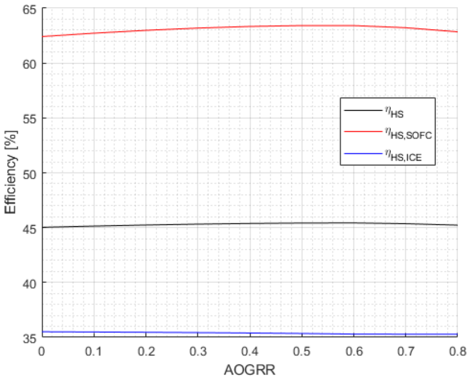

Figure 6.8: Electric efficiency of hybrid system (LHV, AC), SOFC, and ICE against anode off-gas recycling ratio. Configuration A, $i = 5000\,\mathrm{A\,m^{-2}}$, fuel utilization (single pass) = 81 %.

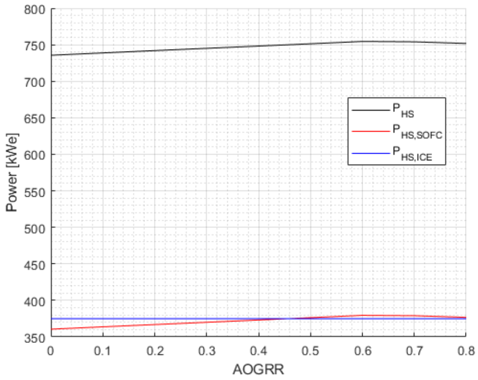

Figure 6.9: Electric power of hybrid system, SOFC, and ICE against anode off-gas recycling ratio. Configuration A, $i = 5000\,\mathrm{A\,m^{-2}}$, fuel utilization (single pass) = 81 %.

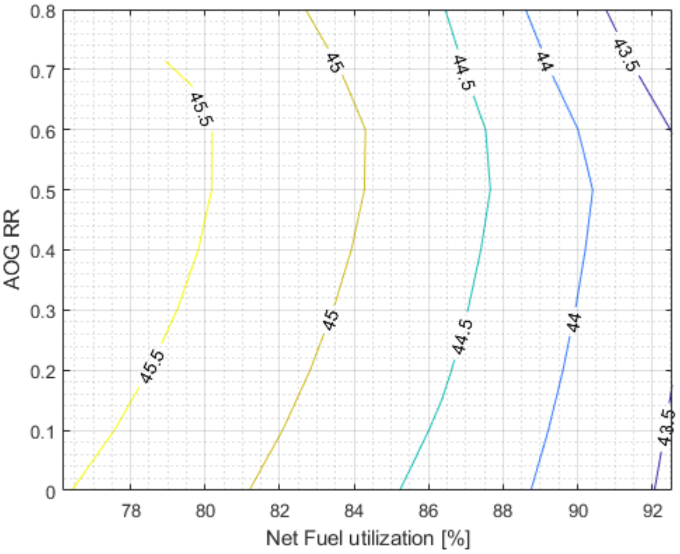

Figure 6.10: Contour plot of hybrid system electric efficiency (%, LHV, AC) in function of net fuel utilization and $AOGRR$. Configuration A, $i = 5000\,\mathrm{A\,m^{-2}}$, $REF = 0.1$.

6.2.1. AOG stream analysis

Figure 6.11 depicts hybrid system performance for varying fuel utilization and a selected set of operating parameters: i = 5000 $\mathrm{A\,m^{-2}}$, $AOGRR$=0, and REF=0.3. The highest hybrid system efficiency (46.9 %) is demonstrated at a fuel utilization of 72 %.

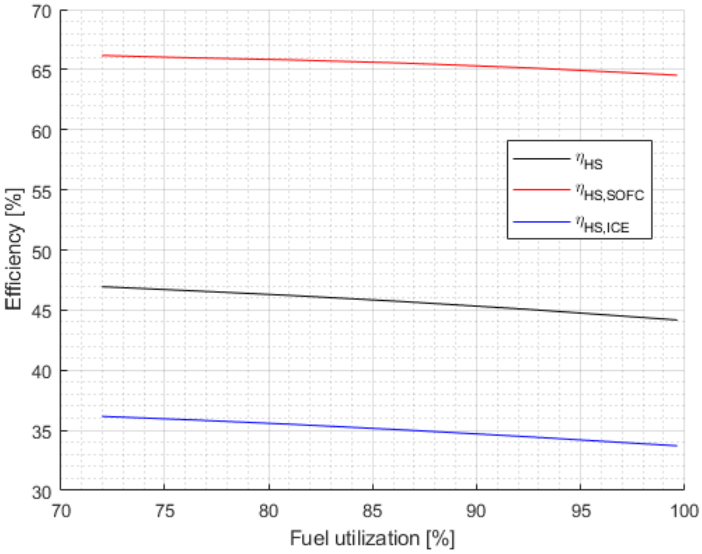

Figure 6.11: Hybrid system electric efficiency (LHV, AC) against fuel utilization. Configuration A, i = 5000 $\mathrm{A\,m^{-2}}$, $AOGRR$=0, REF=0.3.

Fuel utilization is directly affecting fuel composition at ICE intake. Figure 6.12 depicts the relative AOG composition at the SOFC-anode outlet (stream 2) for varying fuel utilization. Figure 6.13 depicts the relative composition of stream 5, and figure 6.14 depicts volumetric flow rates of stream 5. As explained in chapter 5, the engine model is substantiated with experiments up to a hydrogen blending percentages of 20 %. If the hydrogen to natural gas ratio is further increased, the uncertainty of the engine model is increased. As depicted in figure 6.15, the hydrogen blend percentage can easily exceed this 20 % limit. With a maximum hydrogen blend percentage kept in the order of 20 %, a parameter set is selected which provides a corresponding hybrid system efficiency of 45.7 % (at a fuel utilization of 86 %). Table 6.3 provides operational results belonging to the selected set of operating parameters.

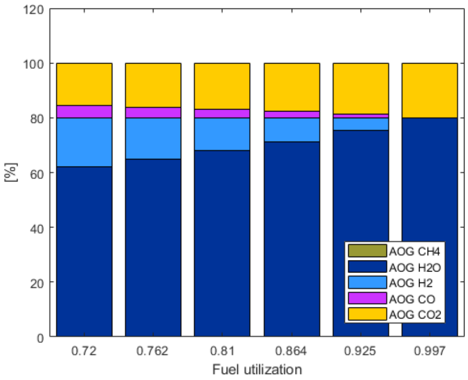

Figure 6.12: AOG composition at SOFC outlet (stream 2). Configuration A, i = 5000 $\mathrm{A\,m^{-2}}$, $AOGRR$=0, REF=0.3.

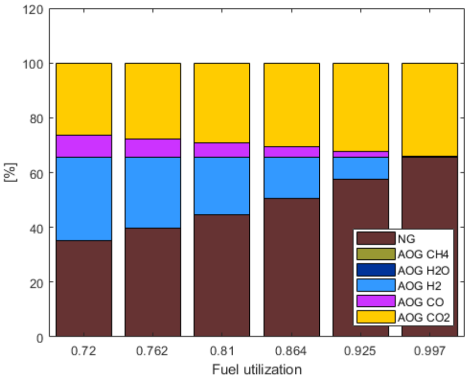

Figure 6.13: Composition fuel at ICE intake (stream 5). Configuration A, i = 5000 $\mathrm{A\,m^{-2}}$, $AOGRR$=0, REF=0.3.

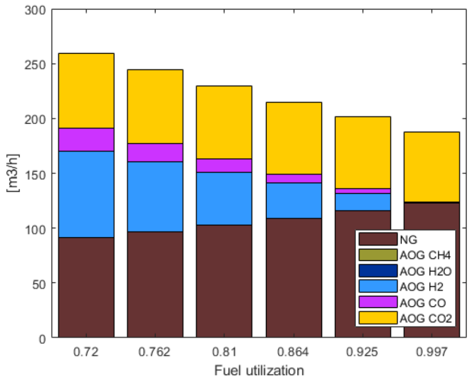

Figure 6.14: Volume flow rate per constituent at ICE intake (stream5). Configuration A, i = 5000 $\mathrm{A\,m^{-2}}$, $AOGRR$=0, REF=0.3.

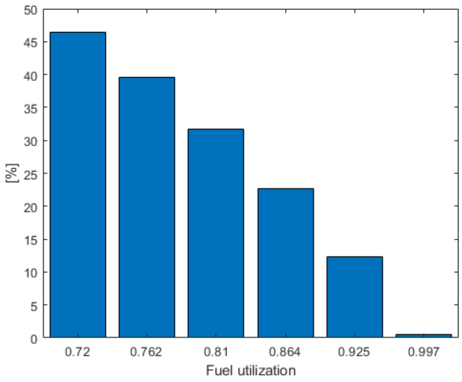

Figure 6.15: Hydrogen to hydrogen-and-natural gas ratio (hydrogen-blend-percentage (HNG)) (stream5). Configuration A, i = 5000 $\mathrm{A\,m^{-2}}$, $AOGRR$=0, REF=0.3.

Table 6.3: Selected hybrid system operating parameters and performance.

Parameter	**Value**	**Unit**
i	5000	$\mathrm{A\,m^{-2}}$
U_f	86	%
$AOGRR$	0	%
REF	0.3	%
$f_{P_{e,ICE}}$ / $f_{P_{e,SOFC}}$	50 / 50	%
% H_2	22.7	%
Performance	**Value**	**Unit**
$P_{e,HS,AC}$	752.4	kW
$\eta_{HS,LHV}$	45.7	%
$\eta_{HS,SOFC,LHV}$	65.5	%
$\eta_{HS,ICE,LHV}$	35.0	%

6.3. Hybrid system heat integration

Adequate heat integration of components and mutual streams is a necessary condition to achieve the proposed efficiency advantages, because no additional energy is required to heat up streams or maintain chemical reactions. In this work a pinch analysis is carried out to determine if there is enough heat capacity available within the system to maintain stream temperatures as required and to produce the steam for methane pre-reforming. Modeling and optimizing the heat exchanger network falls outside the scope of this work. Two proposed designs component for integration are considered:

- Configuration A is depicted in figure 6.16: the pre-reformer is part of the integrated stack module (ISM). The reaction heat required for the (endothermic) methane steam reforming reaction is withdrawn from the SOFC-stack (IIR). The pre-reformer operation temperature is the same as SOFC inlet temperature.
- Configuration B is depicted in figure 6.17: the pre-reformer is a stand-alone component, operating at 500 °C. The heat required for the (endothermic) methane steam reforming reaction is withdrawn from residual heat streams in the hybrid system.

A functional explanation of the heat exchangers is listed below.

- HEX 1, configuration B only: The pre-reformed methane is further pre-heated before it is introduced to the SOFC anode channel. Pre-heating is done by heat exchange between this fuel stream and the SOFC anode off-gas stream.
- Pre-heater for air (HEX 2): Air is pre-heated before it is introduced to the SOFC cathode channel. Pre-heating is done by heat exchange between fresh air and SOFC stack exhausted air. The inlet air

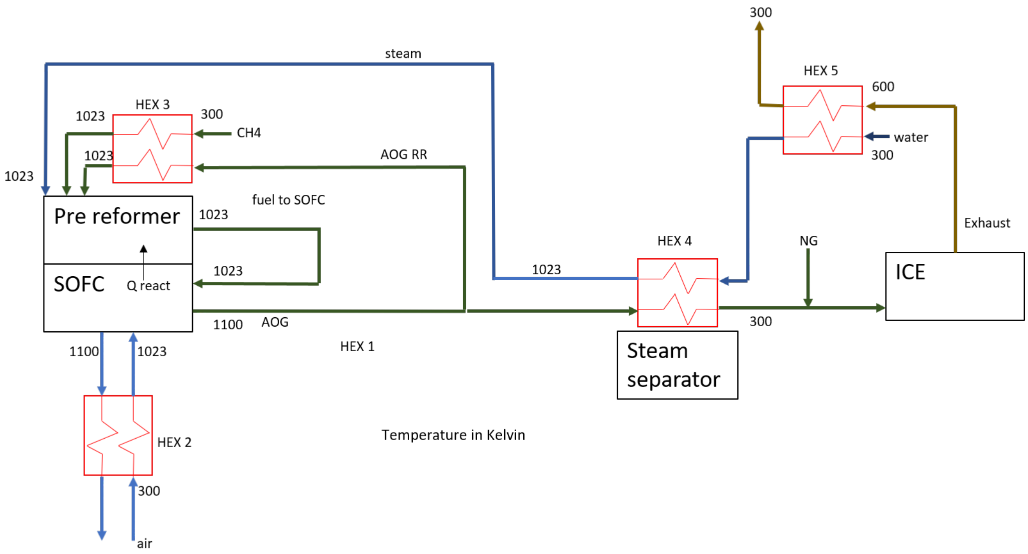

Figure 6.16: Proposed hybrid system heat integration, configuration A.

temperature is fixed, but the volume flow rate of this stream has a role as coolant to remove heat generated in the SOFC stack. In present work the SOFC stack temperature is managed by adapting the air excess ratio. The initial air excess ratio is 2 and will be increased if the temperature difference between stack input and output approaches this maximum value. The maximum temperature difference between cell inlet and outlet is determined to be 100 K[2].

- Pre-heater for fuel (HEX 3): Methane is pre-heated up to pre-reformer operating temperature to maintain the reforming reactions. In the proposed hybrid system this is done by a heat exchange places between the methane and AOGR stream.

- Steam generator (HEX 4 and 5): (Extra) steam is required to reform methane, this steam is produced in heat exchanger 4 and 5. Water is supplied at 300 K (rest product of the steam separator) and is heated, vaporized and further heated up to reach pre-reformer temperature. Heat exchanger 4 is basically a combination of a steam generating (evaporator) and a heating part. Heat exchanger 4 is heated by the hot exhaust stream coming from the SOFC and the steam condensing process. The heat exchanged in heat exchanger 5 is obtained from the ICE exhaust gas stream.

6.3.1. Configuration A and B and fuel utilization

Figure 6.18 depicts efficiency against fuel utilization for configuration A and B. The marginal difference is due to the different pre-reforming temperature, which has a small effect on the species composition of stream 1. For both systems the steady state SOFC temperature is comparable and therefore has no distinctive effect on steady state cell performance. The temperature of both systems is comparable because it is controlled by adapting the excess air supply to the stack. In practice the amount of excess air which has to be blown into the system is influencing system efficiency, but in this work varying blower power is not taken into account.

6.3.2. Pinch analysis

Figure 6.19 presents the results of the pinch analysis for the selected parameter settings. The available heat capacity (supply) and required heat capacity (target) in the hybrid system streams are represented as a function of temperature (K) against heat load (kW). The heat capacity rate of all the streams is combined in two composite curves, one for all hot streams (red curve) and one for all cold streams (blue curve). The point of closest approach between the hot and cold composite curves is the pinch point, and gives a hot stream pinch temperature and a cold stream pinch temperature. At this pinch point the heat integration is most critical. By starting the heat integration at this point, the energy requirements can be achieved using heat exchangers to recover heat between hot and cold streams in two separate systems, one for temperatures above pinch

---

[2] Maximum temperature gradient is 10 $\mathrm{K\,cm^{-1}}$ [71]

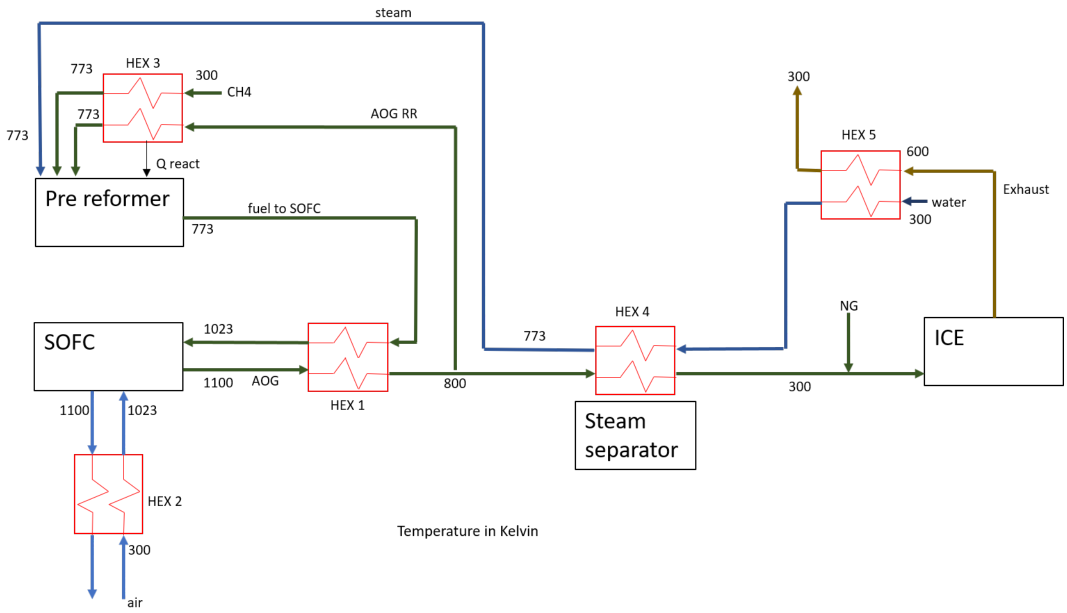

Figure 6.17: Proposed hybrid system heat integration, configuration B.

temperatures and one for temperatures below pinch temperatures. The amount of heat externally added (required) in the hot system is the hot utility, and any residual heat in the cold system is the cold utility. As indicated in figure 6.19, adequate heat integration for this system, with selected operating parameters, is possible without external heating capacity demand (hot utility = 0 kW).

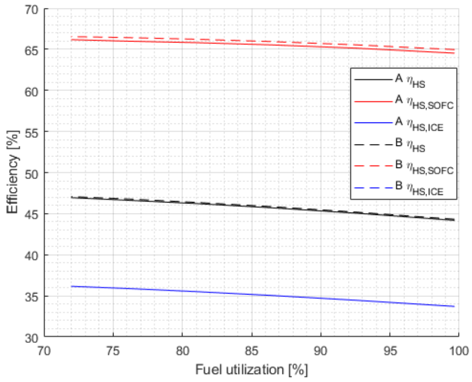

Figure 6.18: Electric efficiency against fuel utilization for configuration A (solid lines) and configuration B (dashed lines), $i = 5000\,\mathrm{A\,m^{-2}}$, $AOGRR$=0, REF=0.3.

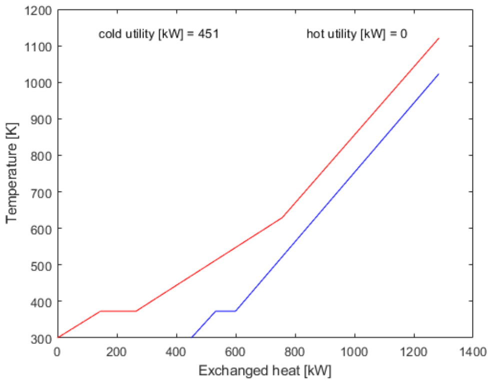

Figure 6.19: Pinch analysis composite curves for selected system parameters. Red curve = hot stream = supply, blue = cold stream = target. Configuration A, $i = 5000\,\mathrm{A\,m^{-2}}$, $AOGRR$=0, fuel utilization = 86 %, REF=0.3.

6.4. Power split study

In order to study the effects of different power splits between SOFC and ICE on hybrid system performance, the power generation capacity of the SOFC is varied by changing the number of SOFC cells, while the power generation of the ICE is kept constant at 375 kWe. Because engine performance is substantiated with experiments up to a hydrogen blending percentages of 20 %, during this study a hydrogen blending percentage in the order of 20 % is the limit. The power fraction distribution as shown in table 6.4 is simulated by the hybrid system model.

The results of this power split study are provided in table 6.5 and figure 6.20 depicts a trend-line for hybrid system efficiency versus SOFC power fraction. A small SOFC power fraction means a lower anode off-gas flow

Table 6.4: Power fraction for power split study, hybrid system power distribution.

Fraction [%]	**target** $P_{e,SOFC,AC}$ [kW]	$P_{e,ICE,AC}$ [kW]	**target** $P_{e,HS,AC}$ [kW]	**number of cells SOFC**
$f_{HS,SOFC}$ = 25 %, $f_{HS,ICE}$ = 75 %	125	375	500	3667
$f_{HS,SOFC}$ = 33 %, $f_{HS,ICE}$ = 67 %	187	375	562	5500
$f_{HS,SOFC}$ = 50 %, $f_{HS,ICE}$ = 50 %	375	375	750	11000
$f_{HS,SOFC}$ = 67 %, $f_{HS,ICE}$ = 33 %	750	375	1125	22000

rate, and hence a lower amount of hydrogen available for blending with natural gas at ICE intake. In that case, in order to increase the amount of hydrogen available for blending with natural gas (up to ≈ 20 %), the SOFC fuel utilization is lowered. A lower fuel utilization improves hybrid system efficiency. In the case of a larger SOFC power fraction, the SOFC fuel utilization is increased in order to keep the hydrogen blending percentage in the order of 20 %. For the case [67 % SOFC- 33 % ICE] the fuel utilization is increased up to 92 %.

In consideration of the ICE model limitations, further enlargement of the SOFC power fraction means that not all left-over fuel can be utilized in the engine, causing the combined efficiency benefits of the hybrid system are cancelled. Based on the here-presented results it can be concluded that efficiency improvements can be obtained by enlarging the SOFC power fraction, however to further optimize these improvement, the engine model should be improved for better analysis.

Table 6.5: Power split study. Selected hybrid system operating parameters and performance, varying power fraction (f SOFC %- / ICE %). The fuel utilization of the SOFC is set, such that the hydrogen blend percentage at ICE intake is in the order of 20 %.

Parameter	$f_{HS,SOFC}$ **= 25 %,** $f_{HS,ICE}$ **= 75 %**	$f_{HS,SOFC}$ **= 33 %,** $f_{HS,ICE}$ **= 67 %**	$f_{HS,SOFC}$ **= 50 %,** $f_{HS,ICE}$ **= 50 %**	$f_{HS,SOFC}$ **= 67 %,** $f_{HS,ICE}$ **= 33 %**	**Unit**
i	5000	5000	5000	5000	$\mathrm{A\,m^{-2}}$
U_f	72	76	86	92	%
$AOGRR$	0	0	0	0	%
% H_2	19.4	22.5	22.7	23.1	%
Performance					**Unit**
actual $P_{e,HS,AC}$	499	566	752	1123	kW
$\eta_{HS,LHV}{}^{(1)}$	38.2	41.6	45.7	50.7	%
$\eta_{HS,SOFC,LHV}{}^{(2)}$	64.4	65.3	65.5	65.2	%
$\eta_{HS,ICE,LHV}{}^{(3)}$	33.7	35.0	35.0	35.1	%

(1) Hybrid system efficiency, see eq. 6.1.
(2) SOFC net efficiency, see eq. 6.2.
(3) ICE efficiency, eq. 6.3.

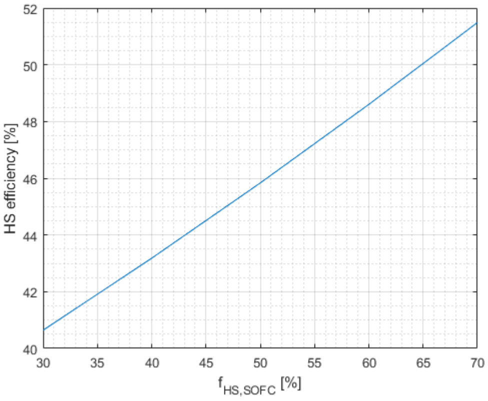

Figure 6.20: Hybrid system efficiency versus SOFC power fraction. The fuel utilization of the SOFC is set, such that the hydrogen blend percentage at ICE intake is in the order of 20 %.

6.5. Marine power plant comparison

The volume and weight of power plants are critical design criteria for any transport application. A certain amount of power and endurance is required, while volume and weight are commonly restricted for practical reasons. Energy and power density are definitions to express these criteria. Energy density is expressed as the amount of energy available per unit of either mass or volume. Power density is expressed as the amount energy conversion per unit of either mass or volume. In this section a comparison is made between a diesel engine generator set, a natural gas engine generator set, a standalone SOFC, and the proposed SOFC-ICE hybrid system. The comparison is made regarding efficiency, gravimetric and volumetric power density and gravimetric and volumetric energy density of the fuel.

Table 6.6 and 6.7 provide the results. Considering volumetric density, which is commonly the critical parameter in modern shipping, the SOFC standalone system needs three times more space, and the SOFC-ICE hybrid system needs two times more space compared to conventional diesel or gas engines power plants. Considering energy density of fuel, and taking the power plant conversion efficiency into account, the LNG storage volume for proposed hybrid system is two times larger than that of a diesel fuelled generator set.

This comparison is done for a 750 kWe system. Most of the data provided in table 6.6 and 6.7 is taken from a review study carried out by van Biert et al. [60]. The SOFC parameter values are based on the Bloomenergy 'Energy Server 5' module (300 kWe) [69].

Table 6.6: Indicated efficiency and power density for marine power plants. Power range is 750 kWe.

Parameter	**ICE gen.set (Diesel)**	**ICE gen.set (LNG)$^{(1)}$**	**SOFC stand-alone (LNG)$^{(1)}$**	**SOFC-ICE hybrid (LNG)$^{(1)}$**	**Unit**
η_{LHV}	36$^{(3)}$	34$^{(4)}$	55$^{(4)}$	45$^{(3)}$	%
Gravimetric power density	45$^{(3)}$	45$^{(3)}$	19$^{(2)}$	27$^{(5)}$	$\mathrm{W kg^{-1}}$
Volumetric power density	32.5$^{(3)}$	30$^{(3)}$	9.5 $^{(2)}$	14.5$^{(5)}$	$\mathrm{W L^{-1}}$

(1) LNG stored at -162 °C

(2) Based on Bloomenergy 'Energy Server 5' (300 kWe) [69].

(3) Ref. [60], [1].

(4) Based on the engine used in present work (CAT-G3508).

(5) Weighted average, calculated using stand-alone specifications.

Table 6.7: Indicated energy density for Diesel and LNG.

Parameter	**Marine Diesel**	**LNG** (1)	**Unit**
Fuel gravimetric energy density (2)	8.3	7.4	$\mathrm{kWh\,kg^{-1}}$
Fuel volumetric energy density (2)	8.2	3.3	$\mathrm{kWh\,L^{-1}}$

(1) LNG stored at -162 °C
(2) Fuel energy density (LHV), including the storage system [60]

6.6. Discussion

The SOFC and ICE component models are combined in a hybrid system model. The sensitivity of operating parameters on hybrid system performance is investigated. The operating parameters investigated are: current density, fuel utilization, pre-reforming ratio, and anode off-gas recycling ratio. The prime focus of this study is hybrid system efficiency. It is found that fuel utilization is strongly effecting hybrid system efficiency and is therefore the most important operating parameter to control.

With hybrid system efficiency as prime focus, a set of operating parameters is selected for further analysis. A study of system's stream compositions and flow rates is conducted with hydrogen blending percentage at ICE intake as critical criterion, because hydrogen percentages larger than 20 % are not substantiated with engine experiments. With this limit in mind, a final parameter set is selected for a heat integration analysis and power-split study. Also a comparison between developed hybrid system and conventional marine power plants is carried out, which is concentrated on power and energy density.

Operating the hybrid system at 5000 $\mathrm{A\,m^{-2}}$ with 30 % pre-reformed methane, and no anode off-gas recycling resulted in an electric efficiency of 46.9 % at an SOFC fuel utilization of 72 %. The hydrogen blending percentage for this setting is ≈ 45 %. To use a by experiments substantiated engine performance (confirmed with experimental data, in the order of 20 % hydrogen blend percentage), the fuel utilization is increased to 86 % , which resulted in a hydrogen blending percentage of 22.3 %. In this latter case, the hybrid system electric efficiency demonstrated is 45.7 %. Since this latter achievement is based on a reasonable fuel utilization (86 %) and the engine results are substantiated with an experimental data set, this operating parameter set is selected as a benchmark for further system comparisons in this work.

Summarizing: a 750kWe net electric power (AC) is generated with an electric efficiency of 45.7 % and a power fraction of $f_{HS,SOFC}$ = 50 % and $f_{HS,ICE}$ = 50 %. This performance is a 5 to 10 percent point improvement compared to conventional diesel engines operating in this power range (see ref. [1] and figure 6.21).

The achieved SOFC-ICE hybrid system efficiency is low compared to demonstrated efficiencies in literature (Park et al.[7]: 59.5 %, van Biert et al. [13]: 64 %, and Chuahy et al. [14]: 70.9 %). The reason for this is the design of the system. In this work the ICE is operated as a combined cycle after the SOFC with an ICE power fraction of $f_{HS,ICE}$ = 50 %, which is a much higher compared to literature: Park et al. [7]: $f_{HS,ICE}$ = 12.7 %, van Biert et al. [13]: 5 %, and Chuahy et al. [14]: 14.7 %. Combined cycle operation, with a substantial $f_{HS,ICE}$ is expected to make the system more capable in dynamic load following and improves system's redundancy, but, as demonstrated, it is at the expense of hybrid system efficiency. In this work, a power-split sensitivity study demonstrated an electric efficiency of 50.7% when operating the developed hybrid system with a power split of $f_{HS,SOFC}$ = 67 % and $f_{HS,ICE}$ = 33 %. This looks attractive, but operating this power fraction requires an SOFC fuel utilization of 92 % in order to keep the hydrogen blend percentage at the ICE fuel intake in the order of 20 %. This latter 20 % is due to the engine model limitations. In future work, higher efficiencies can be achieved with increasing SOFC power fractions, if the hydrogen addition percentage at ICE intake is allowed to expand. Because a fuel utili 50 % power split is used as a benchmark for further comparisons.

A volumetric power density analysis indicated that the SOFC-ICE hybrid system installation volume is more than twice as large as conventional marine power plants. Looking into volumetric energy density of the used fuels, and taking the energy conversion efficiency into account, the LNG storage space for proposed hybrid system is two times larger than that of a diesel fuelled ICE generator set. A 50 % SOFC and 50 % ICE power split leads to these numbers, depending on the operating profile a different power split can lead to other efficiencies and volume and weight constraints. The impact of these power and energy density constraints depend on the practical application (e.g. ship design, required power, endurance, operating profile, and costs) and must be considered case-by-case.

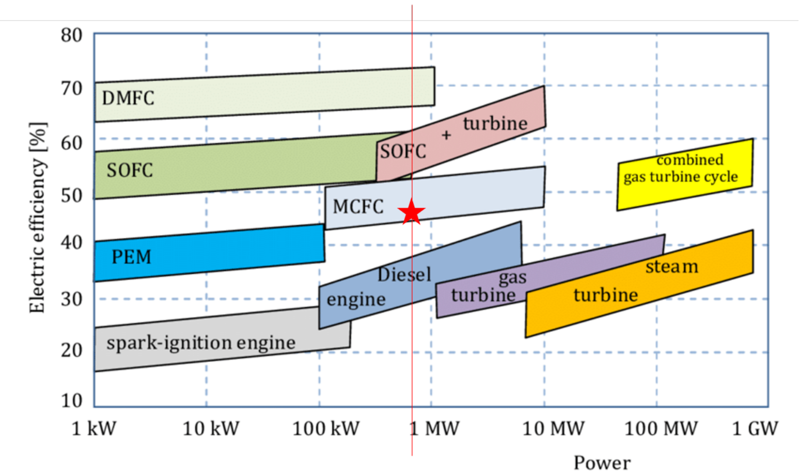

Figure 6.21: Electric efficiency (LHV) for power plants. The red line indicates the 750 kWe. The red start indicates the position of the here-developed SOFC-ICE hybrid system. Original figure taken from [79].

6.7. Conclusion

A SOFC-ICE hybrid system operating parameter sensitivity study and a system power split study are carried out. The following conclusions are drawn:

- The operating parameter fuel utilization has a strong combined effect on SOFC, ICE, and hybrid system efficiency, hence fuel utilizations is assigned to be the most important operator parameter to control.
- A 67 % SOFC power fraction and 33 % ICE power fraction operation have demonstrated a hybrid system electric efficiency of 50.7 %. However, in this model the SOFC should be operated at a fuel utilization of 92 % in order to keep the hydrogen blend percentage at the engine fuel intake in the order of 20 %.
- To keep SOFC fuel utilization within reasonable limits, and in order to operate the engine model within model limitations, a power split of 50 % SOFC and 50 % ICE power is selected as benchmark case.
- Operating the hybrid system with a 50 % SOFC power fraction and 50 % ICE power fraction and a SOFC fuel utilization of 86 % has demonstrated a hybrid system electric efficiency of 45.7 % at 750 kWe.

7

Conclusions and recommendations

This study was a first step in identifying relevant operating parameters and system configurations of SOFC-ICE hybrid systems for marine applications and finding their influence on system efficiency and performance. A literature study was carried out, thereafter system component models were developed and combined in to a hybrid system model. The hybrid system model was studied and has led to a number of conclusions and recommendations.

7.1. Conclusions

7.1.1. SOFC model

An SOFC stack with pre-reformer and anode off-gas recycling was modeled and was able to operate as a standalone model or as a component in a combined model. The model was developed in such a way that either the dynamic performance can be predicted or the steady state results can be used in the hybrid system study. The SOFC model was validated with a well-documented model in literature [26]. It was found that the here-developed model was slightly overestimating the steady state performance compared to the reference model, the dynamic behaviour of the model was comparable. The deviation between this model and the reference model was explained by the difference in modeling approach: a 0-D lumped parameter model versus a 1-D distributed parameter model. The 0-D model is computationally fast, but it demonstrated that an experimental data set is required for calibration if higher accuracy is needed. For this study the deviation with the reference model was accepted.

A parameter sensitivity analysis was performed with the SOFC component model operating as a standalone system. The dependency of cell voltage and temperature to various operating parameters was investigated. With this study the simulation possibilities of the SOFC model were demonstrated and the following conclusions were drawn: operating low current density results in high cell voltage and high efficiency. This is favourable at SOFC part-load operation. High fuel utilization results in high SOFC standalone efficiency and higher temperatures, but cell voltage decreases with increasing fuel utilization and so does the net efficiency. Air excess ratio is an important parameter to optimize SOFC temperature to obtain maximum cell voltage within the thermal stress limits. The modeled air excess controller kept the SOFC cell temperature gradients within the limits. Increasing amount of methane pre-reforming has a positive effect on cell voltage, the corresponding temperature development depends on the method of pre-reformer heat integration and can be regulated by controlling the air excess ratio. Finally, the effects of anode off-gas recycling were studied. It was shown that anode off-gas recycling positively affects cell voltage while keeping the single pass fuel utilization low. The evaluated SOFC operating parameters were expected to have influence on hybrid system performance also.

7.1.2. ICE model

A mean value first principle (MVFP) engine model was developed which relied on measured engine data for calibration. This measured engine data was obtained form a previous TU Delft study carried out by Sapra et al. [20]. The MVFP engine model provided insights on engine performance when hydrogen and natural gas are aspirated into the engine. The following conclusions were drawn: 20 % hydrogen addition to natural gas improved engine efficiency with 1.5 percent point (at 375 kWe, 1500 rpm, $NO_x = 500$ mg/nm^3

(at 5 % oxygen)), and hydrogen addition reduced combustion duration and cycle-to-cycle variations, which improved combustion stability. From these results, it was concluded that combined operation of an internal combustion engine with an SOFC is beneficial, because engine performance is improved due to the addition of a hydrogen-rich gas to the regular natural gas fuel intake.

7.1.3. SOFC-ICE hybrid system model

In this work a SOFC-ICE hybrid system model was developed including a pre-reformer, anode off-gas recycling facility, and steam separator (water vapour condenser). A target power demand of 750 kWe was set with an initial power split of 50 %-ICE and 50 %-SOFC. The SOFC-ICE hybrid system performance was analysed by means of a study to the sensitivity of the following parameters: current density, fuel utilization, methane pre-reforming ratio, and anode off-gas recycling ratio. It was found that fuel utilization is strongly affecting hybrid system performance and is therefore the most important operating parameter in order to obtain best hybrid system efficiency.

With a selected operating parameter set and a fuel utilizations of 72 %, it was demonstrated that a 375 kWe (AC) SOFC and 375 kWe ICE hybrid system was able to operate with an electric efficiency of 46.9 % (LHV). To achieve this efficiency result, the engine was operated with a hydrogen to natural gas percentage of 45 %. The engine model was experimentally substantiated up to a 20 % hydrogen to natural gas percentage. By respecting this engine model limit, through operating an SOFC fuel utilization of 86 %, a hydrogen blend percentage in the order of this limit was managed and an electric efficiency of 45.7 % (LHV) was achieved. This latter efficiency, and the selected operating parameters, were used as a benchmark for further analysis.

The electric efficiency of 45.7 % is a 5 to 10 percent point improvement compared to conventional diesel driven power plants operating in a similar power range [1]. For the selected operating parameter set, by means of a heat integration study, it was demonstrated that the system outlet streams contain sufficient heat capacity to produce the required pre-reformer steam and to heat-up ingoing fuel and air streams.

Furthermore, a study to the effects of SOFC and ICE power fractions on system efficiency was carried out. An electric efficiency of 50.6 % was achieved, operating a 67 % SOFC - 33 % ICE power fraction. It was concluded that hybrid system efficiency can be improved when the SOFC power fraction exceeds the ICE power fraction. This looks attractive, but operating this power fraction requires an SOFC fuel utilization of 92 % in order to keep the hydrogen blend percentage at the ICE fuel intake in the order of 20 %. Higher efficiencies can be achieved if the hydrogen blend percentage at ICE intake is allowed to expand. In this work a 50 % power split is used for further analysis, because this power split in combination with a 86 % fuel utilisation, is a realistic and reliable setting, particularly because of the used engine model and its model limitations.

A power density comparison was made with conventional marine power plant systems. The SOFC-ICE hybrid system installation volume is more than twice as large as conventional marine power plants. Taking the energy conversion efficiency into account: the natural gas storage space is two times larger than that of a diesel fuelled ICE generator set. A 50 % SOFC and 50 % ICE power split leads to these numbers, depending on the operating profile a different power split can lead to other efficiencies and volume and weight constraints. The impact of these constraints depend on the practical application (e.g. ship design, required power, endurance, operating profile, and costs) and must be considered case-by-case.

7.2. Recommendations

The developed models are considered to form a basis for future research on SOFC-ICE hybrid systems for marine applications. Several recommendations are made for future work on this topic:

- Concerning the SOFC-ICE hybrid system:
  - This study was considering only steady state operation. A study to dynamical operations should be the next step to investigate possibilities for future applications in shipping. The key for efficient operation over the full dynamic power range is to control the flows to and between SOFC and ICE. The flows of air and fuel in each component will determine the fuel utilization (efficiency), power split, quality of combustion, protection against thermal-mechanical failure, and emissions of the complete hybrid system. In order to develop a hybrid system control system: First a specific marine application operational profile and dynamical load profile should be selected as a benchmark. Then, to optimize system's performance when following these profiles, the hybrid system design (configuration and power split) and a system control strategy should be developed. The prime controller in this control system design should be fuel utilization.

  - In this study the balance of plant losses are assumed to be 5 % of generated SOFC power (AC). For accurate prediction of net hybrid system efficiency, the individual balance of plant system components should be modeled such that their power losses are predicted based on operating conditions (e.g. air blower power consumption depending on air excess ratio).
  - A combined SOFC-ICE hybrid system can have the potential to meet marine power plant reliability and safety requirements. However a dedicated study to these subjects is necessary to argue this case.
  - This study has not investigated the economical impact of SOFC-ICE hybrid system operation. In future work the capital costs and costs of operation must be calculated and compared to other power plant systems. This study should also take into account the logistic availability of LNG with respect to the operational profile.

- Concerning the SOFC component model:
  - The performance of the here-developed 0-D SOFC model is compared with a 1-D model from literature. Fur this study the 0-D model fulfils its requirements. If the 0-D model is required in more detailed studies, a calibration with experiments is recommended. The 0-D model is developed by implementing basic physical principles (first principles), the calibration of the model can be done accurately and focused at the specific physical principle.

- Concerning the ICE model three recommendations are made:
  - The load of the engine is a fixed value. In future studies to dynamical system operation, the engine's part-load performance is required. The engine model should be improved such that it can compute dynamic engine performance based on varying AOG-fuel blends.
  - The experimental data set which is used for the calibration of the here-developed engine model is describing engine results for hydrogen blending percentages from 0 % to 20 %. Engine model results for hydrogen blending percentages larger than 20 % are based on extrapolated data. Operating at low fuel utilization increases hybrid system efficiency and increases hydrogen amount at ICE intake, therefore it is recommended to expand the ICE experimental data sets by engine measurements at larger hydrogen blending percentages.
  - The developed ICE model is only considering hydrogen-natural gas blends. The effects of CO and CO_2 on engine performance are not taken into account. Future SOFC-ICE hybrid system studies should take these effects into account also.

- Other effects which deserve further attention:
  - Alternating pressures at the ICE intake due the reciprocating principle of the ICE can be pushed backwards to the SOFC, through the anode-off gas line. If this effect is present, it can be harmful to the fragile SOFC structure. A fuel buffer capacity is might be required to dampen these cyclic effects. ICE models or experiments should indicate the severity of this phenomenon.
  - In this work it was investigated if the heat capacity in the hybrid system was sufficient for maintaining required stream temperatures. In future studies the heat exchangers and their network should be modeled to investigate the influence on system's dynamic performance.
  - CO_2 reduction is achieved by the increasing system efficiency. Exact numbers of emission reductions of NO_x and SO_x are not calculated. Future model enhancements should consider emission calculations.

A

SOFC electrochemistry

This appendix describes fundamental fuel cell electrochemistry theory.

A.1. Nernst voltage

At constant pressure and temperature, the maximum amount of work that can be obtained from a chemical system is equal to the change of Gibbs free energy [80].

$$\Delta G = G_{products} - G_{reactants} \tag{A.1}$$

$$\Delta G = W \tag{A.2}$$

If there are no losses in the fuel cell (reversible process) all the Gibbs free energy is converted into electrical energy. This principle is used to find the reversible open-circuit voltage (E) of a fuel cell (eq. A.4).

$$W_{elec} = \Delta G = \pm VI = -nFE \tag{A.3}$$

$$E = \frac{-\Delta G}{nF} \tag{A.4}$$

Where $F = 96485\,\mathrm{C\,mol^{-1}}$ is the Faraday constant and n is the number of moles of electrons participating in the reaction. For a hydrogen fuel cell two electrons pass round the external circuit for each water molecule produced and each molecule of hydrogen used, thus $n = 2$. The change of Gibbs free energy varies with temperature, reactant pressure, and concentration. To account for pressure and concentration the activity a_i of the reactant and product species is introduced. These activity of the reactants and products modify the change of Gibbs free energy of reaction as shown in next expression for a hydrogen fuel cell reaction [80]:

$$\Delta G(T,p) = \Delta G^0(T,p^0) - RTln\left(\frac{a_{H_2} \cdot a_{O_2}^{0.5}}{a_{H2O}}\right) \tag{A.5}$$

Next equation shows how the latter relation affects the Nernst reversible voltage:

$$E = \frac{-\Delta G^0}{nF} + \frac{RT}{nF} ln\left(\frac{a_{H_2} \cdot a_{O_2}^{0.5}}{a_{H2O}}\right) \tag{A.6}$$

Assuming ideal gas law and assuming that at high temperatures (e.g. SOFC at 900 °C) H_2O behaves as an ideal gas, the activity of the species is as follows:

$$a_{H_2} = \frac{p_{H_2}}{p^0} \tag{A.7}$$

$$a_{O_2} = \frac{p_{O_2}}{p^0} \tag{A.8}$$

$$a_{H_2O} = \frac{p_{H_2O}}{p^0} \tag{A.9}$$

$$\tag{A.10}$$

Then eq. A.6 becomes:

$$E = \frac{-\Delta G^0}{nF} + \frac{RT}{nF} ln \left(\frac{\frac{p_{H_2}}{p^0} \cdot \left(\frac{p_{O_2}}{p^0} \right)^{0.5}}{\frac{p_{H2O}}{p^0}} \right) \tag{A.11}$$

If all the pressures are given in bar, than p^0 =1, the latter equation can be simplified to:

$$E = \frac{-\Delta G^0}{nF} + \frac{RT}{nF} ln \left(\frac{p_{H_2} \cdot p_{O_2}^{0.5}}{p_{H2O}} \right) \tag{A.12}$$

The first term of the right hand side can be written as:

$$E^0 = \frac{-\Delta G^0}{nF} \tag{A.13}$$

This makes the final Nernst voltage relation as follows:

$$E = E^0 + \frac{RT}{nF} ln \left(\frac{p_{H_2} \cdot p_{O_2}^{0.5}}{p_{H2O}} \right) \tag{A.14}$$

A.2. Activation voltage loss

Electrochemical reactions have to overcome energy barriers before the reaction will proceed. This barrier is also called 'activation energy' and leads to activation loss, and can be described by the Butler-Volmer equation. Eq. A.15 is proposed by Chan et al. [63].

$$i = i_0 \cdot \left(exp \left(\frac{n \cdot \beta \cdot F \cdot \Delta V_{act}}{RT} \right) - exp \left(\frac{-(1-\beta) \cdot n \cdot F \cdot \Delta V_{act}}{RT} \right) \right) \tag{A.15}$$

Where i is the current density (A m^{-2}), i_0 is the exchange current density (A m^{-2}), which represents the forward and reverse electrode reaction rate at the equilibrium potential. β is the charge transfer coefficient, which represents the part of change in polarization leading to a change in the reaction rate constant, its value is usually 0.5 for fuel cell applications [29, 63]. n is the number of moles of electrons participating in the reaction (in this case $n = 2$). With $\beta = 0.5$, eq. A.15 can be rewritten to:

$$\Delta V_{act} = \frac{RT}{F} \sinh^{-1} \left(\frac{i}{2 i_{0,a}} \right) + \frac{RT}{F} \sinh^{-1} \left(\frac{i}{2 i_{0,c}} \right) \tag{A.16}$$

Before the Butler-Volmer equations was used to describe activation loss, Tafel observed that the overvoltage at the surface of an electrode followed a similar pattern in great variety of electrochemical reactions. This general pattern is represented by eq. A.17. Although the Tafel equation was originally deduced from experimental results, it also has a theoretical basis. It can be shown that for a hydrogen fuel cell with two electrons transferred per mole, the constant A in eq. A.17 is given by: $RT/(n\beta F)$ and results in eq. A.18. This equation holds for high overpotential regions and is easier to use. For low overpotential regions the current is influenced by both anodic and cathodic reactions and the Tafel equation is not representative any more. In low current regions the Butler-Volmer equation should be used for an accurate representation of the activation voltage loss. [5].

$$\Delta V_{act} = A \ln \left(\frac{i}{i_0} \right) \tag{A.17}$$

$$\Delta V_{act} = \frac{RT}{n\beta F} ln \left(\frac{i}{i_0} \right) \tag{A.18}$$

A.3. Concentration voltage loss (mass transfer limitations)

Concentration voltage loss occurs due to the reduction in concentration, caused by mass transfer slowness on both anode and cathode side. The extent of this change in concentration will depend on the current being drawn from the fuel cell. On physical factors it depends on how well the air around the cathode can circulate, and how quickly the fuel or air can be replenished in the anode. Concentration voltage loss is described by:

$$\Delta V_{conc} = \frac{RT}{n\alpha F} ln \left(\frac{C_b}{C_{inf}} \right) = -\frac{RT}{n\alpha F} ln \left(1 - \frac{i}{i_{limit}} \right) \tag{A.19}$$

Where C_b is the concentration ($\mathrm{mol\,m^{-3}}$) at the triple-phase boundary (where electrolyte, gas, and electrode contacts). C_{inf} is the bulk concentration of reactant, i_{limit} is limiting current density ($\mathrm{A\,m^{-2}}$) evaluated at $C_b = 0$, and n is the number of moles of electrons participating in the reaction. In this case $n = 2$.

A.4. Ohmic voltage loss

Ohmic voltages losses occur because of the resistance to the ion flow in the electrolyte and the resistance to the current flow through the electrode materials. The Ohmic voltage loss is described as follows:

$$\Delta V_{ohm} = i \cdot r_{ohm} \tag{A.20}$$

Where i is the current density ($\mathrm{A\,m^{-2}}$), and r_{ohm} the area-specific resistance ($\Omega\,\mathrm{m^{-2}}$) calculated from the conductivity of each layer:

$$r_{ohm} = \frac{\tau_{ae}}{\sigma_{ae}} + \frac{\tau_{ce}}{\sigma_{ce}} + \frac{\tau_{se}}{\sigma_{se}} \tag{A.21}$$

A.5. Fuel crossover

This energy loss results from the waste of fuel passing through the electrolyte, and, to a lesser extent, from electron conduction through the electrolyte. The electrolyte should only transport ions through the cell. However a certain amount of fuel diffusion and electron flow will always be possible due to micro-cracks and fissures in the electrolyte. This phenomenon is hard to define mathematically.

B

Thermodynamic properties SOFC modeling

This appendix describes the methods for obtaining thermodynamic properties used for SOFC modeling such as: molar mass, dynamic viscosity, isobaric heat capacity, thermodynamic conductivity, enthalpy, Gibbs free energy, and lower heating values.

B.1. Molar mass

The molar mass is taken from Perry's chemical engineering handbook [67].

Table B.1: Molar mass

Species	**Molar mass (M)**	**unit**
CH_4	16.04250	$\mathrm{g\,mol^{-1}}$
H_2O	18.01528	$\mathrm{g\,mol^{-1}}$
H_2	02.01588	$\mathrm{g\,mol^{-1}}$
CO	28.01010	$\mathrm{g\,mol^{-1}}$
CO_2	44.00950	$\mathrm{g\,mol^{-1}}$
O_2	31.99880	$\mathrm{g\,mol^{-1}}$
N_2	28.01340	$\mathrm{g\,mol^{-1}}$

B.2. Dynamic viscosity

The dynamic viscosity μ (Pa s) is temperature dependent. To determine μ for each component, Todd and Young [81] published a set of sixth-order polynomial curve fits. Thereupon, dynamic viscosity for the mixture is determined by a ideal-gas mixing law (eq. B.3). The SOFC model invokes a separate MatLab script in order to calculate the temperature dependent dynamic viscosity of the anode and cathode flow mixture.

$$\mu = \sum_{k=0}^{6} b_k \cdot \left(\frac{T}{1000}\right)^k \cdot 10^{-7} \tag{B.1}$$

$$\mu_{mix} = \sum_i \frac{X_i \mu_i}{\sum_j X_i \Phi_{ij}} \tag{B.2}$$

$$\Phi_{ij} = \frac{\left[1 + \left(\frac{\mu_i}{\mu_j}\right)^{1/2} \left(\frac{M_i}{M_j}\right)^{1/4}\right]^2}{\left[8\left(1 + \frac{M_i}{M_j}\right)\right]^{1/2}} \tag{B.3}$$

B.3. Isobaric heat capacity

The molar isobaric heat capacity c_p ($\mathrm{J\,mol^{-1}\,K^{-1}}$) is temperature dependent. Again a set of sixth order polynomial curve fits of Todd and Young is used [81] (eq. B.4). The molar isobaric heat capacity of an ideal gas mixture is determined with a weighted average (eq. B.5). The SOFC model invokes a separate MATLAB script in order to calculate the temperature dependent molar isobaric heat capacity of the anode and cathode flow mixture.

$$c_p = \sum_{k=0}^{6} a_k \cdot \left(\frac{T}{1000}\right)^k \cdot 10^{-7} \tag{B.4}$$

$$c_{p,mix} = \sum_{x=1}^{n} X_x \cdot C_{p,x}(T) \tag{B.5}$$

B.4. Thermodynamic conductivity

As before, to determine the thermodynamic conductivity k ($\mathrm{W\,m^{-1}\,K^{-1}}$) a set of sixth order polynomial curve fits of Todd and Young is used [81] (eq. B.6). Thereupon, thermal conductivity for the mixture is determined by a ideal-gas mixing law (eq. B.8). The SOFC model invokes a separate MATLAB script for calculating the temperature dependent thermal conductivity of the anode and cathode flow mixture.

$$k = \sum_{k=0}^{6} c_k \cdot \left(\frac{T}{1000}\right)^k \cdot 10^{-2} \tag{B.6}$$

$$k_{mix} = \sum_i \frac{X_i\, k_i}{\sum_j X_j \Phi_{ij}} \tag{B.7}$$

$$\Phi_{ij} = \frac{\left[1 + \left(\frac{\mu_i}{\mu_j}\right)^{1/2} \left(\frac{M_i}{M_j}\right)^{1/4}\right]^2}{\left[8\left(1 + \frac{M_i}{M_j}\right)\right]^{1/2}} \tag{B.8}$$

B.5. Enthalpy

The molar specific enthalpy h_i ($\mathrm{J\,mol^{-1}}$) of each species is approximated using first order polynomials of temperature as listed in table B.2. These first order polynomials are based on data which is computed with the ideal gas law thermodynamic model (Gasmix) in *FluidProp* [64].

Table B.2: Molar specific enthalpy fit functions for a temperature range of 700-1500 K

Species	**Fit function**	**unit**
CH_4	$74.66 \cdot T - 1.105e5$	$\mathrm{J\,mol^{-1}}$
H_2O	$42.45 \cdot T - 2.58e5$	$\mathrm{J\,mol^{-1}}$
H_2	$30.68 \cdot T - 9911$	$\mathrm{J\,mol^{-1}}$
CO	$33.57 \cdot T - 1.223e5$	$\mathrm{J\,mol^{-1}}$
CO_2	$55.03 \cdot T - 4.149e5$	$\mathrm{J\,mol^{-1}}$
O_2	$35.15 \cdot T - 1.1235e4$	$\mathrm{J\,mol^{-1}}$
N_2	$33.12 \cdot T - 1.154e4$	$\mathrm{J\,mol^{-1}}$

B.6. Gibbs free energy

Gibbs free energy for hydrogen oxidation ΔG_{HOR} ($\mathrm{J\,mol^{-1}}$), methane steam reforming ΔG_{MSR}, and water-gas shift ΔG_{WGS} is calculated with the ideal gas law thermodynamic model (Gasmix) in *FluidProp* [64]. In the temperature range of 700-1500 K, for concerning species, the molar specific enthalpy and entropy is determined. Thereafter, using eq. B.9, B.10, B.12, and B.14 the Gibbs free energy is determined. Finally, for easy implementation in the model, a first order polynomial of temperature is made: eq. B.11, B.13, and B.15.

$$G_i\ [\mathrm{J\,mol^{-1}}] = h_i - T \cdot s_i \tag{B.9}$$

$$\Delta G_{HOR} = G_{H_2O} - 0.5 G_{O_2} - G_{H_2} \tag{B.10}$$

$$\Delta G_{HOR} = -54.6 \cdot T + 2.478 \cdot 10^5 \tag{B.11}$$

$$\Delta G_{MSR} = 3 \cdot G_{H_2} + G_{CO} - G_{CH_4} - G_{H_2O} \tag{B.12}$$

$$\Delta G_{MSR} = -254.3 \cdot T + 2.26 \cdot 10^5 \tag{B.13}$$

$$\Delta G_{WGS} = G_{H_2} + G_{CO2} - G_{H_2O} - G_{CO} \tag{B.14}$$

$$\Delta G_{WGS} = 30.69 \cdot T - 3.401 \cdot 10^4 \tag{B.15}$$

B.7. Lower heating values

The lower heating values (LHV) are taken from Perry's chemical engineering handbook [67] and presented in table B.3.

Table B.3: Lower heating value at standard conditions (T = 298.15 K and p = 1 atm)

Species	**LHV**	**unit**
CH_4	$802.6 \cdot 10^3$	$\mathrm{J\,mol^{-1}}$
H_2	$283.0 \cdot 10^3$	$\mathrm{J\,mol^{-1}}$
CO	$241.8 \cdot 10^3$	$\mathrm{J\,mol^{-1}}$

C

SOFC model - validation results

C.1. Mass and element conservation

Figure C.1 presents the anode channel species mole fraction against simulation time. Only the first three seconds of simulation are depicted, within this time bracket steady condition is achieved. This figure illustrates the fast response of the methane steam reforming reaction. The water-gas shift and hydrogen oxidation take more time, as can be seen in the subsequent two seconds.

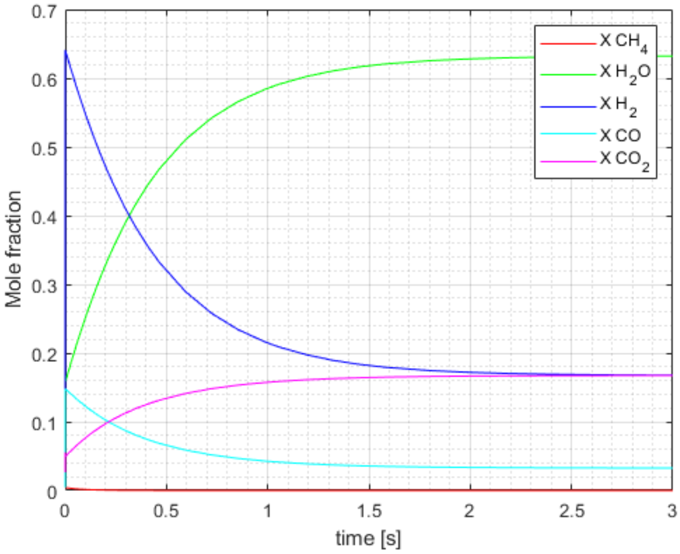

Figure C.1: Fuel channel component mole fractions at outlet. Inlet conditions from table 4.5

While molar flow rates change due to the methane steam reforming, water-gas shift, and hydrogen oxidation reactions, element and mass conservation across the SOFC inlet and outlet should hold. Two cases are considered to check if mass and elements are conserved. Case 1 is without any current drawn (open circuit), case 2 is with a current density of 5000 $\mathrm{A\,m^{-2}}$. For both cases the simulation is performed with a fixed fuel mass flow ($1.8 \cdot 10^{-5}$ $\mathrm{kg\,s^{-1}}$) and air mass flow ($6.05 \cdot 10^{-4}$ $\mathrm{kg\,s^{-1}}$). The other input conditions are as provided in table 4.5. The simulation time is set to 1000 seconds.

Table C.1 provides the input flows, table C.2 provides the output flows for open circuit condition (case 1). Table C.3 provides the output flows for the case where a current is drawn (case 2). It is concluded that both mass and elements are conserved. The mass ingoing is equal to total mass outgoing. Moreover, for both cases holds that the number of elements ingoing is equal to number of elements outgoing.

Table C.1: Element and mass conservation, ingoing (0-D SOFC).

Species in	x^{in} [-]	$\dot{N}^{in}$ [mol s^{-1}]	$\dot{C}^{in}$ [mol m^{-3} s^{-1}]	$\dot{m}^{in}$ [kg s^{-1}]
CH_4	2.82e-1	3.12e-4	7.80	5.01e-6
H_2O	5.66e-1	6.27e-4	1.57e1	1.13e-5
H_2	1.21e-1	1.34e-4	3.35	2.70e-7
CO	4.00e-3	4.43e-6	1.11e-1	1.24e-7
CO_2	2.70e-2	2.99e-5	0.747	1.32e-6
O_2	2.10e-1	4.41e-3	1.11e2	1.41e-4
N_2	7.90e-1	1.66e-2	4.14e2	4.64e-4
Total mass in	-	-	-	6.23e-4
Elements in	**-**	$\dot{N}^{in}$ [mol s^{-1}]	**-**	**-**
C	-	3.50e-3	-	-
H	-	2.77e-3	-	-
O	-	9.50e-3	-	-
N	-	1.66e-2	-	-

Table C.2: Element and mass conservation, outgoing, case 1 - open circuit (0-D SOFC).

Species out	x^{out} [-]	$\dot{N}^{out}$ [mol s^{-1}]	$\dot{C}^{out}$ [mol m^{-3} s^{-1}]	$\dot{m}^{out}$ [kg s^{-1}]
CH_4	4.49e-3	7.75e-6	1.94e-1	1.24e-7
H_2O	1.53e-1	2.65e-4	6.61	4.78e-6
H_2	6.47e-1	1.12e-4	2.79e1	2.26e-6
CO	1.55e-1	2.67e-4	6.66	7.49e-6
CO_2	4.60e-2	7.89e-4	1.97	3.47e-6
O_2	2.10e-1	4.41e-3	1.11e2	1.41e-4
N_2	7.90e-1	1.66e-3	4.14e2	4.64e-4
Total mass out	-	-	-	6.23e-4
Error	-	-	-	0 %
Elements out	**-**	$\dot{N}^{out}$ [mol s^{-1}]	**-**	**-**
C	-	3.50e-3	-	-
H	-	2.77e-3	-	-
O	-	9.50e-3	-	-
N	-	1.66e-2	-	-
Error	-	0 %	-	-

Table C.3: Element and mass conservation, outgoing, case 2 - i=5000 $\mathrm{A\,m^{-2}}$ (0-D SOFC).

Species out	x^{out} [-]	$\dot{N}^{out}$ [$\mathrm{mol\,s^{-1}}$]	$\dot{C}^{out}$ [$\mathrm{mol\,m^{-3}\,s^{-1}}$]	$\dot{m}^{out}$ [$\mathrm{kg\,s^{-1}}$]
CH_4	1.23e-6	2.09e-8	3.35e-4	3.36e-10
H_2O	6.35e-1	1.09e-3	1.16e1	1.97e-5
H_2	1.67e-1	2.90e-4	3.08	5.84e-5
CO	3.26e-2	6.07e-5	0.65	1.70e-6
CO_2	1.65e-1	2.86e-4	3.04	1.28e-5
O_2	2.10e-1	4.41e-3	1.10e2	1.41e-4
N_2	7.90e-1	1.66e-3	4.14e2	4.64e-4
Total mass out	-	-	-	6.23e-4
Error	-	-	-	0 %
Elements out	**-**	$\dot{N}^{out}$ [$\mathrm{mol\,s^{-1}}$]	**-**	**-**
C	-	3.50e-3	-	-
H	-	2.77e-3	-	-
O	-	9.50e-3	-	-
N	-	1.66e-2	-	-
Error	-	0 %	-	-

C.2. Chemical equilibrium

Assuming that the chemical reactions are fast enough to achieve chemical equilibrium in the fuel channel, the expected output chemical equilibrium composition can be used as a verification method. The reference chemical equilibrium output composition is computed with the chemical reaction module of *Factsage*. For this verification the operating temperature of the 0-D SOFC model is kept constant at 1023 K. Again, two cases are considered: Case 1 is without any current drawn (table C.4), case 2 is with current density of 5000 $\mathrm{A\,m^{-2}}$ (table C.5).

The chemical equilibrium composition achieved in both cases is almost equal to the chemical equilibrium composition predicted by *Factsage*. The deviations are expected to be small enough for this study.

Table C.4: Chemical equilibrium check 0-D SOFC, at 1023 K, Case 1: $i = 0\,\mathrm{A\,m^{-2}}$ (0-D SOFC)

Species	***Factsage***	**0-D SOFC**
$x_{CH_4}^{out}$ [-]	5.00e-3	4.54e-3
$x_{H_2O}^{out}$ [-]	1.59e-1	1.56e-1
$x_{H_2}^{out}$ [-]	6.39e-1	6.42e-1
x_{CO}^{out} [-]	1.48e-1	1.48e-1
$x_{CO_2}^{out}$ [-]	4.90e-2	4.91e-2

Table C.5: Chemical equilibrium check 0-D SOFC, at 1023 K, Case 2: $i = 5000\,\mathrm{A\,m^{-2}}$ (0-D SOFC)

Species	***Factsage***	**0-D SOFC**
$x_{CH_4}^{out}$ [-]	5.41e-6	1.22e-6
$x_{H_2O}^{out}$ [-]	6.31e-1	6.32e-1
$x_{H_2}^{out}$ [-]	1.69e-1	1.68e-1
x_{CO}^{out} [-]	3.36e-2	3.27e-1
$x_{CO_2}^{out}$ [-]	1.67e-1	1.67e-1

C.3. Energy conservation

Energy conservation is used to verify that the energy balances are correctly implemented in the model. A total energy balance is expressed in eq. C.1.

$$\begin{gathered} 0 = \sum_i \dot{N}_i^{in} \cdot h_i^{in} - \sum_i \dot{N}_i^{out} \cdot h_i^{out} - IV \\ i \in (\mathrm{CH_4},\ \mathrm{H_2O},\ \mathrm{H_2},\ \mathrm{CO},\ \mathrm{CO_2},\ \mathrm{O_2},\ \mathrm{N_2}) \end{gathered} \tag{C.1}$$

The two above mentioned cases are simulated at 1000 seconds and 10000 seconds. Table C.6 provides the results of three simulations. It is concluded that energy is conserved since the error is small and is converging to zero.

Table C.6: Energy conservation (0-D SOFC)

Case	IV [W]	**error** [W]	**error [% w.r.t electric power]**
Case 1 (no current)	0	0	0
Case 2 (i=5000$\mathrm{A\,m^{-2}}$)	143	0.052	0.035
Case 2 (i=5000$\mathrm{A\,m^{-2}}$) run time = 10000 s	143	0.034	0.025

D

SOFC model - parameter sensitivity analysis

In this appendix the effects two SOFC modeling assumptions are investigated.

D.1. Effect of temperature dependent thermal conductivity, gas density, and isobaric heat capacity:

As explained in chapter 4, the temperature dependency of: thermal conductivity, gas density, and isobaric heat capacity is neglected. These parameters are calculated for the inlet temperature conditions only and are kept constant throughout the simulation. To study the effects of this simplification, a simulation is performed where the temperature dependency is taken into account. Figure D.1 depicts the dynamic response of this simulation. It is concluded that the effects are negligible and that the initial simplification is justified. However, it should be noted that the computation time is tripled when running these temperature-dependent simulations. The increased computational burden does not weigh up against the improved accuracy.

D.2. Effect of Nusselt number:

The model developed by Aguiar uses a constant Nusselt number of 3.09 for both air and fuel flow. This Nusselt number is based on ref. [82]. 3.09 is obtained by using a squared channel and constant heat input per unit length. There is no Reynolds or Prandtl dependency. In the model here developed: the Nusselt number is determined using a relation from Mills Basic Heat and Mass Transfer [65]. This Nusselt number is depending on Reynolds number and Prandtl number and holds by the assumption of a laminar flow between parallel plates with fully developed hydrodynamics. In present model the average Nusselt number obtained by Mills relation is 7.54. Because it is difficult to say which method is the most realistic approach; both methods are implemented and tested. Figure D.2 depicts the difference.

As expected, due to the higher Nusselt number in present model, the heat transfer between the solid parts and the gas streams is higher, which leads to a better heat spread between layers and thus lower overall temperatures and accordingly higher cell voltage. Although the effects are small, the Nusselt number is affecting the simulation results. The Nusselt number relation suggested by Mills is used in further simulations since it has a more suitable physical justification.

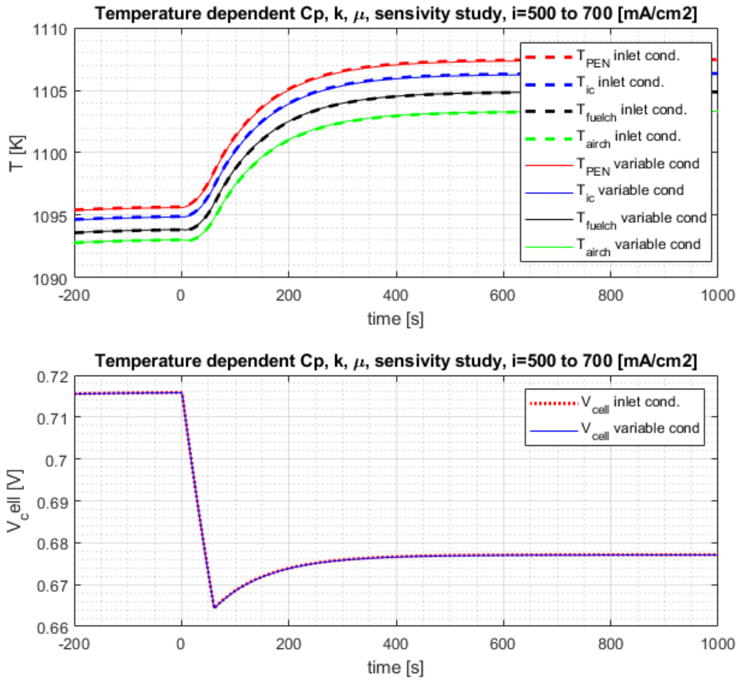

Figure D.1: 0-D SOFC: temperature and voltage response for constant (dashed line) and varying (solid line) thermodynamic properties, after a load change from $i = 5000\,\mathrm{A\,m^{-2}}$ to $i = 7000\,\mathrm{A\,m^{-2}}$

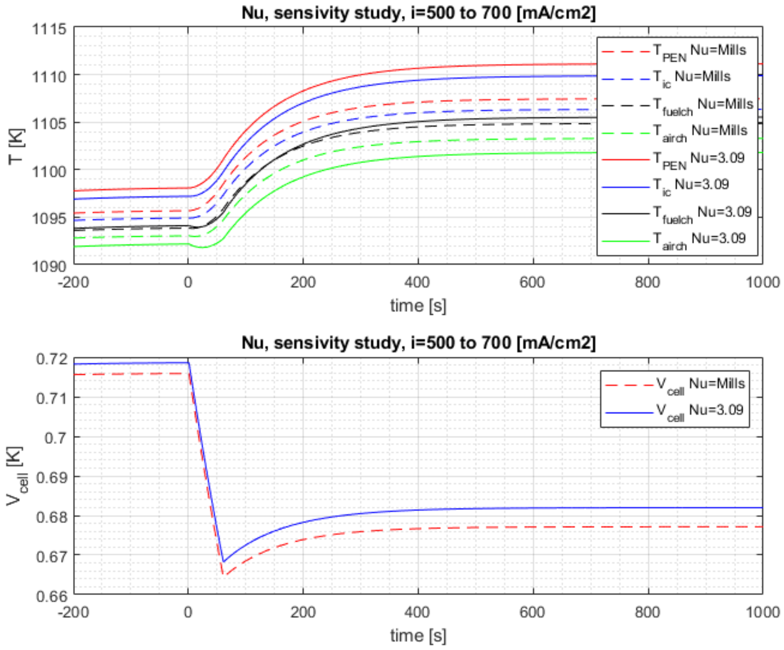

Figure D.2: 0-D SOFC: temperature and voltage response for two different Nusselt numbers, after a load change from $i = 5000\,\mathrm{A\,m^{-2}}$ to $i = 7000\,\mathrm{A\,m^{-2}}$

E

Engine cylinder geometry

Figure E.1 depicts a schematic overview of the geometry of cylinder, connecting rod, and crank shaft. The following parameters define the basic geometry of a reciprocating engine.

$$V_1 = \frac{\pi D_B^2 L_s r_c}{4(\epsilon_c - 1)} \tag{E.1}$$

$$r_c = (\epsilon_c - 1)x_c + 1 \tag{E.2}$$

$$x_c = \frac{L_{IC}}{L_{BDC}} \tag{E.3}$$

$$L_{IC} = L_s\left(\frac{1}{\epsilon_c - 1} + \frac{1}{2}\left((1 - \cos(\alpha_{IC})) + \frac{1}{\lambda_{CR}}(1 - \sqrt{1 - \lambda_{CR}^2 \sin^2(\alpha_{IC})}\right)\right) \tag{E.4}$$

$$\lambda_{CR} = \frac{R_{CR}}{L_{CR}} = \frac{L_s}{2L_{CR}} \tag{E.5}$$

$$L_{BDC} = \frac{\epsilon_c L_s}{\epsilon_c - 1} \tag{E.6}$$

$$r_{EO} = \frac{V_6}{V_1} = \frac{L_{EO}}{L_{IC}} \tag{E.7}$$

$$L_{EO} = L_s\left(\frac{1}{\epsilon_c - 1} + \frac{1}{2}\left((1 - \cos(\alpha_{EO})) + \frac{1}{\lambda_{CR}}(1 - \sqrt{1 - \lambda_{CR}^2 \sin^2(\alpha_{EO})}\right)\right) \tag{E.8}$$

$$r_e = \frac{V_6}{V_3} \cdot \frac{V_3}{V_4} \cdot \frac{V_4}{V_5} = \frac{r_{EO} r_c}{bc} \tag{E.9}$$

V_1 is the cylinder volume at start of compression, D_B is the bore diameter, L_s is the stroke length, ϵ_c is the geometric compression ratio determined by cylinder dimensions, r_c is the effective compression ratio, which is determined with the compression stroke effectiveness factor (x_c). L_{IC} is the distance between top of the cylinder and the piston crown, L_p (figure E.1) is cylinder space length when the inlet valve closes, L_{BDC} is the cylinder space length when the cylinder is at bottom dead centre position and L_{TCD} is the cylinder space length when the cylinder is at top dead centre position. L_{CR} is the length of the crank rod, $alpha_{IC}$ is the crank angle when the inlet valve closes, λ_{RC} is ratio of the crank radius (R_{CR}) to the length of the connecting rod, r_{EO} is the ratio of volume between Seiliger point 6 and 1, and r_e is the effective expansion ratio between Seiliger point 6 and 5.

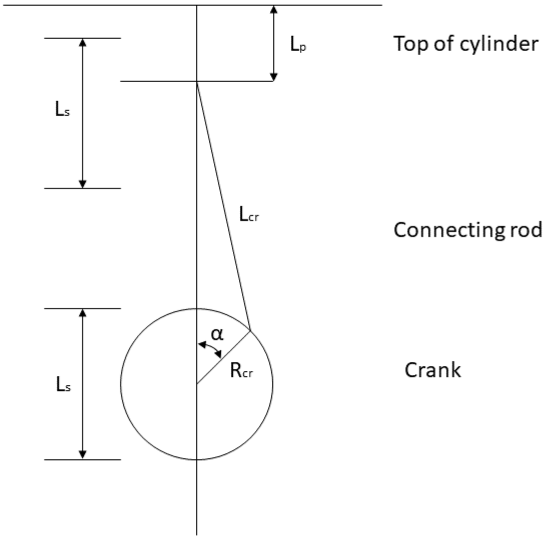

Figure E.1: Schematic of piston, connecting rod/crank shaft [83]

F

Thermodynamic properties ICE modeling

Computation steps in thermodynamic properties library for: fuel, air, and stoichiometric gas. The subscript i denotes the constituent.

F.1. Lower heating value

1. Set volume fractions of species in fuel (y_i). This is including a percentage of hydrogen if added.
2. Set density of constituents (ρ_i).
3. Determine mass fraction in fuel of constituents ($x_i = \frac{m_i}{m_{fuel}}$).
4. Determine fuel density based on mass composition.
5. Set fuel volumetric lower heating value ($\mathrm{J\,m^{-3}}$) and calculate graviatmetric lower heating value ($\mathrm{J\,kg^{-1}}$).

F.2. Stoichiometric air to fuel ratio and mass fractions

1. Determine mass fractions of constituents in dry air.
2. Determine mass fraction per element in fuel (C: x_C, H: x_H, S: x_S, O: x_O).
3. Determine stoichiometric ratio: $\sigma = \frac{M_{air}}{y_{o_2,air}} \cdot \left(\frac{x_C}{M_c} + \frac{x_H}{M_H} + \frac{x_S}{M_S}\right)$
4. Determine mass fractions of the constituents in stoichiometric gas: $x_{i,sg} = x_{i,air} \cdot \frac{\sigma}{(\sigma+1)}$

F.3. Gas constant and specific heat capacity of air, fuel and stoichiometric gas

1. Set gas constant per constituent (R_i).
2. Determine gas constant $R_{mix} = \sum x_i \cdot R_i$
3. Set coefficients of polynomial functions of $c_{p,i}(k)$ per constituent. Data set is provided by Stapersma, for more information see: [84].
4. Determine isobaric heat per constituent: $c_{p,i} = \sum_{k=1}^{k} c_{p,i}(k) \cdot \left(\frac{T}{1000}\right)^{(k-1)}$
5. $c_{p,mix} = \sum x_i \cdot c_{p,i}$
6. $c_{v,mix} = c_{p,mix} - R_{mix}$

G

ICE model validation

Three parameter sets (table 5.3) are loaded in the developed MVFP engine model to validate performance. The model results are compared with results from experiments and detailed engine modeling [20]. It can be concluded that the MVFP model is predicting accurate engine performance, the maximum deviation is 1.5 %.

The validation is done in three ways: performance calculations, p-V diagram comparison (the model results are indicated with a '*', the reference model results are indicated with a 'o'), and a comparison of temperature and pressure at specific points (indicated in bar charts).

For operating natural gas only, see table G.1, figure G.1 and G.2. The results are within 1 % accuracy.

Table G.1: ICE MVFP mode results, operating NG.

Parameter	**MVFP model**	**Detailed model**	**unit**
P_e	375.6	375.0	kW
η_e	33.73	33.68	%

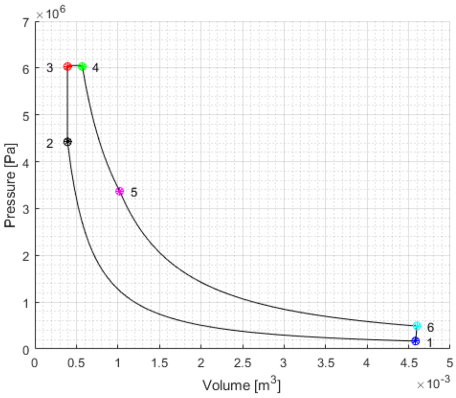

Figure G.1: p-V diagram, MVFP model (star) and detailed model (o), operating NG.

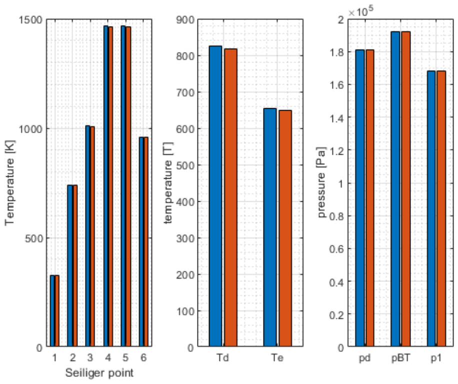

Figure G.2: Gas exchange pressure, MVFP model (model) and measured (red), operating NG.

For operating 10 % hydrogen, 90 % natural gas, see table G.2, figure G.3 and G.4 The results are within 1 % accuracy.

Table G.2: ICE MVFP mode results, operating 10HNG.

Parameter	MVFP model	Detailed model	unit
P_e	376.8	375.0	kW
η_e	34.43	34.26	%

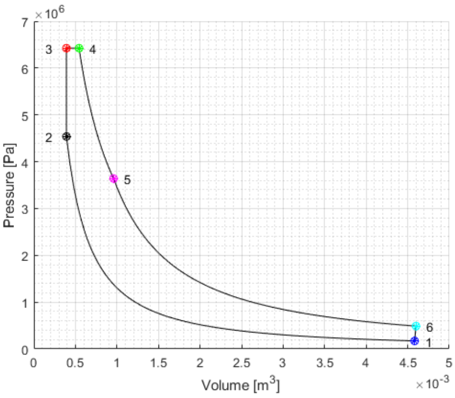

Figure G.3: p-V diagram, MVFP model (star) and detailed model (o), operating 10HNG.

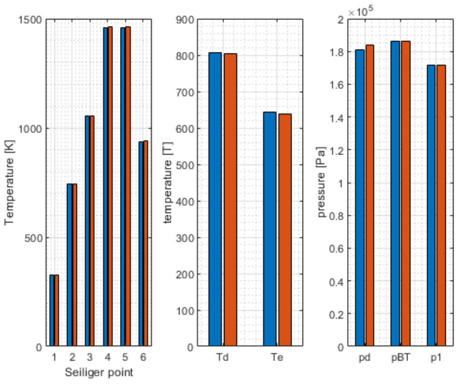

Figure G.4: Gas exchange pressure, MVFP model (model) and measured (red), operating 10HNG.

For operating 20 % hydrogen, 80 % natural gas, see table G.3, figure G.5 and G.6. The results are within 1.5 % accuracy.

Table G.3: ICE MVFP mode results, operating 20HNG.

Parameter	MVFP model	Detailed model	unit
P_e	380.1	375.0	kW
η_e	35.25	34.77	%

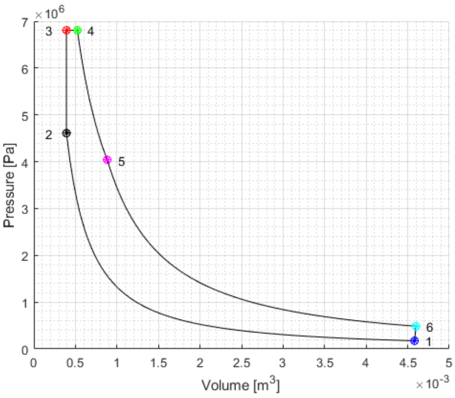

Figure G.5: p-V diagram, MVFP model (star) and detailed model (o), operating 20HNG.

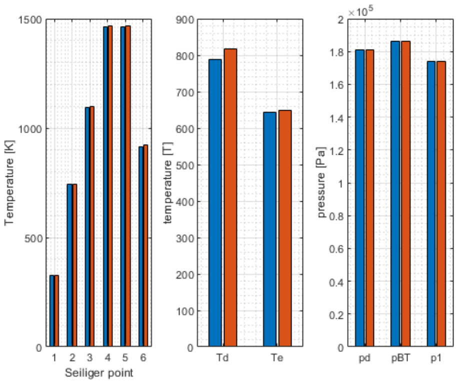

Figure G.6: Gas exchange pressure, MVFP model (model) and measured (red), operating 20HNG.

Bibliography

[1] D Stapersma. *Diesel Engines, Volume 1 Performance analysis*. DELFT UT, NLDA, Delft, 1 edition, 2010.

[2] IMO. Adoption of the Initial IMO Strategy on Reduction of GHG Emissions From Ships and Existing Imo Activity Related To Reducing Ghg Emissions in the Shipping Sector. 2018.

[3] IMO. Third IMO greenhouse gas study, 2014.

[4] Timothy J McCoy and John V Amy. The state-of-the-art of integrated electric power and propulsion systems and technologies on ships. *IEEE Electric Ship Technologies Symposium, ESTS 2009*, pages 340–344, 2009.

[5] Andrew Dicks and James Larminie. *Fuel Cell Systems Explained*. Wiley, Oxford Brookes University UK, University of Queensland, Australia, second edition, 2003.

[6] Stefano Campanari. Full Load and Part-Load Performance Prediction for Integrated SOFC and Microturbine Systems. *Journal of Engineering for Gas Turbines and Power*, 122(2):239, 2002.

[7] Sung Ho Park, Young Duk Lee, and Kook Young Ahn. Performance analysis of an SOFC/HCCI engine hybrid system: System simulation and thermo-economic comparison. *International Journal of Hydrogen Energy*, 39(4):1799–1810, jan 2014.

[8] Annamaria Buonomano, Francesco Calise, Massimo Dentice D'Accadia, Adolfo Palombo, and Maria Vicidomini. Hybrid solid oxide fuel cells–gas turbine systems for combined heat and power: A review. *Applied Energy*, 156:32–85, oct 2015.

[9] Stefano Campanari, Luca Mastropasqua, Matteo Gazzani, Paolo Chiesa, and Matteo C. Romano. Predicting the ultimate potential of natural gas SOFC power cycles with CO2 capture – Part A: Methodology and reference cases. *Journal of Power Sources*, 324:598–614, aug 2016.

[10] L. Barelli, G. Bidini, and A. Ottaviano. Integration of SOFC/GT hybrid systems in Micro-Grids. *Energy*, 118:716–728, 2017.

[11] SE Veyo, SD Vora, KP Litzinger, and WL Lundberg. Status of pressurized SOFC/gas turbine power system development at Siemens Westinghouse. *ASME TURBO EXPO*, 2002.

[12] T Kabata, M Nishiura, K Tomida, S Koga, and N Matake. MHI SOFC/GT hybrid system. *Fuel cell seminar & exposition*, 2008.

[13] L van Biert, T Woudstra, M Godjevac, K Visser, and P V Aravind. A thermodynamic comparison of solid oxide fuel cell-combined cycles. *Journal of Power Sources*, 397(September):382–396, 2018.

[14] Flavio D.F. Chuahy and Sage L. Kokjohn. Solid oxide fuel cell and advanced combustion engine combined cycle: A pathway to 70% electrical efficiency. *Applied Energy*, 235:391–408, feb 2019.

[15] Us Environmental Protection Agency, Combined Heat, and Power Partnership. Catalog of CHP Technologies, Full Report, September 2017. (September), 2017.

[16] C G Bauer and T W Forest. Effect of hydrogen addition on the performance of methane-fueled vehicles. Part II: driving cycle simulations. *International Journal of Hydrogen Energy*, 26(1):71–90, jan 2001.

[17] Fanhua Ma and Yu Wang. Study on the extension of lean operation limit through hydrogen enrichment in a natural gas spark-ignition engine. *International Journal of Hydrogen Energy*, 33(4):1416–1424, 2008.

[18] Erjiang Hu, Zuohua Huang, Bing Liu, Jianjun Zheng, and Xiaolei Gu. Experimental study on combustion characteristics of a spark-ignition engine fueled with natural gas–hydrogen blends combining with EGR. *International Journal of Hydrogen Energy*, 34(2):1035–1044, jan 2009.

[19] Roopesh Kumar Mehra, Hao Duan, Romualdas Juknelevičius, Fanhua Ma, and Junyin Li. Progress in hydrogen enriched compressed natural gas (HCNG) internal combustion engines - A comprehensive review. *Renewable and Sustainable Energy Reviews*, 80:1458–1498, dec 2017.

[20] Harsh D Sapra, Youri Linden, Wim Sluijs van, Milinko Godjevac, and Klaas Visser. Experimental investigations of hydrogen-natural gas engines for maritime applications. In *ASME 2018 Internal Combustion Engine*, San Diego, CA, USA, 2018. Division Fall Technical Conference ICEF2018.

[21] A. Boudghene Stambouli and E. Traversa. Solid oxide fuel cells (SOFCs): A review of an environmentally clean and efficient source of energy. *Renewable and Sustainable Energy Reviews*, 6(5):433–455, 2002.

[22] R Bove, (European Commission DG-joint research centre Petten The Netherlands) and S Ubertini (DiT-Dipartimento per le Tecnology University of Naples Italy). *Modeling Solid Oxide Fuel Cells*. 2008.

[23] Sunfire. Sunfire supplies ThyssenKrupp Marine Systems with 50 kW SOFC. https://www.sunfire.de/en/company/news/detail/sunfire-supplies-thyssenkrupp-marine-systems-with-50-kw-sofc-20 (Date accessed: 2019-04-22).

[24] Z G Yang, D M Paxton, K S Weil, J W Stevenson, and P Singh. Pnnl-14116. (November), 2002.

[25] D Marra and Polverino Pierpaolo. *Models for Solid Oxide Fuel Cell Systems*. Springer, London, 2016.

[26] P. Aguiar, C. S. Adjiman, and Nigel P. Brandon. Anode-supported intermediate temperature direct internal reforming solid oxide fuel cell. I: Model-based steady-state performance. *Journal of Power Sources*, 138(1-2):120–136, 2004.

[27] E Achenbach and E Riensche. Methane/steam reforming kinetics for solid oxide fuel cells. *Journal of Power Sources*, 52(2):283–288, dec 1994.

[28] Ying-Wei Kang, Jun Li, Guang-Yi Cao, Heng-Yong Tu, Jian Li, and Jie Yang. A reduced 1D dynamic model of a planar direct internal reforming solid oxide fuel cell for system research. *Journal of Power Sources*, 188(1):170–176, mar 2009.

[29] Cheng Bao, Ying Wang, Daili Feng, Zeyi Jiang, and Xinxin Zhang. Macroscopic modeling of solid oxide fuel cell (SOFC) and model-based control of SOFC and gas turbine hybrid system. *Progress in Energy and Combustion Science*, 66:83–140, may 2018.

[30] R S Gemmen and C D Johnson. Evaluation of fuel cell system efficiency and degradation at development and during commercialization. *Journal of Power Sources*, 159(1 SPEC. ISS.):646–655, 2006.

[31] Fabian Mueller, Faryar Jabbari, Robert Gaynor, and Jacob Brouwer. Novel solid oxide fuel cell system controller for rapid load following. *Journal of Power Sources*, 172(1):308–323, 2007.

[32] Qingping Fang, Ludger Blum, Roland Peters, Murat Peksen, Peter Batfalsky, and Detlef Stolten. SOFC stack performance under high fuel utilization. *International Journal of Hydrogen Energy*, 40(2):1128–1136, 2015.

[33] A. Salogni and P. Colonna. Modeling of solid oxide fuel cells for dynamic simulations of integrated systems. *Applied Thermal Engineering*, 30(5):464–477, apr 2010.

[34] L. Barelli, G. Bidini, and A. Ottaviano. Solid oxide fuel cell modelling: Electrochemical performance and thermal management during load-following operation. *Energy*, 115:107–119, nov 2016.

[35] J Padullés, G W Ault, and J R McDonald. An integrated SOFC plant dynamic model for power systems simulation. *Journal of Power Sources*, 86(1-2):495–500, 2000.

[36] Marco Sorrentino and Cesare Pianese. Model-based development of low-level control strategies for transient operation of solid oxide fuel cell systems. *Journal of Power Sources*, 196(21):9036–9045, nov 2011.

[37] S H Chan, H K Ho, and Y Tian. Modelling for part-load operation of solid oxide fuel cell–gas turbine hybrid power plant. *Journal of Power Sources*, 114(2):213–227, 2003.

[38] Yutong Qi, Biao Huang, and Jingli Luo. Nonlinear state space modeling and simulation of a SOFC fuel cell. *2006 American Control Conference*, (1):5 pp., 2006.

[39] Ioana Georgescu, Douwe Stapersma, Lars M Nerheim, and Benny Mestemaker. Characterisation of Large Gas and Dual-fuel Engines. *MTZ industrial*, 6(3):64–71, 2016.

[40] K Motyl and T J Rychter. HCCI Engine - A Preliminary analysis. *Journal of KONES Internal Combustion Engines*, 10(3-4):217–225, 2003.

[41] Laura Manofsky, Jiri Vavra, Dennis N Assanis, and Aristotelis Babajimopoulos. Bridging the Gap between HCCI and SI: Spark-Assisted Compression Ignition. (x), 2011.

[42] A Aziz Hairuddin, Talal F Yusaf, and Andrew P Wandel. Predicting the Combustion Behaviour of a Diesel HCCI Engine Using a Zero-Dimensional Single-Zone Model . *Analysis*, (March 2017):1–4, 2011.

[43] A Aziz Hairuddin, Talal Yusaf, and Andrew P Wandel. Single-zone zero-dimensional model study for diesel-fuelled homogeneous charge compression ignition (HCCI) engines using Cantera. *International Journal of Automotive and Mechanical Engineering*, 13(2):3309–3328, 2016.

[44] Kathi Epping, Salvador Aceves, Richard Bechtold, and John E. Dec. The Potential of HCCI Combustion for High Efficiency and Low Emissions. jun 2002.

[45] T. Karthikeya Sharma, G. Amba Prasad Rao, and K. Madhu Murthy. Homogeneous charge compression ignition (HCCI) engines: A review. *Archives of Computational Methods in Engineering*, 23(4):623–657, 2016.

[46] T Korakianitis, A M Namasivayam, and R J Crookes. Natural-gas fueled spark-ignition (SI) and compression-ignition (CI) engine performance and emissions. *Progress in Energy and Combustion Science*, 37(1):89–112, feb 2011.

[47] Heather Thomson, James J Corbett, and James J Winebrake. Natural gas as a marine fuel. *Energy Policy*, 87:153–167, dec 2015.

[48] Haeng Muk Cho and Bang-Quan He. Spark ignition natural gas engines—A review. *Energy Conversion and Management*, 48(2):608–618, feb 2007.

[49] John B Heywood. *Internal combustion engine fundamentals*. McGraw-Hill, New York, 1988.

[50] IMO. IMO - Prevention of Air Pollution from Ships (Marpol IV, reg 13), 2018.

[51] Wartsila. Wartsila 31 - Product Guide, 2018.

[52] Khalid Al-Qurashi, Yu Zhang, and André L Boehman. Impact of intake CO2addition and exhaust gas recirculation on NOxemissions and soot reactivity in a common rail diesel engine. *Energy and Fuels*, 26(10):6098–6105, 2012.

[53] Pia Kilpinen. Optimization of a simplified sub-model for NO emission prediction by CFD in large 4-stroke marine diesel engines. *Fuel Processing Technology*, 91(2):218–228, feb 2010.

[54] Spiridon I Raptotasios, Nikolaos F Sakellaridis, Roussos G Papagiannakis, and Dimitrios T Hountalas. Application of a multi-zone combustion model to investigate the NOx reduction potential of two-stroke marine diesel engines using EGR. *Applied Energy*, 157:814–823, nov 2015.

[55] P. Schulten and D. Stapersma. Mean Value Modelling of the Gas Exchange of a 4-stroke Diesel Engine for Use in Powertrain Applications. *SAE Technical Paper*, (2003-01-0219), 2003.

[56] S A Miedema and Z Lu. The dynamic behavior of a diesel engine. *Proceedings of the WEDA XXII technical conference and 34th Texas A&M dredging seminar, Denver, Colorado, USA*, 2002.

[57] Yu Ding. *PhD Thesis - Characterising Combustion in Diesel Engines*. 2011.

[58] Yu Ding, Douwe Stapersma, and Hugo Grimmelius. Using parametrized finite combustion stage models to characterize combustion in diesel engines. *Energy and Fuels*, 26(12):7099–7106, 2012.

[59] R D Geertsma, R R Negenborn, K Visser, M A Loonstijn, and J J Hopman. Pitch control for ships with diesel mechanical and hybrid propulsion: Modelling, validation and performance quantification. *Applied Energy*, 206:1609–1631, nov 2017.

[60] L van Biert, M Godjevac, K Visser, and P V Aravind. A review of fuel cell systems for maritime applications. *Journal of Power Sources*, 327:345–364, sep 2016.

[61] Sanggyu Kang and Kook-Young Ahn. Dynamic modeling of solid oxide fuel cell and engine hybrid system for distributed power generation. *Applied Energy*, 195:1086–1099, jun 2017.

[62] Wonjae Choi, Jaehyun Kim, Yongtae Kim, Seonyeob Kim, Sechul Oh, and Han Ho Song. Experimental study of homogeneous charge compression ignition engine operation fuelled by emulated solid oxide fuel cell anode off-gas. *Applied Energy*, 229:42–62, nov 2018.

[63] S H Chan, K A Khor, and Z T Xia. A complete polarization model of a solid oxide fuel cell and its sensitivity to the change of cell component thickness. *Journal of Power Sources*, 93(1-2):130–140, feb 2001.

[64] P. Colonna and T.P. Van der Stelt. FluidProp: a program for the estimation of thermophysical properties of fluids, 2004.

[65] Anthony F Mills. *Basic Heat and Mass Transfer*. Prentice Hall, inc, Los Angeles, 2/e edition, 1999.

[66] Caisheng Wang and M Hashem Nehrir. A physically based dynamic model for solid oxide fuel cells. *IEEE Transactions on Energy Conversion*, 22(4):887–897, 2007.

[67] Robert H Perry. *Perry's chemical engineers' handboek*. McGraw-Hill, 7th edition, 1997.

[68] E Achenbach. Three-dimensional and time-dependent simulation of a planar solid oxide fuel cell stack. *Journal of Power Sources*, 49(1-3):333–348, apr 1994.

[69] Bloomenergy. Bloomenergy product data sheet - Energy server 5. *Bloom energy Corporation*, 2016.

[70] Meng Ni, Michael K H Leung, and Dennis Y C Leung. A modeling study on concentration overpotentials of a reversible solid oxide fuel cell. *Journal of Power Sources*, 163(1):460–466, dec 2006.

[71] P. Aguiar, C.S. Adjiman, and N.P. Brandon. Anode-supported intermediate-temperature direct internal reforming solid oxide fuel cell: II. Model-based dynamic performance and control. *Journal of Power Sources*, 147(1-2):136–147, sep 2005.

[72] P. Iora, P. Aguiar, C. S. Adjiman, and Nigel P. Brandon. Comparison of two IT DIR-SOFC models: Impact of variable thermodynamic, physical, and flow properties. Steady-state and dynamic analysis. *Chemical Engineering Science*, 60(11):2963–2975, 2005.

[73] D Stapersma. *Diesel Engines, Volume 2 Turbocharging*. DELFT UT, NLDA, 1 edition, 2010.

[74] K Zinner. *Supercharging of Internal Combustion Engines*. Springer-Verlag, Heidelberg, 1978.

[75] SL Dixon and CA Hall. *Fluid Mechanics and Thermodynamics*. Elsevier Inc, UK, seventh edition, 2014.

[76] R D Geertsma, K Visser, and R R Negenborn. Adaptive pitch control for ships with diesel mechanical and hybrid propulsion. *Applied Energy*, 228:2490–2509, 2018.

[77] C Robinet, J Andrzejewski, and P Higelin. Cycle-to-Cycle Variation Study of an SI Engine Fired by Spark Plug and a Non Conventional Device. *SAE Technical Paper Series*, 1:163–170, 2010.

[78] Harsh Sapra, Milinko Godjevac, Wim Sluis van, Peter Vos de, and Klaas Visser. Modelling of Hydrogen-Natural Gas Combustion (to be published). 2019.

[79] Dr S.P.S. Badwal. Solid Oxide Fuel Cell technology. https://csiropedia.csiro.au/ceramic-fuel-cells/ (Date accessed: 2019-05-08), 2013.

[80] Robert Holyst and Andrzej Poniewierski. *Thermodynamics for Chemists, Physicists and Engineers*. Springer Dordrecht Heidelberg New York London, 2012.

[81] B Todd and J B Young. Thermodynamic and transport properties of gases for use in solid oxide fuel cell modelling. *Journal of Power Sources*, 110(1):186–200, jul 2002.

[82] U G Bossel. Facts and Figures, Final Report on SOFC Data, IEA report, Annex II, Modelling and Evaluation of Advanced SOFC. Technical report, Swiss Federal Officie of Energy, 1992.

[83] D Stapersma. *Diesel Engines, Volume 3 Combustion*, volume 3. DELFT UT, NLDA, 1 edition, 2003.

[84] D Stapersma. *Diesel Engines, Volume 6 Thermodynamical principles II*. DELFT UT, NLDA, 1 edition, 2010.